THE ORBITAL EVOLUTION OF PLANET-DISK SOLAR SYSTEMS

by

Althea Valkyrie Moorhead

A dissertation submitted in partial fulfilment
of the requirements for the degree of
Doctor of Philosophy
(Physics)
in the University of Michigan
2008

Doctoral Committee:

Professor Fred C. Adams, Chair
Professor Carl W. Akerlof
Professor Nuria P. Calvet
Professor August Evrard
Professor Mark E. Newman

ACKNOWLEDGMENTS

I would like to thank my adviser, Fred Adams, for providing me with the advice, oversight, and research education that made the completion of this dissertation possible. Additionally, I would acknowledge the influence of Ed Thommes, Zsolt Sandor, and Matt Holman through a few key conversations regarding elements of this thesis. Finally, I would like to thank Kimberly Smith for assisting me with the myriad beaurocratic steps associated with the completion of a Ph.D.

Monetary support for this thesis was provided by the Terrestrial Planet Finder Program, the Michigan Center for Theoretical Physics, and by NASA through the Origins of Solar Systems Program.

CONTENTS

CHAPTER

LIST OF FIGURES

Figure

LIST OF TABLES

Table

CHAPTER 1

INTRODUCTION

Our solar system contained the only known planets orbiting a main sequence star until 1995, when a planet was found orbiting the Sun-like star 51 Peg via a periodic Doppler shift in the star's spectrum. The discovery of more than 200 additional extrasolar planets has overturned our understanding of what constitutes a typical planetary system. The extrasolar planets discovered to date are Jupiter-sized, possess a wide range of orbital eccentricities ($0 \leq \epsilon \leq 0.9$), and orbit their host stars with small semi-major axes (0.03 AU $\leq a \leq 6$ AU). In contrast, similarly sized planets in our solar system (Jupiter and Saturn) live in nearly circular orbits at 5 and 10 AU.

These discoveries prompted corresponding shifts in solar system evolution theory. We previously believed that planets formed in, or near, their current orbits. However, ice, which plays a significant role in forming the dense solid core of a gas giant, will not condense within 3 AU of a Sun-like star, which in turn implies that gas giant planets are unlikely to form with the small semi-major axes they possess. We now believe that massive planets form outside of this "snow line" and subsequently move inward via interactions with a circumstellar disk, a process known as planetary migration. There are two limiting cases in migration theory in a laminar disk: Type I migration, in which a planet lacks sufficient mass to clear a gap in the disk material and is driven inward by a density wake in the disk, and Type II migration, in which massive planets do clear a gap and are driven inward by resonances between the planet and material in the remainder of the disk. For completeness we note that additional models of runaway migration have been proposed as a way to explain “hot Jupiters” (sometimes called Type III migration – see Masset & Snellgrove, 2001; Masset & Papaloizou, 2003), although they are not considered here. If the disk is not laminar, Type I migration can be overwhelmed by turbulent effects (Laughlin et al., 2004; Nelson, 2005). An important astronomical challenge is to provide a theoretical explanation for the observed distributions of orbital elements. A related challenge is to understand the physical mechanism through which planets migrate inward from their birth sites.

This thesis addresses many important issues in the evolution of solar systems, including what initial planet mass function is likely, what mechanisms give rise to the observed distributions of extrasolar planet orbital elements, and how often terrestrial planets are likely to be detected by transit observations. We organize this thesis as follows: chapters 2 and 3 review relevant aspects of planet observations and solar system dynamics, and chapters 4-7 present research completed in the course of this thesis work; this material is also available in Moorhead & Adams (2005) and Moorhead & Adams (2008). Finally, our main results are summarized in chapter 8.

CHAPTER 2

OBSERVATIONS OF EXTRASOLAR PLANETS

2.1 Observation Methods

While the current catalog of extrasolar planets is less than fifteen years old, forward-thinking astronomers have been proposing extrasolar planet detection methods for many decades. One example is Otto Struve's 1952 paper detailing how massive planets in tight orbits produce a wobble in their host star detectable though a Doppler shift in the star's spectrum (Struve, 1952.) In this same document, Struve points out that a large planet in a small orbit is also likely to eclipse its host star, an effect which can be detected through a dip in the star's overall brightness. Thus, the two main planet detection methods in current use were first proposed over fifty years ago.

2.1.1 Reflex Velocity Observations

Astronomers were historically prevented from observing extrasolar planets due to insuffuciently precise Doppler reflex motion measurements; a planet such as Jupiter will produce a reflex velocity in its sun of about 10 m/s (this quantity can be obtained from Eq. 2.1.1), while radial velocity measurements had uncertainties of order 1 km/s. The last quarter of a century saw a series of advances in radial velocity measurements; systematic errors were reduced by obtaining the reference spectrum and stellar spectrum simultaneously (Griffin & Griffin 1973), and the uncertainty was gradually whittled down. In 1996, an accuracy of 3 m/s was obtained by sending starlight through an iodine cell and using the iodine absorption lines as a scale (Butler et. al., 1996); a host of extrasolar planet detections followed.

The three quantities derived from Doppler shift observations of a planet-star system are the period of reflex velocity fluctuations, the amplitude of the fluctuations, and the mass of the central star, which is obtained by determining its spectral type. Combining the period of the fluctuations with the star's mass yields the semi-major axis. The velocity amplitude K of a star M_* due to a planet of mass M_P tilted with respect to the viewer by angle i is

$$K = \left(\frac{2\pi G}{P}\right)^{1/3} \frac{M_P \sin i}{(M_P + M_*)^{2/3}} \frac{1}{(1-e^2)^{1/2}}\,, \tag{2.1}$$

where e is the orbital eccentricity and a is the semi-major axis of the planet's orbit (Perryman, 2000).

This leaves a degeneracy between M_P, i, and e. However, further information can be gleaned from the reflex velocity as a function of time. As a simple example, if an orbit is eccentric and perogee does not lie along the viewer's line of sight, the minima in radial velocity will not occur halfway between maxima as they would for a planet in a circular orbit. Thus, further examination of the radial velocity curve allows us to calculate eccentricity, leaving only M and i degenerate in this set of variables.

2.1.2 Transit Observations

The first observations of extrasolar planets using the transit method of detection were made in 1999 (Charbonneau et al., 2000; Henry et al., 2000). Observers using this technique survey stars that are known or expected to have planets; however, even if a planet is known to exist around a given star, the odds that the planet will transit the star are long. For this reason, transit detections remain behind reflex velocity detections in number.

On the other hand, supplementing with transit observations helps to fill in the gaps left by the radial velocity observation method. The mere occurence of a transit implies that we are seeing the system edge on, and that $M_P \sin i = M_P$. The primary observables of a transit are the depth, duration, and period of recurrence of the decrease in the star's luminosity. The period, of course, yields the semi-major axis of the transiting planet, which can be compared with any existing radial velocity measurements of the same quantity.

The decrease in luminosity, combined with a main sequence estimation of the star's radius, yields the radius of the planet; $\Delta L/L = (R_P/R_*)^2$. Transit observations have yielded the surprising information that many exoplanets are much less dense than Jupiter; the first observed transiting planet, HD 209458b, possesses a density roughly 30% that of Jupiter (Charbonneau et al., 2000).

The duration of the transit reflects the angular velocity of the planet at the time of the transit. Work is currently underway to transform this quantity, along with other variables, into additional information about the planet's orbit (see, for example, Ford et al., 2008). Small variations in the period may be indications of additional, otherwise invisible, bodies in the extrasolar planetary system (Holman & Murray, 2005).

2.1.3 Additional Observational Techniques

In addition to the radial velocity and transit methods, potential mechanisms for detecting extrasolar planets include gravitational microlensing and direct imaging. Microlensing occurs when a small body, such as a planet, passes near a luminous body; its gravitational field focuses the light coming from the luminous object and causes a slight amplification in brightness. Direct imaging, while currently difficult to impossible considering the many orders of magnitude difference between a star and a planet's luminosity, grows more plausible all the time with advances in coronagraphy and adaptive optics. However, these methods have yet to result in any planet discoveries.

2.2 Properties of the Extrasolar Planets

With more than 200 discoveries so far, it is possible to comment on the properties of the observed planets. First of all, though we are only able to determine $M_P \sin i$, and not M_P, for the majority of planets, due to the degeneracy inherent in the radial velocity approach, we expect the viewing angle to have a random distribution. Therefore, the distribution of $M_P \sin i$, which is roughly characterized by the power law $dN_P/dM_P \propto M_P^{-1.16}$ (Butler et al., 2006), should more or less resemble the true distribution of M_P (see Fig. 2.1).

2.1

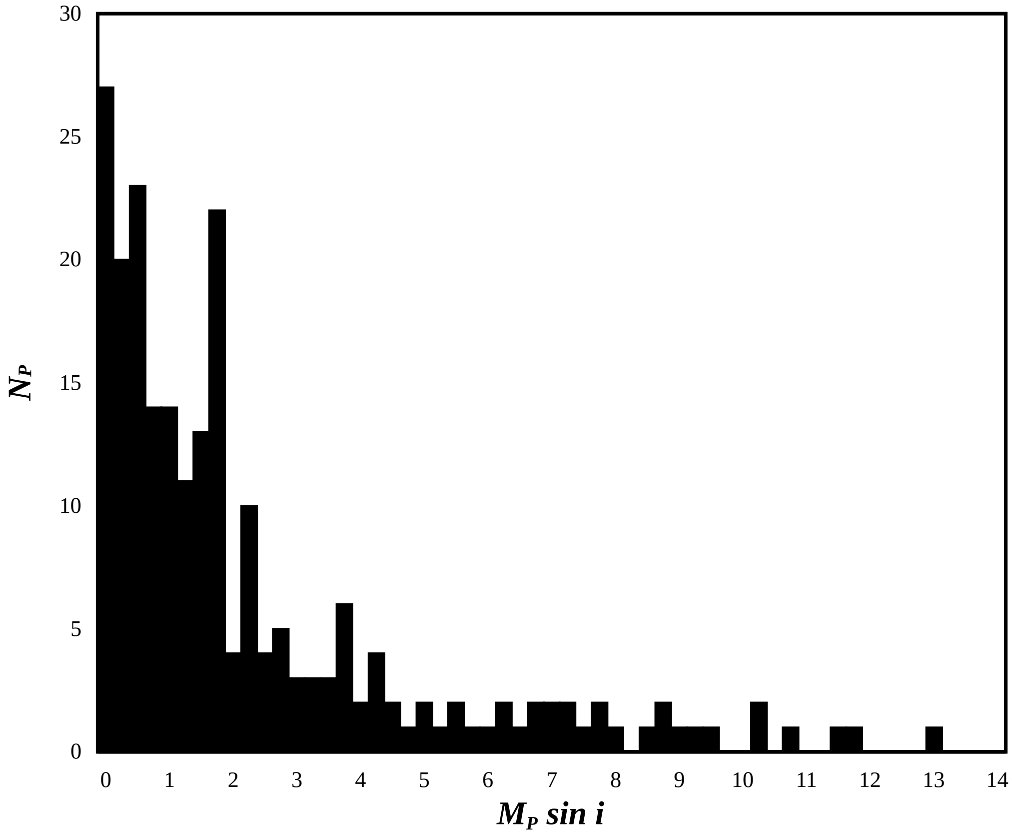

Figure 2.1. The number of planets, N_P, with $M_P \sin i$ between M and $M + dM$, where $dM = 0.25 M_J$. Notice the power law shape of the mass distribution.

As mentioned previously, the observed extrasolar planets generally lie much closer to their host stars than Jupiter does in our system, with an average period of about 3 days. Simultaneously, these planets possess fairly eccentric orbits; the mean eccentricity of the observed planets is 0.24, and the median 0.2, with eccentricities as high as 0.9 (using data posted on `exoplanets.org` as of May 2008; this data is from Butler et al., 2006, and is updated by the authors). To first order, the observed planets fill the eccentricity-semi-major axis parameter space (see Fig. 2.2).

2.2

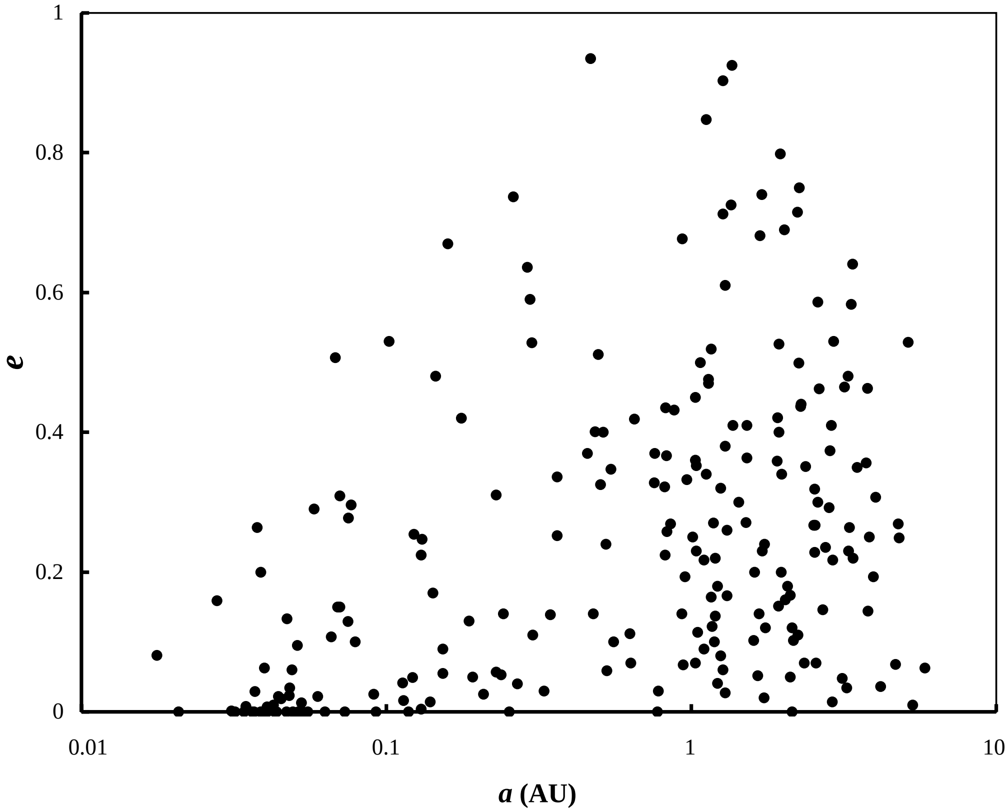

Figure 2.2. Eccentricity versus semi-major axis for the population of observed extrasolar planets. Note that the scale for semi-major axis is logarithmic, reflecting the large number of planets with periods on the order of days. The eccentricity distribution, on the other hand, is very roughly linear, with large numbers of planets with intermediate and high values of eccentricity. This breaks down for planets with semi-major axes less than 0.1, which are subject to long-term tidal circularization.

This distribution is partly affected by observational biases; both the transit and radial velocity methods of planet detection favor massive, short-period planets. The lower limit on detectable reflex velocities, for instance, is a couple meters per second (Butler et al., 2006); in comparison, Jupiter induces a reflex velocity in the sun of 13 m/s. Thus, while Jupiter would be detectable by this method, Neptune, with an induced solar reflex velocity of 0.2 m/s, would not.

On the other hand, the wide range in observed eccentricity exists despite a slight bias against detecting planets with large eccentricities, and, while observational biases describe why it is possible to detect planets with small orbits, it does not explain why such planets exist. To truly understand the extrasolar planets, we must investigate how the planets moved into their current, observed, configurations.

CHAPTER 3

SOLAR SYSTEM DYNAMICS

All solar systems are governed primarily by gravitational forces, which can be easily calculated in N-body simulations (though of course this calculation is time-consuming if many bodies are present.) However, planets are thought to form from the material in a circumstellar disk, and both the mechanism of planet formation and the disk's continued effects on solar system dynamics are incompletely understood. Much of current solar system dynamics research is devoted to better understanding the role of the disk; here we present recent developments in this area.

3.1 Planet Formation

There are two competing theories of solar system formation: the core accretion model and the gravitational instability model. While the core accretion model works for a variety of disk masses, the gravitational instability model requires a highly massive, cold disk for the spontaneous condensation of planet-sized bodies. Here we summarize the two models and their implications for the orbital elements of newly-formed planets.

3.1.1 The Core Accretion Model

The standard core accretion model (see, e.g., Pollack et al., 1996) combines three phases, as seen in Figure 3.1: [1.] In the first phase, solids accrete onto a planetary embryo until the planet's feeding zone is depleted. [2.] Subsequently, solids and gas accrete onto the embryo at a slow, nearly constant rate. [3.] When the embryo reaches a critical mass, runaway gas accretion commences and continues until the planet's (now enlarged) feeding zone is once again depleted. The first and third phases take place rapidly; the timescale of planet formation in the core accretion model is almost entirely determined by the length of the second phase.

3.1

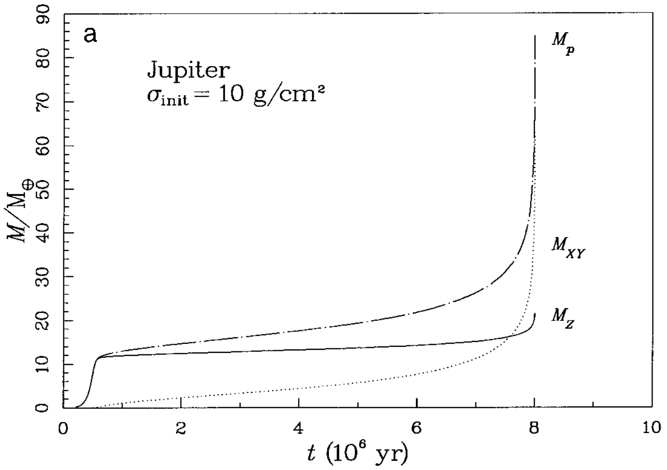

Figure 3.1. Mass as a function of time for Jupiter's formation under the core accretion model as simulated by Pollack et al. (1996). Total mass, M_P, is represented by the dashed line, while the mass in hydrogen and helium, M_{XY}, is represented by the dotted line and mass in all other elements, M_Z, is represented by the solid line. The three phases of the core accretion model are plainly visible; runaway planetesimal accretion takes place in less than 1 Myr, followed by slow accretion of both gases and solids for the next 7 Myr. At the 8 Myr mark, the critical mass is reached and runaway gas accretion takes place.

The core accretion process is usually modeled starting with a field of planetesimals. A large number of initial planetesimals is assumed and their velocities determined by assigning a probability density to individual orbital elements; perihelia and longitudes of ascending nodes are evenly distributed and inclination angles and eccentricities are Rayleigh distributed (Lissauer, 1993). Collision frequency and outcome determined the growth rate of the largest planetesimal. Objects in non circular orbits undergo radial motion given by $r_{\rm max} - r_{\rm min} = a(1+e) - a(1-e) = 2ae$, where a is the object's semi-major axis and ϵ is the object's orbital eccentricity. Accretion takes place most rapidly when random velocities, and thus the quantity $2a\epsilon$, are small; protoplanets acquire small but non-zero eccentricities of order 0.01, which are nevertheless sufficient for the protoplanets to suffer close encounters (Safronov, 1991).

Hydrogen and helium do not condense in the solar nebula, and so must be accreted onto protoplanets in gaseous form. Additionally, a gas envelope surrounding an ice core cannot remain static if the core mass is greater than 10-15 earth masses (Mizuno, 1980). The similarity to estimated core masses of Jupiter and Saturn gives impetus to the core accretion model.

The core accretion model predicts the formation of multiple planets spaced radially between the snow-line, or the 3 AU distance from a sun-like star at which ices condense, and about 30 AU. Since the core accretion model requires the formation of a solid core, planet formation in this model is inhibited within the snow-line due to the lack of solid ices. As mentioned above, planets are thought to attain small orbital eccentricities. The timescale for the core accretion model is comparable to estimated disk lifetimes of a few million years. While the seminal work by Pollack et al. seems to indicate a timescale problem (i.e., the lengthy second phase barely completes by the time the disk dissipates), more recent work has noticeably shortened the formation timescale. In particular, more accurate equations of state (Saumon & Guillot, 2004), updated opacities (Ikoma et al., 2000), and the inclusion of disk density patterns (Klahr & Bodenheimer, 2006) have all shortened the expected timescale for planet formation so that it lies well within the expected timescale of circumstellar disks.

3.1.2 The Gravitational Instability Model

The gravitational instability model of planet formation, in which massive, cold disks collapse into smaller, planet-mass fragments, was developed as an alternative to the core accretion model. The underlying physics of this mechanism can be understood by looking at the Toomre stability factor (Toomre, 1964), Q,

$$Q = \kappa a_s / \pi G \sigma \, , \tag{3.1}$$

where σ is the local, azimuthally averaged surface density, a_s is the sound speed, and κ is the epicyclic frequency, or frequency at which orbiting material undergoes radial oscillations. If Q is greater than 1, the gas is stable against axisymmetric perturbations (Shu, 1992). We can see from this equation that if the temperature, and thus the sound speed $a_s \propto \sqrt{T}$, are low, and the surface density is high, the disk is subject to non-axisymmetric perturbations, which may lead in turn to gravitational collapse.

Hydrodynamical simulations of heavy ($M_D \gtrsim 0.1 M_\odot$), cold disks indeed show signs of the disks collapsing into smaller fragments (e.g., Boss, 2001) which could potentially continue to collapse into gas giant planets. This collapse takes place within the time it takes the fragments to complete an orbit or two; therefore, it is an extremely rapid mechanism for planet formation. Fragments are most like to form at large distances from the central star (10s of AUS) where the disk is coldest; disk material near the star is stabilized against collapse by the star's heating.

While these two models have significantly different starting disks and mechanisms of planet formation, both predict that planets are unlikely to form near the central star of solar systems. This contrasts with observations; the detected exoplanets frequently lie in orbits with semi-major axes measuring a fraction of an AU, in some cases as small as 0.01 AU. Thus, additional physics is required to explain the observed properties of solar systems.

3.2 Planet Migration

Neither model of planet formation predicts planets with small semi-major axes; additionally, the core accretion model produces planets with small eccentricities only. In contrast, the observed extrasolar planets possess a wide range of orbital eccentricities ($0 \leq \epsilon \leq 0.9$), and orbit their host stars with small semi-major axes (0.03 AU $\leq a \leq$ 6 AU).

The most popular explanation for this discrepancy is planetary migration, in which massive planets form outside of the "snow line," or radius outside of which ices are able to condense, and subsequently move inward via interactions with a circumstellar disk. There are two limiting cases in migration theory in a laminar disk: Type I migration, in which a planet lacks sufficient mass to clear a gap in the disk material and is driven inward by a density wake in the disk, and Type II migration, in which massive planets do clear a gap and subsequently drift inward on the viscous timescale of the disk.

Whenever the ratio of periods of two orbiting bodies is a rational number, the system will repeatedly pass through the same configuration over and over. If the orbits are aligned in one of a set of certain configurations (one example, for a 2:1 mean motion ratio, occurs when the planets' apogees are anti-aligned; Murray & Dermott, 2001), the situation is known as a mean motion resonance. This leads to significant planet-planet interactions as each planet is repeatedly subjected to the same forces. In addition to resonances between planets, resonances can exist between a planet and annuli in a circumstellar disk. In fact, a planet-disk system contains an infinite number of such resonances, and corresponding torques, between the disk and the planet.

Disk-planet resonances occur, and torques are exerted, where the motion of a ring in the disk matches the pattern speed $\Omega_{\ell,m}$ of the planet,

$$\Omega_{\ell,m} = \Omega_P + (\ell - m)\kappa_P/m = \frac{\ell}{m}\Omega_P \quad , \tag{3.2}$$

where Ω_P is the mean motion of the planet and κ_P its epicyclic frequency. The quantities ℓ and m are integer wavenumbers. The most strongly contributing resonances can be divided into two groups; Lindblad resonances and corotation resonances.

3.2.1 Corotation Resonances

Corotation resonances occur where disk material rotates with the same mean motion as the given pattern speed; i.e., at radii r where

$$\Omega(r) = \Omega_{\ell,m} \, . \tag{3.3}$$

We denote the radius at which we encounter a corotation resonance r_C. The expression for the disk torque due to a corotation resonance (Goldreich & Tremaine, 1980; hereafter GT80) in a cold, Keplerian, non-gravitating disk is given by

$$T^{\mathsf{C}}_{\ell,m} = -\frac{4m\pi^2}{3}\left[\frac{r}{\Omega(r)}\frac{d}{dr}\left(\frac{\Sigma}{\Omega}\right)(\phi^{\mathsf{P}}_{\ell,m})^2\right]_{r_C} \, . \tag{3.4}$$

where $\phi^{\mathsf{P}}_{\ell,m}$ is the $(l,\, m)$ component of the cosine expansion of the disturbing potential produced by the planet (see GT80), and is discussed in further detail below.

3.2.2 Lindblad Resonances

Lindblad resonances, perhaps best known for giving rise to spiral arms in galaxies, occur at radii where a test particle in the disk encounters peaks in the potential at the same frequency as it undergoes radial oscillations (Binney & Tremaine, 1987). The condition for this to occur is $\Omega(r) \pm \kappa(r)/m = \Omega_{\ell,m}$, where $m > 0$. For a Keplerian disk, in which $\kappa = \Omega$, this condition can be written in the form

$$\Omega(r) = \left(\frac{m}{m \pm 1}\right)\Omega_{\ell,m} \, . \tag{3.5}$$

The radius of a Lindblad resonance is denoted r_L. In the above equation and throughout this discussion, we take the top sign for an outer Lindblad resonance and the lower sign for an inner Lindblad resonance. The expression for the disk torque due to a Lindblad resonance in a cold, Keplerian, non-gravitating disk is given by

$$T^{\mathsf{L}}_{\ell,m} = \frac{m\pi^2}{3(1 \pm m)}\left[\frac{\Sigma(r)}{\Omega^2(r)}\left(\frac{r d\phi^{\mathsf{P}}_{\ell,m}}{dr} \mp 2m\phi^{\mathsf{P}}_{\ell,m}\right)^2\right]_{r_L} \, . \tag{3.6}$$

3.2.3 Determining the Expansion Coefficients

Just as the disk is insufficiently massive for self-gravitation, the orbiting planet's gravitational potential is small in comparison to the potential produced by the central star. As a result, we treat the planet's influence as a small perturbation in the overall potential, and consider the cosine expansion of the potential. The elements of this expansion correspond to resonances between the planet and disk material at different radii.

The disturbing potential ϕ^{P} produced by an orbiting planet moving in the plane of the disk is well known (see, for example, Murray & Dermott, 2001), and is given by

$$\begin{aligned} \phi^{\mathsf{P}}(r,\theta,t) &= GM_P\left(\frac{\mathbf{r_P}\cdot\mathbf{r}}{r^3}-\frac{1}{|\mathbf{r}-\mathbf{r_P}|}\right) \qquad (3.7)\\ &= GM_P\left(\frac{r_P\cos(\theta-\theta_P)}{r^2}-\frac{1}{\sqrt{r^2+r_P^2-2rr_P\cos(\theta-\theta_P)}}\right) \end{aligned}$$

We can expand in terms corresponding to pattern speeds $\Omega_{\ell,m}$:

$$\phi^{\mathsf{P}}(r,\theta,t)=\sum_{\ell=-\infty}^{\infty}\sum_{m=0}^{\infty}\phi^{\mathsf{P}}_{\ell,m}(r)\cos(m\theta-\ell\Omega_P t)\,. \qquad (3.8)$$

Defining $\beta=r/a$, we can write the expansion coefficients $\phi^{\mathsf{P}}_{\ell,m}$ in the form

$$\begin{aligned} \phi^{\mathsf{P}}_{\ell,m}(\beta) &= \frac{GM_P}{2\pi^2 a}\int_0^{2\pi}\int_0^{2\pi} d\theta d\xi\Bigg[\cos(m\theta-\ell(\xi-\epsilon\sin\xi))(1-\epsilon\cos\xi)\\ &\qquad\times\left(\frac{g(\theta,\xi)}{\beta^2}-\frac{1}{\sqrt{\beta^2+(1-\epsilon\cos\xi)^2-2\beta g(\theta,\xi)}}\right)\Bigg], \qquad (3.9)\\ g(\theta,\xi) &= (\cos\xi-\epsilon)\cos(\theta)+(\sqrt{1-\epsilon^2}\sin\xi)\sin(\theta)\,. \end{aligned}$$

Note that β is not a free variable, but is determined by m, ℓ, and the type of resonance. As a result, $\phi^{\mathsf{P}}_{\ell,m}(\beta)$ is a non-trivial function of m, ℓ, ϵ and the type of resonance, as both the planet mass M_P and the semi-major axis a are prefactors.

3.2.4 Type I Migration

When the planet is insufficiently massive to clear a gap in the disk (i.e., the planet is less than 0.1 M_J), an infinite number of resonances exist close to the planet. Therefore, one computes first the torque density as a function of radius near the planet, then uses this quantity to compute the average torque per radial interval.

For a given ring torque component T with pattern speed Ω, the semi-major axis and eccentricity evolution is given by (GT80)

$$\frac{da}{dt} = -\frac{2\Omega_P}{a\kappa^2 M_P} T \tag{3.10}$$

$$\frac{de}{dt} = -\left[(\Omega - \Omega_P) - 2e^2\Omega_P \left(1 + \frac{d\ln\kappa_P}{d\ln r}\right)\right] \frac{T}{M_P e (a\kappa_P)^2} \tag{3.11}$$

where Ω_P and κ_P are the mean motion and epicyclic frequency at a, the location of the planet. Integration over radius yields semi-major axis and eccentricity damping on a timescale of thousands of years. Note that this is much shorter than the accepted lifetime of circumstellar disks, which are estimated to last for a few million years. While overcoming planet accretion is an important obstacle in understanding whether the core accretion model can take place, several methods for slowing or halting Type I migration have been proposed, such as turbulence or the formation of a hole in the disk.

3.2.5 Type II Migration

If a protoplanet survives Type I migration via turbulence, hole formation, or some other mechanism, and accumulates a mass of 0.1 M_J, it begins to clear a gap in the surrounding disk material. The width of this gap can be estimated by balancing the viscous torque with the primary Lindblad torques (Goldreich & Sari, 2003). The viscous torque is given by

$$T_{vis} = 3\pi\alpha\Sigma r^2(\Omega h)^2 \tag{3.12}$$

where h is the disk scale height, or vertical length scale over which disk surface density decreases by a factor of e, given by the sound speed over the mean motion. Σ is the local surface density, and $\alpha = \nu/\Omega h^2$ is the standard parameter for accretion disks. The torque from each principal Lindblad resonance with pattern speed Ω is

$$T_L \approx \left(\frac{r}{w}\right)^3 \Sigma r^2 (r\Omega)^2 \left(\frac{M_P}{M_*}\right) , \tag{3.13}$$

where M_P/M_* is the ratio of the planet mass to central star mass. Combining these two equations yields the gap width

$$\frac{w}{r} \approx (3\pi\alpha)^{-1/3} \left(\frac{r}{h}\frac{M_P}{M_*}\right) . \tag{3.14}$$

Using the values $\alpha = 10^{-3}$ and $h/r = 0.04$, a Jupiter-mass planet at 1 AU produces a gap of width 0.4 AU.

Because a wide gap has been cleared, the planet's semi-major axis is no longer noticeably affected by Lindblad and corotation torques. Instead, the planet drifts inward on the viscous timescale of the disk; that is,

$$\frac{1}{a}\frac{da}{dt} = t_{vis}^{-1} \sim \alpha\Omega \left(\frac{h}{r}\right)^2 . \tag{3.15}$$

However, the eccentricity evolution is still governed by resonant disk torques. For a Keplerian disk, the eccentricity evolution due to an individual disk torque T_D is

$$\frac{d\epsilon}{dt} = \frac{(1-\epsilon^2)\left[(1-\epsilon^2)^{-1/2} - \ell/m\right]/\epsilon}{M_P\sqrt{GM_* a}} T_D , \tag{3.16}$$

where a, ϵ, and M_P are the semi-major axis, eccentricity, and mass of the planet, m is the azimuthal wavenumber of the pattern speed (see Eq. 3.2), and T_D is the portion of the torque exerted by the disk on the planet that corresponds to the Fourier component of the planet's potential with azimuthal wavenumber m and pattern speed $(l/m)\Omega_P$ (Goldreich & Sari, 2003).

Recall that the system contains an infinite number of resonances, and corresponding torques, between the disk and the planet. For example, if we assign these resonances wavenumbers $(m,\ \ell)$, the location of a corotation resonance is given by $r_C = a[m/(\ell)]^{3/2}$. However, the massive planets of interest here will clear large gaps in the disk, providing, for each value of ℓ, an upper limit on the number of resonances contributing to the total torque. The shape of the gap also affects the eccentricity evolution; Lindblad resonances are proportional to surface density, and corotation resonances are proportional to the radial derivative of surface density. Thus, in the Type II migration case, we first calculate the location and torque of each resonance, then sum over the finite number of contributions to obtain the total eccentricity time derivative due to these resonances.

These formulae will be of particular importance in Chapter 5, in which we calculate the eccentricity time derivative as a function of initial eccentricity.

3.3 MHD Turbulence

We have seen the effects of a circumstellar disk on early solar system evolution through the mechanism of planet migration. The disk itself, however, is subject to a magnetic field; if this magnetic field has a poloidal component, and the angular velocity of the disk material decreases with radius, the disk is unstable to axisymmetric disturbances (Balbus & Hawley, 1991), a phenomenon referred to as magnetorotational instability (MRI.) Magnetohydrodynamical turbulence plays an important role in star formation theory; expecting this turbulence to continue beyond the formation of a protostar and into the planet-formation era is therefore not unreasonable.

The central star threads the disk with a poloidal field; furthermore, circumstellar disks are not likely to be massive enough for angular velocity to increase with radius. MRI turbulence, then, should be present in all circumstellar disks, and should be included in models of solar system formation. In fact, several studies have shown that MRI turbulence is capable of overwhelming Type I migration on sufficiently short timescales (Laughlin, Steinacker, & Adams, 2004; and Nelson, 2005), possibly solving the problem of how planet cores avoid being accreted onto the central star before further planet formation can take place.

Laughlin, Steinacker, and Adams (2004, hereafter LSA04) take the approach of modeling the turbulence spectrum; in this manner, they are able to compute the typical random walk in semi-major axis experienced by a protoplanet embedded in a turbulent disk without performing the (time-expensive) full MHD simulations. While the net displacement due to random walk grows like $\sqrt{t}$ and the effect on semi-major axis due to migration is proportional to $e^{-t/\tau_{damp}}$, it is possible for turbulence to overwhelm migration on a finite timescale. If that timescale is the lifetime of the circumstellar disk, or the time necessary for the protoplanet to begin runaway gas accretion, then MRI turbulence can prevent the accretion of protoplanets onto the central star.

While small protoplanets are easily batted around by turbulent fluctuations, massive bodies are less affected. Nevertheless, turbulence may still play an important role in gas giant dynamics. In multiple body systems, differential migration will, without fail, force pairs of planets into resonances. If these resonances are stable, both planets will remain in the system for the lifetime of the disk; if not, one planet is likely to be ejected from the system or accreted onto the central star. If turbulence is present in the surrounding disk, the small perturbations the planets experience may be capable of jostling them out of resonance. In this manner, an otherwise small effect could prove important for the dynamics of systems with large planets.

The turbulence model of LSA04, while developed initially for use in an analytic calculation, can also be easily incorporated into N-body simulations. The potential of a particular turbulent fluctuation is given as

$$\Phi = \frac{A\xi e^{-(r-r_c)^2/\sigma^2}}{r^{1/2}} \cos{(m\theta - \phi - \Omega_c \tilde{t})} \sin{(\pi \frac{\tilde{t}}{\Delta t})}\,, \tag{3.17}$$

where r_c and ϕ give the position of the center of the disturbance and σ describes its radial extent. The disturbance persists for time Δt and has pattern speed Ω_c. Each individual disturbance has amplitude ξ, chosen from a gauss-random distribution with unit width, and the entire spectrum has the overall amplitude A. This amplitude can be chosen to mimic the turbulence encountered in MHD simulations (see Laughlin et al., 2004), and has the (awkward) units of $\ell^{5/2}t^{-2}$ where ℓ is a length scale and t a time scale.

CHAPTER 4

MIGRATION THROUGH THE ACTION OF DISK TORQUES AND PLANET-PLANET SCATTERING

Our primary goal in this thesis is to discover how the extrasolar planets obtained the observed combination of small semi-major axes and wide variety in eccentricity. We first investigate the effects of combining planet-planet interactions with disk torques in the form of planetary migration. During the epoch of planet formation and migration, both gaseous circumstellar disks and multiple planets are expected to be present. As previously discussed, sufficiently massive disks – those that are a few percent of the central star's mass – are effective at exerting torques on planets and moving them inward, thereby changing their semi-major axes a. Scattering interactions between planets are effective at increasing the orbital eccentricities ϵ (Lin & Ida, 1997; Kley, 2000; Thommes & Lissauer, 2003; Kley et al. 2004; Adams & Laughlin, 2003, hereafter AL2003). Many of the previous studies focus on explaining particular observed two-planet systems like GJ876 (e.g., Snellgrove et al., 2001; Lee & Peale, 2002; Murray et al., 2002) and 47 UMa (Laughlin et al., 2002). This study adopts a more general treatment.

We present a statistically comprehensive study of this migration mechanism and demonstrate that the interplay between these two effects leads to a rich variety of possible outcomes. Because these systems cover a wide range of parameter space and tend to be chaotic, this process results in a broad distribution for the orbital elements of the final systems. This model – Type II migration driven by interactions with a circumstellar disk and by dynamical scattering from other planets – naturally produces the entire possible range of semi-major axis a and eccentricity ϵ.

In this study, we assume planets have already formed and attained sufficient mass to clear gaps in the disk; the starting point of these calculations takes place after Type I migration has run its course (although it remains possible for these early stages to provide an alternate explanation of the observed orbital elements). We utilize a simplified parametric description of Type II migration, in which semi-major axis and eccentricity are damped on roughly Myr timescales.

This chapter has two modest goals: The first objective is to explore the physics of this migration mechanism by extending previous calculations to encompass a wider range of parameter space. this chapter is a straightforward generalization of AL2003, but extends that paper in several ways: [1] In addition to the random mass distribution of AL2003, this chapter considers a a log-random initial mass function for the planets. [2] We explore a much wider range of time scales for eccentricity damping due to the disk. [3] We include starting configurations that lead to the planets being initially caught in both the 2:1 and 3:1 mean motion resonances, and we track how long the planets stay near resonance. [4] The distributions of ejection velocities for escaping planets are determined. [5] In order to isolate the effects of the input parameters on the final results, we present the orbital elements both immediately after planets are lost and after corrections for additional evolution are taken into account. [6] The results presented here include a tenfold increase in the number of numerical simulations and hence in coverage of parameter space (for a total of ~ 8500 trials).

The second goal of this chapter is to determine if this migration mechanism can account for the orbital elements of the observed extrasolar planets. Since the observed orbital elements of these planetary systems explore (nearly) the full range of possible semi-major axis and eccentricity, filling the $a - \epsilon$ plane is a necessary, but not sufficient, condition on a complete theory of planet migration. The mechanism explored here can be made consistent with the observed orbital element distributions, but such a comparison is preliminary and caution should be taken.

4.1 Methods and Initial Conditions

This section outlines our basic migration model which combines the dynamical interactions between two planets with inward forcing driven by tidal interactions with a background nebular disk, i.e., Type II migration (see also Kley, 2000; Murray et al., 2002; Papaloizou, 2003; Kley et al., 2004). Our goal here is to build on previous studies by producing a statistical generalization of the generic migration problem with two planets and an exterior disk – a situation that we expect is common during the planet formation process.

The numerical experiments are set up for two planets with the following orbital properties: Two planets are assumed to form within a circumstellar disk with initial orbits that are widely spaced. The central star is assumed to be of solar-type with mass $M_* = 1.0\ M_\odot$. For the sake of definiteness, the inner planet is always started with orbital period $P_{in} = 1900$ days, which corresponds to a semi-major axis $a_{in} \approx 3$ AU. This radial location lies just outside the snowline for most models of circumstellar disks and thus provides a fiducial starting point where the innermost giant planets are likely to form. For most of the simulations, the second (outer) planet is placed on an orbit with the larger period $P_{out} = \pi 2^{1/4} P_{in} \approx (3.736\ldots)P_{in}$. With this starting state, the planets are not initially in resonance but will first encounter the 3:1 resonance as the outer planet migrates inward. As the system evolves, the two orbits become closer together. With these starting states, the planets are sometimes caught in the 3:1 resonance, but often pass through and approach the 2:1 resonance. In an alternate set of starting states, the outer planet is given an initial orbital period $P_{out} = eP_{in} \approx (2.718\ldots)P_{in}$ so that the planets start inside the 3:1 resonance but outside the 2:1 resonance. In either case, the two planets are often caught in mean motion resonances for some portion of their evolution (for a more detailed description, see Lee & Peale, 2002). In practice, the initial period ratio is likely to have a distribution, but this chapter focuses on these two specific choices. The initial eccentricities of both planets are drawn from a uniform random distribution in the range $0 < \epsilon < 0.05$. The planets are also started with a small, but nonzero inclination angle in the range $i \leq 0.03$ (in radians). Planetary systems started in exactly the same orbital plane tend to stay co-planar, whereas small departures such as these allow the planets to explore the full three dimensions of space.

In this study we use two different distributions for the starting planetary masses. We denote the planetary mass distribution as the IMF (the initial mass function) where it should be understood that we mean planet masses (not stellar masses). The first IMF is a uniform random distribution in which the planet masses m_P are drawn independently from the range $0 < m_P < 5m_J$, where m_J is the mass of Jupiter. In the second mass distribution, denoted as the log-random IMF, the logarithm of the planet mass $\log_{10}[m_P/m_J]$ is drawn independently from the interval $-1 \leq \log_{10}[m_P/m_J] \leq 1$. The random mass distribution provides a good starting point to study the physics of these systems – it provides a good sampling of the possible masses and mass ratios that two planet systems can have. On the other hand, the observed distribution of planet masses is much closer to a log-random distribution, so this latter distribution provides a better model for comparison with observations. One result of this chapter is a determination of how this migration mechanism changes the planetary IMF, and it is useful to study this evolution from the two different starting distributions.

The numerical integrations are carried out using a Bulirsch-Stoer scheme (Press et al., 1986), described more fully in the Appendix. The equations of motion are those of the usual three body problem (two planets and the star) with the following additional forcing terms: The circumstellar disk exerts torques on the planets which lead to both orbital decay (Type II migration) and damping of eccentricity. The star exerts tidal forces on the planets which leads to additional energy dissipation and partial circularization of the orbits. Finally, the leading order curvature of space-time (due to general relativity) is included to properly account for the periastron advance of the orbits.

The outer planet in the system is tidally influenced by a background circumstellar disk. Since the planets are (roughly) of Jovian mass, they clear gaps in the disk and experience Type II migration. Instead of modeling the interaction between the outer planet and disk in detail, we adopt a parametric treatment that introduces a frictional damping term into the dynamics. This damping force has the simple form $\mathbf{f} = -\mathbf{v}{\tau_{\rm damp}}^{-1}$ and is applied to the outer planet at each time step, as a torque $\mathbf{r} \times \mathbf{f}$, so the outer planet is gradually driven inward. The assumed damping force is proportional to the velocity and defines a disk accretion time scale $\tau_{\rm damp}$. We assume here that the disk inside the orbit of the outer planet is sufficiently cleared out so that the inner planet does not usually experience a Type II torque. Over most of its evolution, the inner planet has a sufficiently small eccentricity so that it lies well inside the (assumed) gap edge and receives negligible torque from the disk (which lies outside the outer planet). When the inner planet attains a high eccentricity, however, it can be found at a radius comparable to that of the outer planet and can thus experience some torque. This (relatively minor) effect is included by giving the inner planet a torque that is reduced from that of the outer planet by a factor $(r_{in}/r_{out})^6$.

In this set of simulations, we set the accretion time scale to be $\tau_{\rm damp} = 0.3$ Myr, consistent with recent estimates, outlined as follows. We can compare this time scale to several reference points: [1] For example, Nelson et al. (2000) advocate migration time scales of 10^4 orbits for Jovian mass planets. [2] If disk accretion is driven by viscous diffusion and can be described by an α prescription, then the disk accretion time scale $\tau_{\rm disk} = r^2/\nu$, where the viscosity $\nu = (2/3)\alpha a_s^2 \Omega^{-1}$ (Shu, 1992). The disk scale height H can be written in the form $H = a_s/\Omega$, where a_s is the sound speed, and the accretion time becomes $\tau_{\rm disk} = 1.5(r/H)^2\Omega^{-1}\alpha^{-1}$. If we evaluate the disk scale height H and rotation rate Ω for a temperature of $T = 70$ K at $\varpi = 7$ AU (where the outer planet forms and begins its migration), the adopted disk accretion time scale $\tau_{\rm damp} = 0.3$ Myr corresponds to $\alpha = 7 \times 10^{-4}$. This value falls within the expected range $10^{-4} \le \alpha \le 10^{-2}$ (see Shu 1992). [3] As another point of comparison, three-dimensional simulations of Jovian planets in circumstellar disks (Kley, D'Angelo, & Henning, 2001) find similar migration time scales, about 0.1 Myr, which agree with two-dimensional simulations done previously (Kley, 1999). In these numerical studies, the disks have slightly larger $\alpha = 4 \times 10^{-3}$ (hence the slightly shorter time scale), scale height $H/r = 0.05$, and disk mass $M_d = 3.5 \times 10^{-3} M_\odot$ between 2 and 13 AU. Note that the total disk mass must be larger than the planet masses in order to drive Type II migration. Notice also that the migration time scale is assumed to be independent of the orbital eccentricity, although more complicated behavior is possible.

These simulations include an additional forcing term that damps the eccentricity of the outer planetary orbit (as suggested by numerical simulations of these systems). In other words, the same angular momentum exchange between the disk and the planet that leads to orbital migration can also modify the eccentricity of the orbit. Unfortunately, previous work on this issue presents rather divergent points of view. Most numerical studies indicate that the action of disk torques leads to damping of eccentricity, and these results are often supported by analytic calculations (e.g., Snellgrove et al., 2001; Schäfer et al., 2004). On the other hand, competing analytic calculations indicate that eccentricity can be excited through the action of disk torques and this mechanism has been proposed as an explanation for the observed high eccentricities in the extrasolar planetary orbits (e.g., Ogilvie & Lubow, 2003; Goldreich & Sari, 2003; Papaloizou et al., 2001). One reason for this ambiguity is that the interaction between the disk and the planet can be broken down into the action of resonances in the disk, where the non-coorbital corotation resonances act to damp the eccentricity of the planetary orbits while the non-coorbital Lindblad resonances act to pump it up. The net effect depends on a close competition between the damping terms and the excitation terms. In rough terms, the conditions that result in eccentricity damping are those that lead to relatively narrow gaps, which in turn correspond to large disk viscosity ($\alpha \sim 10^{-3}$) and modest sized planet masses ($m_P \sim m_J$) as assumed here. The disk surface density and scale height also play a role (Bryden et al., 2000). If the gap is not completely clear, then the corotation resonance locations within the gap will contain gas that can interact with the planet and help enforce eccentricity damping (Ogilvie & Lubow, 2003; Goldreich & Sari, 2003). In contrast, wide and clear gaps, which result from smaller viscosity and/or larger planet masses ($m_P \approx 10 - 20 m_J$), can lead to eccentricity excitation (Snellgrove et al., 2001; Papaloizou et al., 2001).

In light of these ambiguities, we incorporate the effects of eccentricity damping in a parametric manner. For completeness, we note that the damping force described above (that which enforces inward migration) also tends to damp the eccentricity, although this effect is much smaller than the explicit eccentricity damping terms included here. Specifically, the orbital eccentricity of the outer planet is damped on a time scale $\tau_{\rm ed}$, which is considered as a free parameter in this treatment. The eccentricity damping is enforced by converting the cartesian variables to orbital elements (a, ϵ, i), applying the damping term, and then converting back. The inclination angle is not explicitly damped, although the outer planet experiences a small damping effect due to the form of the migration force. In this chapter, we explore a range of damping times scales 0.1 Myr $\le \tau_{\rm ed} \le \infty$, where the $\tau_{\rm ed} \to \infty$ limit corresponds to no eccentricity damping. We have also run test cases in which $\tau_{\rm ed}$ varies with orbital eccentricity, so that more eccentric orbits are damped to a greater extent, although the results are not markedly different. Our numerical exploration of parameter space suggests that the most relevant variable is the ratio of eccentricity damping time to disk accretion time, where this ratio falls in the range $1/3 \le \tau_{\rm ed}/\tau_{\rm damp} \le \infty$ for the simulations presented here. For comparison, the full range of positive values for this ratio considered in the literature is approximately $0.01 \le \tau_{\rm ed}/\tau_{\rm damp} \le \infty$ (with an additional range of negative values corresponding to eccentricity excitation). This chapter considers the more limited range because the behavior outside our range is known: For small values of $\tau_{\rm ed}/\tau_{\rm damp}$, eccentricity damping is highly efficient, few planets are ejected, and large eccentricities are not produced (e.g., Lee & Peale, 2002; Thommes & Lissauer, 2003). For negative values of $\tau_{\rm ed}/\tau_{\rm damp}$, eccentricity is excited. We find that even with no eccentricity damping, this model tends to overproduce eccentricity relative to the currently observed sample of extrasolar planets; eccentricity excitation could lead to even larger discrepancies. Note that one advantage of this parametric treatment is that thousands of simulations can be performed and the full distributions of final orbital elements can be determined.

The numerical code includes relativistic corrections to the force equations (e.g., Weinberg, 1972). This force contribution drives the periastron of both planetary orbits to precess (in the forward direction). Because the effect is greater close to the star, the inner planet experiences more precession, and the net effect is to move the two planets away from resonance. If the planets migrate sufficiently close to the central star, this differential precession effect can keep the planets out of a perfect resonance. Since resonant conditions lead to greater excitation of orbital eccentricity, which in turns drives the system toward instability, this relativistic precession acts to make planetary systems more stable. In these simulations, however, the planets rarely migrate close enough to the star to make this effect important, but it is included for completeness.

The simulations also include energy lost due to tidal interactions between the planets and their central stars. In these simulations, the planets spend most of their time relatively far from the star where tidal interactions are negligible. As a result, we adopt a simplified treatment of this effect. Specifically, the force exerted on the planet due to tidal interactions is written in the approximate form

$$\mathbf{F} = -\frac{Gm_P R_*^5}{Cjr^{11}} \left[r^2 \mathbf{v} - (\mathbf{r} \cdot \mathbf{v}) \mathbf{r} \right] \frac{0.6 r_p^3}{1 + (r_p/R_*)^3} \,, \tag{4.1}$$

where R_* is the radius of the star, r_p is the distance of closest approach for a parabolic orbit with angular momentum j, and $C = 2\sqrt{\pi}/3$ is a dimensionless constant of order unity (for further discussion, see Papaloizou & Terquem, 2001; Press & Teukolsky, 1977). This formula implicitly assumes that the time between encounters is long compared to the time for tidal interaction itself and that most of the forcing occurs near the point of closest approach. This approximation is valid when the close encounters occur due to planetary orbits with high eccentricities, which is generally the case for planets in these simulations. Note that for longer term evolution of close planetary orbits, such as circularization over Gyr time scales, an alternate approximation for the tidal forces is necessary (see Section 4.2).

The simulations allow for collisions to take place between the planets, and between the planets and the star. The effective radius for planetary collisions is taken to be $R_P = 2R_J$, with cross section $\sigma_P = 4\pi R_J^2$, which implicitly assumes that the planets have not fully contracted. In order to model accretion events, we assume that when a planet wanders within a distance $d = 2 \times 10^{11}$cm of the central star, accretion takes place. This distance corresponds to $d \sim 3R_\odot$; the pre-main sequence simulations of D'Antona and Mazzitelli (1994) yield stellar radii ranging from $5.7R_\odot$ at 10^5 years to $2.2R_\odot$ at 10^6 years.

For a given set of starting conditions (described above), each numerical experiment is integrated forward in time and the system follows the same basic evolutionary trend (see Fig. 4.1 and Section 3): The planets are started with a sufficient separation so that they have weak initial interactions and are far from resonance. As the outer planet migrates inward through the action of disk torques, the planets often enter into a mean motion resonance, usually the 3:1 or 2:1 resonance because of the starting conditions. The tendency to enter 3:1 versus 2:1 resonances varies with the planetary IMF, with a linear IMF producing more planets in 3:1 resonances and a log IMF producing more 2:1 systems. In addition, the 2:1 resonances last longer, implying that they are more stable. The two planets then migrate inwards together, staying relatively close to resonance, but displaying ever larger librations as the orbital eccentricities of both planets increase (on average). The eccentricities increase until the system (often) becomes unstable, and a wide range of final system properties can result. In practice, we continue the simulations until one of the following stopping criteria is met: A planet is ejected, the planets collide with each other, a planet is accreted by the central star, or a maximum integration time limit is reached (set here to be 1.0 Myr). This latter time scale represents the time over which the disk contains enough mass to drive inward migration of planets; the disk could retain enough gas to exhibit observational signatures over a longer time.

After a planet is lost (through ejection, accretion, or collision), the numerical integration is stopped and the orbital elements of the surviving planet are recorded. In general, however, the orbital elements of the surviving planet can continue to evolve after a planet is lost as long as the disk is still present. In order to separate the effects of the combined migration mechanism (i.e., Type II migration with planet scattering) from the additional evolution, we first present the results with no additional evolution in the following section. In order to compare with the observed orbital elements of extrasolar planets, we consider possible algorithms for this additional evolution in Section 4.

4.2 Results from the Numerical Simulations

This chapter presents the results of an ensemble of $\sim$ 8500 simulations that follow the early evolution of two-planet solar systems subjected to disk torques using the methodology described above. The simulations use two different planetary IMFs and, for each IMF, four choices of the eccentricity damping time scale $\tau_{\rm ed}$. For each set of these input parameters, we completed approximately 800 – 1000 solar system simulations. We then determined the resulting distributions of semi-major axis a, eccentricity ϵ, inclination angle i, and surviving planetary mass m_P. These results can be used to quantify the outcome of this migration mechanism (see below) and can be compared to observed distributions of orbital elements in extrasolar planetary systems (Section 4).

4.2.1 Evolution of Orbital Elements

To illustrate the general behavioral trend of these systems, we follow the evolution of orbital elements for a collection of representative simulations. The result of one such run is shown in Fig. 4.1. The first panel shows how the semi-major axis of each planet decreases smoothly with time; this basic trends holds for essentially all cases. In the second panel of Fig. 4.1, we plot the period ratio of the two planets, and find that it quickly approaches and remains near 3. This result indicates that the two planets may be in a 3:1 mean motion resonance (see Section 3.3 for further discussion). This behavior occurs during the early evolution for the majority of cases, although in some cases the outer planet passes through the 3:1 period ratio (and hence the 3:1 resonance) and the period ratio remains near ∼2 for most of the evolution. In other systems, the period ratio remains near 3 for the early evolution, and then the planets move through the 3:1 resonance, become closer, and reside near the 2:1 resonance for the latter part of the simulation. A more detailed accounting of how long various systems spend near the 3:1 and 2:1 resonances is given below (Section 3.3).

4.1

The behavior of eccentricity and inclination angle is more complex. We find that

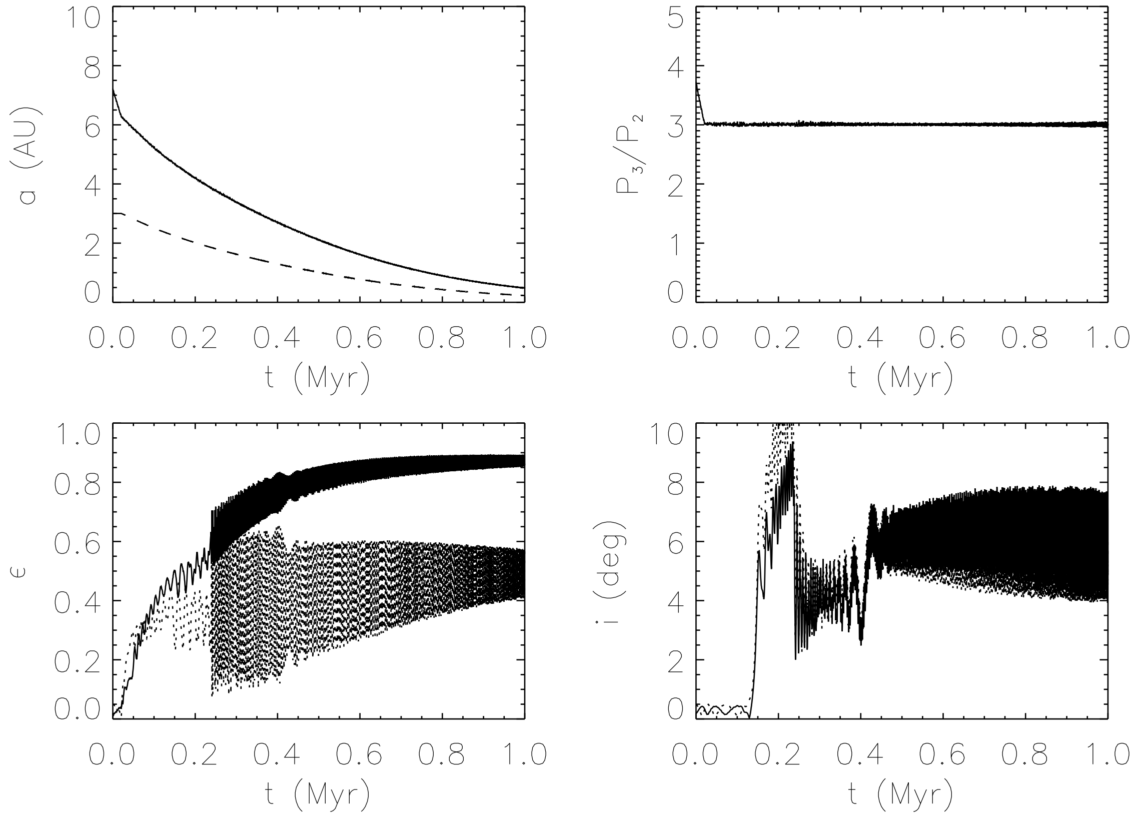

Figure 4.1. Time evolution of a typical system of two interacting planets migrating under the influence of torques from a circumstellar disk. The upper left panel shows the time evolution of the semi-major axes, which decrease steadily on the migration time scale $\tau_{\rm damp}$. The upper right panel shows the ratio of the orbital periods. This ratio quickly decreases to 3 and stays close to this value for much of the evolution (the two planets are near the 3:1 resonance – see section 3.1). The evolution of eccentricity is illustrated in the lower left panel, which shows that the eccentricity of both planets steadily increases at first and then enters into a complicated time series including both short period oscillations and an overall growth trend on longer time scales. The lower right panel shows the corresponding time evolution of the inclination angle. Both planets wander back and forth out of the original orbital plane, but the inclination angles vary by only a few degrees.

orbital eccentricity increases steeply in the beginning, and then undergoes oscillations about an average value that increases at a slower rate. The eccentricity exhibits varying behaviors over different spans of time and varies substantially from case to case. In the more stable systems, the eccentricity values level off and experience variations about the mean. In unstable cases, the eccentricities are driven to ever larger values until a planet is either ejected or accreted onto the central star. The inclination angle experiences a similar evolutionary trend.

This complex behavior of the orbital element leads to a distribution of final values. To illustrate this sensitive dependence on the initial conditions, we have run a set of numerical experiments with equal mass planets, an eccentricity damping time scale $\tau_{\rm ed}$ = 1 Myr, and starting configurations with the outer planet outside the 3:1 resonance. The starting values of the angular orbital elements are chosen randomly from 0 to 2π. The results are shown in Fig. 4.2 for the case of two $m_P = 1.0 m_J$ planets (top two panels) and two $m_P = 5.0 m_J$ planets (bottom two panels). For the case of smaller planets (1 m_J), both planets survive the entire 1.0 Myr time span of the simulations, but they attain a wide distribution of final orbital elements. For the case of larger planets ($5 m_J$), one of the planets is always ejected, whereas the remaining planet attains a distribution of orbital elements as shown. Fig. 4.2 shows that effectively equivalent starting conditions lead to a well-defined distribution of outcomes. In other words, for this class of simulations, the outcomes must be described in terms of the distributions of a or ϵ, rather than as particular values of a or ϵ.

4.2

4.2.2 End State Probabilities

The simulations end in a variety of different states, including ejection, accretion, collision, or the survival of both planets past the fiducial time span of one million years. The frequencies of each fate are listed in Table 4.1 for varying eccentricity

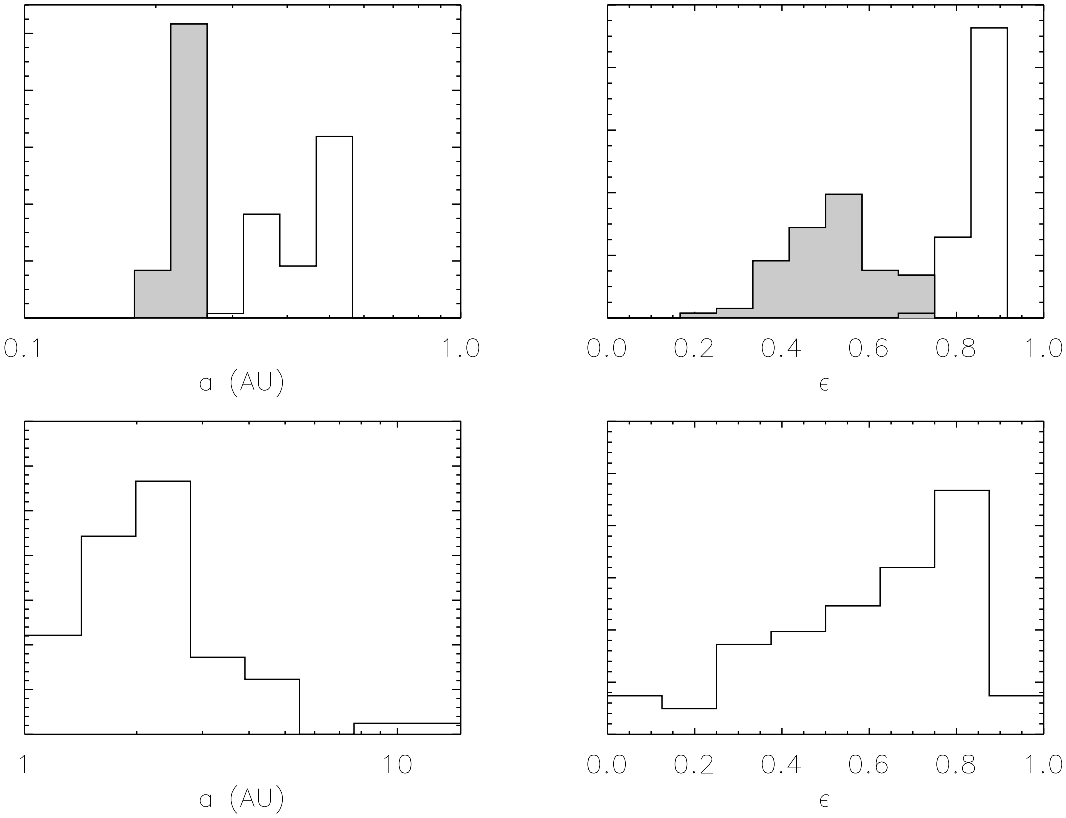

Figure 4.2. Illustration of sensitive dependence on initial conditions. The top panels show the results of simulations performed for two equal mass planets with $m_P = m_J$. The bottom two panels show analogous results for simulations done with two equal mass planets with $m_P = 5m_J$. The set of simulations use the same starting conditions except for the choice of angular orbital elements. In all cases, both planets survive to the end of the fiducial time period of 1 Myr, but the orbital elements of the planets are different, i.e., they show a distribution of values. In the top panels, the orbital elements of the inner planet are shown as the shaded histogram; those of the outer planet correspond to the unshaded histrogram. As mentioned, the bottom two panels show analogous results for simulations done with two equal mass planets with $m_P = 5m_J$. In this case, one of the planets is always ejected, but the remaining planet takes on a distribution of values for its orbital elements.

damping time scales and for both planetary IMFs. The number of ejected planets depends sensitively on the IMF: Only one third of the planets were ejected for a logarithmic IMF, whereas more than half were ejected for a linear IMF. This behavior is expected because the linear IMF provides more massive planets, which in turn produce a disturbing function of greater magnitude and lead to more frequent ejection. We also find that the outer planet is more than 3–4 times as likely to be the ejected planet, and the inner planet is almost always the accreted planet. The incidence of each end state exhibits no clear trend with respect to eccentricity damping time scale (for a given planetary IMF). For the case in which the planets are started just outside the 2:1 resonance (inside the 3:1 resonance), the end state probabilities are similar, but show a slight preference for accretion relative to ejection (see Table 4.1).

Table 4.1. Planetary Fate Probabilities.

$\tau_{\rm ed}$	Ejection	Accretion	Collision	Survival
Linear IMF				
0.3 Myr	0.53	0.33	0.031	0.11
1.0 Myr	0.56	0.19	0.006	0.24
3.0 Myr	0.55	0.16	0.003	0.29
Log IMF				
0.1 Myr	0.25	0.40	0.072	0.27
0.3 Myr	0.34	0.35	0.030	0.29
1.0 Myr	0.34	0.29	0.005	0.37
∞	0.35	0.33	0.004	0.29
Log IMF (2:1)				
1.0 Myr	0.29	0.35	0.011	0.35

Averaged over all outcomes, the mean time of the simulations (which end when a planet is lost) is about 0.5 Myr; this time scale is roughly comparable to the viscous damping time of $\tau_{\rm damp} = 0.3$ Myr. Accretion events take the longest, with an average time of 0.55 Myr; ejection events have a mean time of 0.22 Myr; collisions take place the fastest with a mean time of only 0.10 Myr.

The end states depend on the planet masses in a systematic way, as shown in Figs. 4.3 and 4.4, which show the various possible end states as a function of the masses.

For systems in which the outer planet is substantially more massive than the inner one, $m_{out} \gg m_{in}$, the inner planet is nearly always driven to high eccentricities and accreted onto the central star (as shown by the blue diamonds in Figs. 4.3 and 4.4). In the opposite limit where $m_{out} \ll m_{in}$, the outer planet tends to be ejected (as shown by the green squares in the figures). When both planets are massive, corresponding to the upper right portion of the mass plane, either planet can be readily ejected. When both planets have relatively low masses, corresponding to the lower left portion of the mass plane, both planets tend to survive (shown by the cross symbols in the figures).

4.3

4.4

Tables 4.2 – 4.4 present the distributions of mass m_P, semi-major axis a, and eccentricity ϵ at the end of the simulations. Each entry lists the mean value of the distribution as well as its width (variance). Table 4.2 presents the planetary masses for all cases, including planets that are lost (ejected planets and accreted planets). The following tables list the parameters that characterize the distributions of semi-major axis (Table 4.3) and orbital eccentricity (Table 4.4) for the planets that remain at the end of the simulations. For accretion or ejection events (of either planet), the distributions of semi-major axis, eccentricity, and mass are roughly similar for a given planetary IMF and varying $\tau_{\rm ed}$ (although variations do exist, especially at the extremes of our chosen range of $\tau_{\rm ed}$). The collisions result in significantly different orbital properties (not listed in the Tables), with smaller eccentricity ϵ and larger mass m_P. The other general trend that emerges from this suite of simulations is that the systems that remain stable over the entire 1 Myr integration time are those with the smallest planets, with a mean mass of only 0.79 m_J (for the log-random IMF, averaged over the four values of $\tau_{\rm ed}$) compared to a mean mass $m_P = 2.8$ m_J for the whole ensemble.

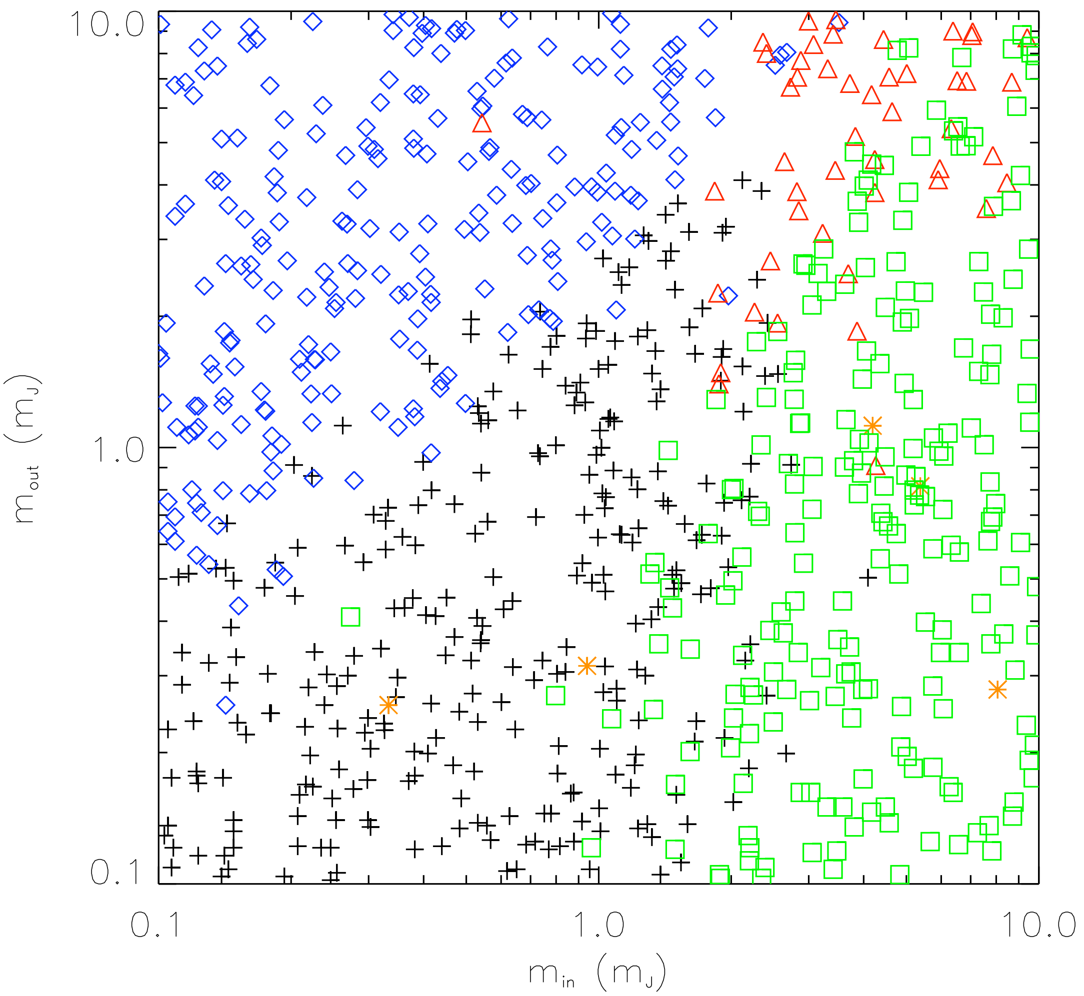

Figure 4.3. End states as a function of the planetary masses for eccentricity damping time scale τ_{ed} = 1 Myr for a linear IMF. Each symbol in this figure represents the outcome of a simulation with the mass of the outer planet plotted as a function of the mass of the inner planet. All of the simulations depicted here use the log-random IMF, the standard starting configuration in which the outer planet begins outside the 3:1 resonance, and eccentricity damping time $\tau_{ed} = 1$ Myr. The different symbols correspond to different outcomes: open blue diamonds represent accretion of the inner planet, open green squares denote ejection of the outer planet, open red triangles represent ejection of the inner planet, crosses denote survival of both planets, and orange star symbols represent accretion of the outer planet.

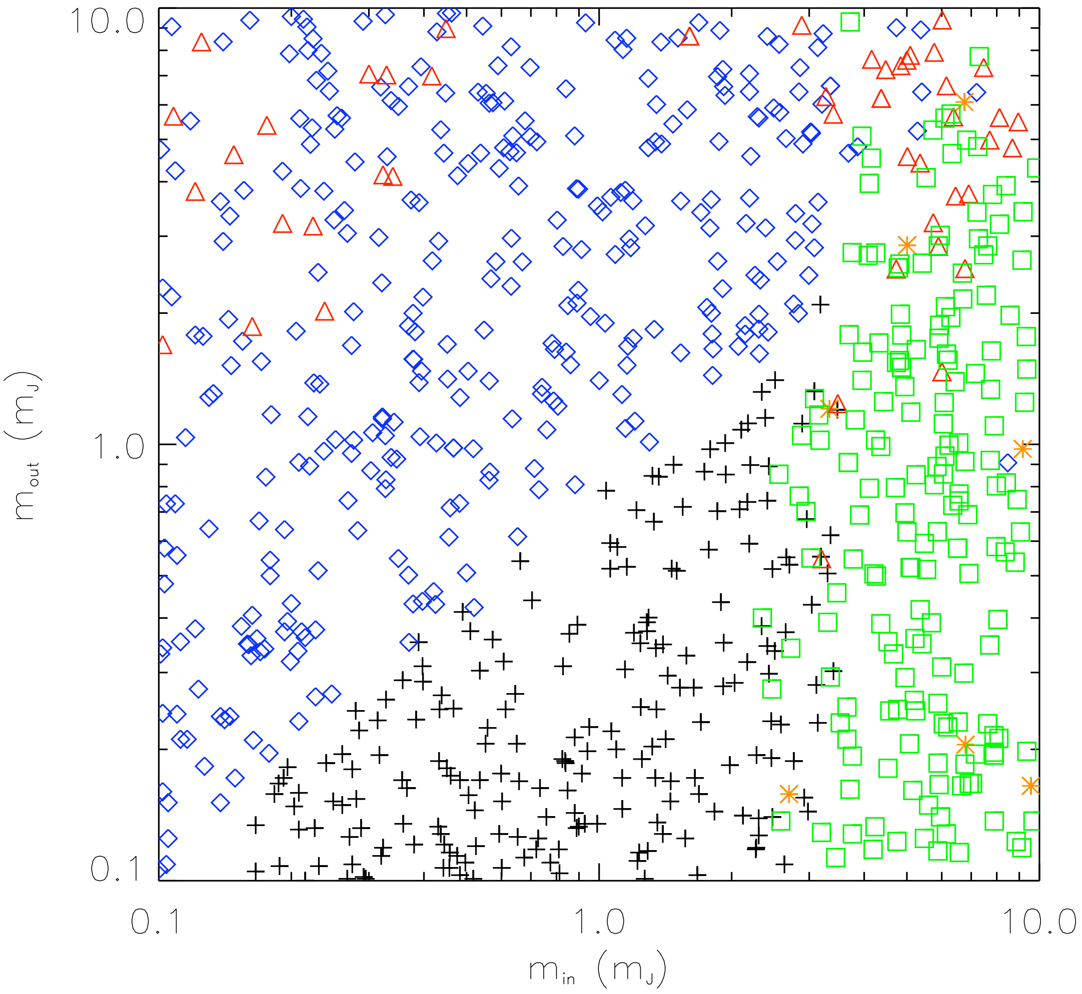

Figure 4.4. End states as a function of the planetary masses for eccentricity damping time scale τ_{ed} = 0.1 Myr. (Compare with Fig. 4.3). Each symbol in this figure represents the outcome of a simulation with the mass of the outer planet plotted as a function of the mass of the inner planet. All of the simulations depicted here use the log-random IMF, the standard starting configuration in which the outer planet begins outside the 3:1 resonance, and eccentricity damping time τ_{ed} = 0.1 Myr. The different symbols correspond to different outcomes: open blue diamonds represent accretion of the inner planet, open green squares denote ejection of the outer planet, open red triangles represent ejection of the inner planet, crosses denote survival of both planets, and orange star symbols represent accretion of the outer planet.

Table 4.2. Planet Masses (in m_J).

$\tau_{\rm ed}$	Ejectors	Ejectees	Accreted	Acc. Surviver	Both Survive
Linear IMF					
0.3 Myr	3.7 ± 0.9	2.5 ± 1.4	1.0 ± 0.6	3.3 ± 1.1	1.3 ± 0.8
1.0 Myr	3.6 ± 1.0	2.2 ± 1.4	0.8 ± 0.7	3.3 ± 1.1	1.8 ± 1.1
3.0 Myr	3.5 ± 0.9	2.2 ± 1.5	0.7 ± 0.5	3.4 ± 1.1	1.8 ± 1.0
Log IMF					
0.1 Myr	5.7 ± 1.9	1.6 ± 1.9	0.9 ± 1.0	3.3 ± 2.7	0.8 ± 0.8
0.3 Myr	5.2 ± 2.4	1.8 ± 2.1	0.6 ± 0.6	3.9 ± 2.8	0.7 ± 0.7
1.0 Myr	4.9 ± 2.4	1.8 ± 2.1	0.5 ± 0.5	4.0 ± 2.7	0.8 ± 0.7
∞	5.0 ± 2.4	1.8 ± 1.9	0.5 ± 0.4	3.7 ± 2.8	0.9 ± 1.0
Log IMF (2:1)					
1.0 Myr	4.8 ± 2.2	1.6 ± 2.2	0.65 ± 0.9	3.8 ± 2.6	0.8 ± 0.7

Table 4.3. Semi-major Axes of Remaining Planets (in AU).

$\tau_{\rm ed}$	Ejectors	Acc. Surviver	Both Survive	All Survivors
Linear IMF				
0.3 Myr	2.3 ± 1.8	0.2 ± 0.2	0.4 ± 0.4	1.2 ± 1.2
1.0 Myr	2.5 ± 2.7	0.7 ± 1.6	0.4 ± 0.3	1.4 ± 0.5
3.0 Myr	2.3 ± 1.1	1.0 ± 1.1	0.6 ± 0.4	1.4 ± 0.9
Log IMF				
0.1 Myr	3.1 ± 6.2	0.2 ± 1.4	0.5 ± 0.4	1.0 ± 3.1
0.3 Myr	2.5 ± 0.9	0.2 ± 0.4	0.4 ± 0.4	0.9 ± 0.6
1.0 Myr	2.6 ± 2.7	0.6 ± 0.6	0.5 ± 0.4	1.1 ± 1.4
∞	2.7 ± 1.9	1.5 ± 0.9	1.3 ± 0.7	1.7 ± 1.2
Log IMF (2:1)				
1.0 Myr	2.6 ± 0.9	0.5 ± 0.9	0.5 ± 0.4	1.0 ± 1.7

For the log-random IMF, which is closest to producing the observed mass distribution, roughly one third of the systems retain both planets within 30 AU at the end of the 1 Myr integration time (see Table 4.1). For comparison, about 10 – 20 percent of the observed extrasolar planetary systems show multiple planets (to date – see www.exoplanets.org). However, the theoretical systems that retain multiple planets tend to have planetary masses that are smaller than average (Table 4.2) and such low mass planets may have escaped detection. In addition, as many as half of the systems observed with one planet may contain additional bodies (Fischer et al., 2001). More data is necessary to determine whether or not this issue is problematic

Table 4.4. Eccentricities of Remaining Planets.

$\tau_{\rm ed}$	Ejectors	Acc. Surviver	2-Planet Systems	All Survivors
Linear IMF				
0.3 Myr	0.5 ± 0.3	0.3 ± 0.2	0.5 ± 0.3	0.4 ± 0.3
1.0 Myr	0.4 ± 0.3	0.5 ± 0.3	0.7 ± 0.2	0.5 ± 0.2
3.0 Myr	0.4 ± 0.3	0.4 ± 0.3	0.8 ± 0.1	0.6 ± 0.2
Log IMF				
0.1 Myr	0.2 ± 0.3	0.04 ± 0.07	0.3 ± 0.2	0.2 ± 0.2
0.3 Myr	0.3 ± 0.2	0.1 ± 0.2	0.4 ± 0.3	0.3 ± 0.2
1.0 Myr	0.3 ± 0.3	0.3 ± 0.3	0.7 ± 0.2	0.5 ± 0.2
∞	0.3 ± 0.3	0.4 ± 0.4	0.8 ± 0.1	0.6 ± 0.2
Log IMF (2:1)				
1.0 Myr	0.3 ± 0.3	0.4 ± 0.2	0.6 ± 0.21	0.5 ± 0.2

for the theory; our model contains only two planets, for instance, while solar systems, as we well know, can possess more than two planets.

4.2.3 Behavior of Resonance Angles

As shown above, the period ratio of the two planets quickly and smoothly approaches an integer value, often 3, and thus approaches a mean motion resonance. As one benchmark, 70% of the systems studied here spend at least 10,000 years near the 3:1 resonance. This result is supported by the behavior of the 3:1 resonance angles over time. To illustrate this behavior we focus on the three angles

$$\phi_1 = 3\lambda_2 - \lambda_1 - 2\varpi_1, \qquad \phi_2 = 3\lambda_2 - \lambda_1 - \varpi_2 - \varpi_1, \qquad \phi_3 = 3\lambda_2 - \lambda_1 - 2\varpi_2, \tag{4.2}$$

where the λ_j are the mean longitudes and the ϖ_j are the longitudes of pericenter (Murray & Dermott, 2001). Note that a complete description of the 3:1 resonance requires three additional angles, although their behavior is similar to those considered here. For the representative case of two planets of one Jupiter mass each, Fig. 4.5 shows how the system passes through different versions of the 3:1 resonances. For example, between 50 and 200 thousand years, the first three angles librate about values that are 120 degrees apart. Then, between 0.25 and 1 Myr, the first and third angles librate about an angular value that is 180 degrees different from the second.

4.5

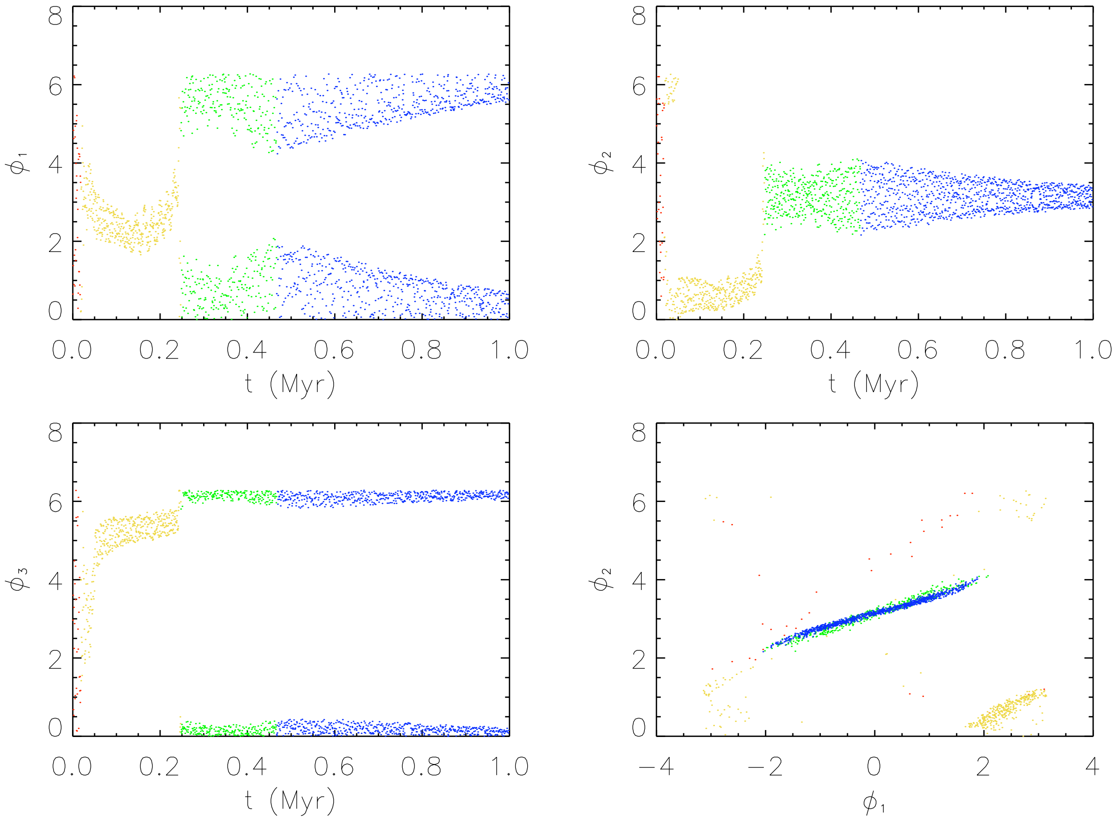

Figure 4.5. Representative behavior of resonance angles for a 3:1 mean motion resonance. The first three panels show the time evolution of the 3:1 resonance angles for a representative simulation in which two equal mass planets with $m_P = 1.0\ m_J$ migrate inward together and approach the 3:1 mean motion resonance. Colors have no significance except to help identify regions in the last plot with different spans of time. As shown here, the resonance angles exhibit complex behavior and exhibit large librations about the resonance; nonetheless, a well-defined resonant condition is reached. The lower right panel shows two of the resonance angles plotted against each other. For most of the evolution, $t > 0.25$ Myr, the system librates around the point $\phi_1 = 0$, $\phi_2 = \pi$.

A wide range of behavior is displayed in the time evolution of the resonance angles, although the overall defining trend can be described as follows (see also Beaugé et al., 2003; Ferraz-Mello et al., 2003; Lee, 2004): The planets tend to approach a mean motion resonance, but generally exhibit large librations about a perfect resonant condition. Two effects contribute to this behavior. The circumstellar disk exerts a torque on the outer planet and acts to move the planet inward and away from resonance; although the inner planet experiences a greatly reduced torque, it is not enough to keep up, and the two planets must continually readjust their orbital elements to maintain a resonant condition. In addition, the planets are massive enough and sufficiently close together so that they tend to excite the orbital eccentricities; this continual pumping up of the eccentricities can eventually act to make the system unstable. Notice that when the planets have low masses, they tend to stay in resonance longer. Indeed, at the end of the simulations, the subset of solar systems that retain both planets over the entire 1 Myr time period have a much lower average mass (see Table 4.2, Figs. 4.3 and 4.4, and the previous subsection).

Although most of these two-planet systems spend some of their evolutionary time in states with period ratio near 3:1, a substantial fraction of the systems pass through the 3:1 resonance and approach a 2:1 period ratio. One should keep in mind that a rational period ratio is a necessary, but not sufficient, condition for being in a mean motion resonance. For the ensemble of simulations studied here, we have kept track of the time for which the planets display period ratios near 3:1 and near 2:1 (specifically, period ratios within 3 ± 0.15 and 2 ± 0.15, respectively). The results are compiled in Table 4.5. The first four columns give the percentage of the time spent near each resonance, where the first value in each table entry corresponds to the 2:1 resonance and the second value to the 3:1 resonance. Here, for the first four columns of results, the percentage is calculated by integrating up the total time that any planet in the given ensemble spends near the resonance and then dividing by the total time that the ensemble of planets resides in the simulations. Notice that this figure of merit is different from that obtained by finding the percentage of time that each individual planet spends near resonance, and then averaging that fraction over the planets; this latter quantity is given in the last column in Table 4.5 for the total samples (including all outcomes) for each planetary IMF.

For the linear IMF, Table 4.5 indicates that planets spend about 70 percent of their evolutionary time with period ratios of 3:1 and only about 20 percent of their

Table 4.5. Percent of Total Time Spent in 2:1/3:1 Resonances.

$\tau_{\rm damp}$	TimeStop	Eject	Accrete	Total	Total(alt)
Linear IMF					
0.3 Myr	47/50	2/83	18/69	22/67	12/73
1.0 Myr	25/72	9/69	20/68	20/70	13/70
3.0 Myr	21/77	11/68	19/67	19/73	13/71
Log IMF					
0.1 Myr	64/32	10/61	40/54	49/44	34/52
0.3 Myr	70/25	8/63	33/46	51/35	33/46
1.0 Myr	70/26	17/55	34/46	55/34	37/44
∞	62/33	15/56	43/37	51/37	32/46
Log IMF (2:1)					
1.0 Myr	100/0	94/0.3	100/0	100/0	94/0.1

time with ratios near 2:1. The planets that survive the longest (from the simulations that reach the stopping time of 1 Myr without losing a planet) tend to reach the 2:1 resonance (see below). As a result, the resonance fractions obtained by time averaging over the whole ensemble of planets (the percentages given in column 4 in Table 4.5) are more weighted toward the 2:1 resonance than the fractions obtained by finding the individual resonance time fractions and then averaging (the alternate percentages given in column 5). Similarly, for the log-random IMF, the systems spend an average of 53 percent of their time with 2:1 period ratios and 38 percent of their time with 3:1 period ratios (averaged over the four values of $\tau_{\rm ed}$). The main difference between the two IMF choices is that the linear IMF has larger planets and mass ratios closer to unity; our numerical results indicate that this combination is more conducive to keeping the planets locked in the 3:1 resonant condition. For those systems that stay near a period ratio of 3:1 for more than 80 percent of their evolutionary time, the distribution of mass ratios m_{out}/m_{in} is sharply peaked near unity, with a long tail to larger values. As a result, equal mass planets tend to stay near resonance longer. Systems with with the inner planet more massive than the outer planet tend to move away from resonance, often by ejecting the smaller planet, whereas systems with more massive outer planets often drive the smaller inner planet into the star.

Another related result concerns the systems that survive for the entire 1 Myr time span without ejecting a planet. As mentioned above, the planets in these systems have relatively lower masses (Table 4.2). For the log-random IMF, 69 percent of the surviving systems are found with period ratios near 2:1, 28 percent of the systems show period ratios near 3:1, and the remaining 3 percent are "far" from resonance. Thus, surviving systems tend to be those that pass through the 3:1 resonance and become locked into the 2:1 resonance. As expected, the surviving systems show a mass distribution that is weighted toward lower masses compared with the original log-random distribution (which is roughly consistent with the mass distribution of observed planets). The distribution of mass ratios m_{out}/m_{in} is slanted toward values less than unity so that surviving systems tend to have the outer planet less massive than the inner planet. For the linear IMF, the results are somewhat different, where 67 percent of the surviving systems have period ratios near 3:1 and the remaining 33 percent have 2:1 period ratios (see also Figs. 4.3 and 4.4).

4.2.4 Distributions of Orbital Elements

For each class of starting configuration, the simulations result in a distribution of final system properties. The starting states can be characterized by the planetary IMF, the eccentricity damping time scale $\tau_{\rm ed}$, and the initial period of the outer planet P_{out} (although most of our simulations use $P_{out} \approx 3.736 P_{in}$). Each triple (IMF, $\tau_{\rm ed}$, P_{out}) thus leads to distributions of final orbital elements, as reported in Tables 4.2 – 4.4. For each end state of the simulations (ejection, accretion, etc.), these tables characterize the distributions of mass, eccentricity, and semi-major axes, by specifying their mean values and widths. One must keep in mind the probabilistic nature of this type of problem. The simulations act as a mapping from an initial space to a final one,

$$({\rm IMF}, \tau_{\rm ed}, P_{out}) \;\rightarrow\; \Big\{ f_{out}, f_a(a), f_\epsilon(\epsilon), f_i(i), f_m(m_P), \dots \Big\}, \qquad (4.3)$$

where the entries on the left hand side are numbers (single values) and the entries f_j on the right hand side are distributions of values (e.g., f_{out} represents the fractional occurrence of each outcome, $f_a(a)$ is the distribution of semi-major axes, etc.).

The resulting distributions of orbital elements, and planet masses are plotted in Figs. 4.6 and 4.7. For comparison, these figures include the distributions of planet properties from the observed sample (see Section 4). The lower right panel of each figure shows the mass distribution of the planets that survive to the end of the simulations. The observed distribution of planets provides us with $m_P \sin i_{obs}$ (rather than m_P); to account for this ambiguity, we have used the quantity $2 m_P \sin i_{obs}$ as a working mass estimate for specifying the "observed" mass distribution (notice also that the observational viewing angle is different from the usual definition of inclination angle as an orbital element so that $\sin i_{obs} \neq \sin i$). In spite of the tendency for smaller planets to be ejected, the linear IMF tends to roughly preserve its shape during the course of evolution (see Fig. 4.6). However, in comparison, the mass distribution of observed extrasolar planets has fewer high mass planets and more low mass planets and is thus closer to the log-random distribution (which we adopted as our second working IMF – see Fig. 4.7). Even with the ejection of the smaller planets, the log-random IMF model yields a final mass distribution that is close to the observed distribution. Some discrepancy occurs in the high mass tail, however, because our log-random distribution has an upper bound at $m_P = 10\ m_J$. Our model also provides a small surplus of planets in the low mass tail, relative to the observed mass distribution, although this disagreement may be the result of less frequent detection of the smallest planets.

4.6

The different sets of simulations (two planetary IMFs and four values of the eccentricity damping time scale) tend to result in relatively flat distributions of the semi-major axis (see the upper left panels of Figs. 4.6 and 4.7). For the case of no

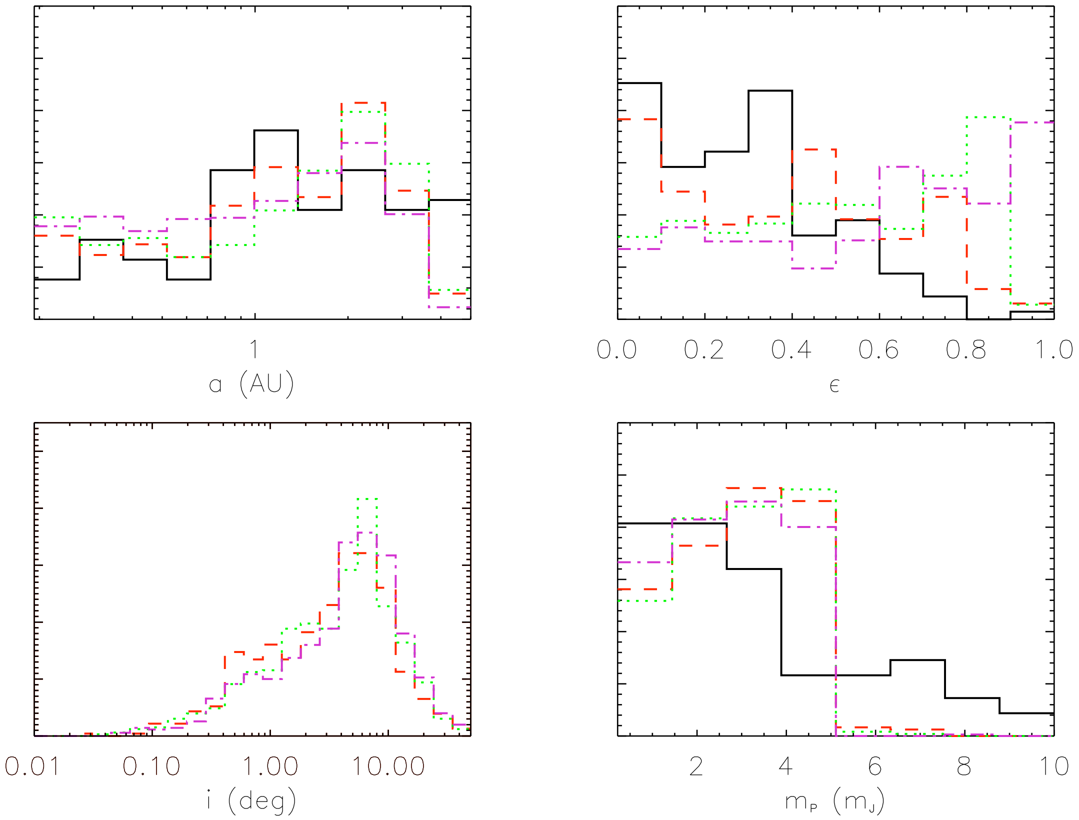

Figure 4.6. Normalized histograms of the orbital elements of surviving planets for a linear (random) planetary IMF. Vertical scale is linear and represents the relative number of planets in each bin. The upper left panel shows the distributions of semi-major axis for the observed planets (solid curve) and theoretical simulations with varying time scales for eccentricity damping: dashes ($\tau_{\rm ed} = 0.3$ Myr), dots ($\tau_{\rm ed} = 1$ Myr), and dot-dashes ($\tau_{\rm ed} = 3$ Myr). Similarly, the upper right panel shows the distributions of eccentricities and the lower left panel shows the distributions of orbital inclination angles. The lower right panel shows the distributions of masses, where the mass distribution of the observed planets (solid curve) is included for comparison; note that the random IMF for the simulations cuts off at 5 m_J.

eccentricity damping and a log-random IMF, however, the semi-major axis distribution of the surviving planets displays a broad peak near 1 AU. As the eccentricity damping is increased (more damping with a shorter time scale $\tau_{\rm ed}$), this peak becomes even broader (flattens out) and moves toward lower values of a. Because Type II migration torques are effective at moving planets inward, and because of the random element introduced into the migration process (due to different starting angles and varying effective integration times), the resulting values of semi-major axis fill the entire range covered by current observations.

4.7

The distributions of eccentricities are shown in the upper right panels in Figs. 4.6 and 4.7. As expected, the distribution of eccentricity shifts toward lower values as the level of eccentricity damping is increased (i.e., as $\tau_{\rm ed}$ decreases). The general trend is for the simulations to excite the orbital eccentricities to higher levels (averaged over the distribution) than those found in the observational sample. The exception to this rule occurs for the shortest eccentricity damping time scale $\tau_{\rm ed} = 0.1$ Myr for the log-random planetary IMF: In this class of systems, the resulting distribution of eccentricity is shifted to lower values than the observed planetary orbits. Taken at face value (ignoring the possibility of selection effects in the observational sample), this set of results argues that, within the context of this migration scenario, the eccentricity damping time scale cannot be smaller than about $\tau_{\rm ed} = 0.1$ Myr (otherwise, resulting eccentricities would be too low) or larger than about $\tau_{\rm ed} = 1.0$ Myr (otherwise, ϵ values would be too large). We will return to this issue below.

The distributions of inclination angle are shown as the lower left panels in Figs. 4.6 and 4.7. The resulting distributions of the inclination angle appear to be largely independent of the eccentricity damping time scale $\tau_{\rm ed}$ for both choices of planetary IMF. The distribution shows a well-defined peak near $i \approx 6$ degrees for the random IMF and a broader peak near $i = 3 - 5$ degrees for the log-random IMF.

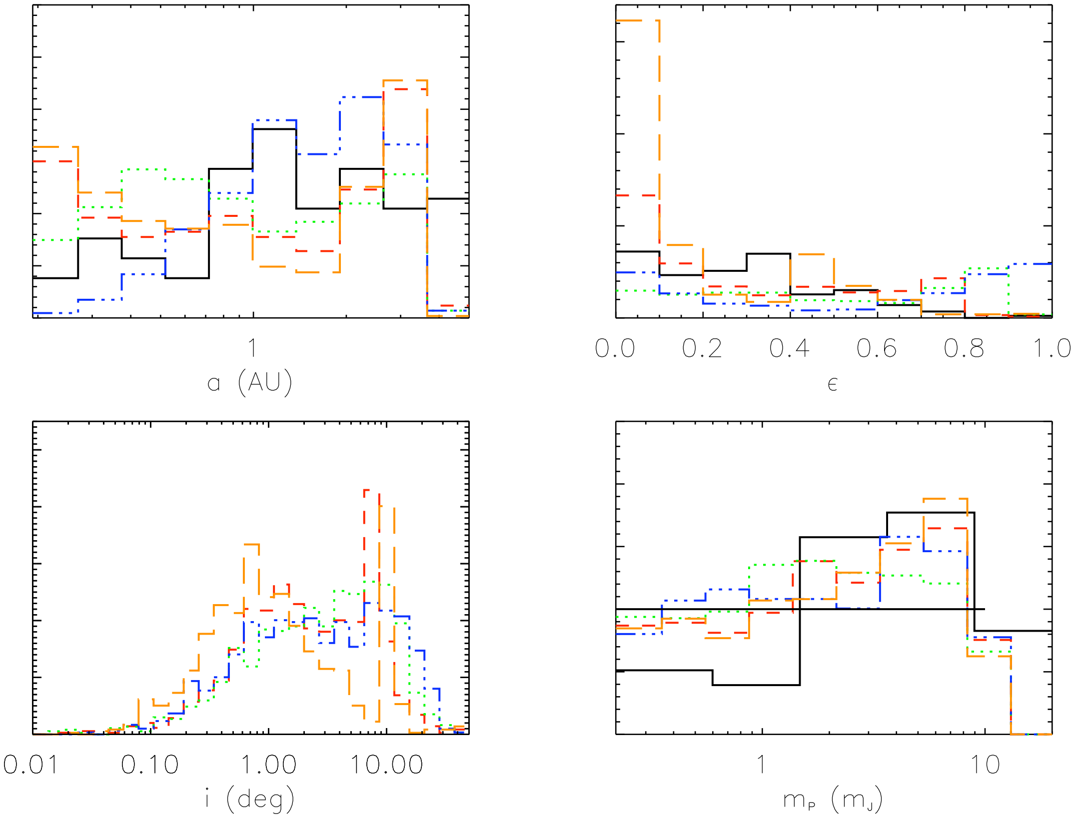

Figure 4.7. Normalized histograms of the orbital elements of surviving planets for a logarithmic (random) planetary IMF. The upper left panel shows the distributions of semi-major axis for the observed planets (solid curve) and theoretical simulations with varying time scales for eccentricity damping: long dashes ($\tau_{\rm ed}$ = 0.1 Myr), regular dashes ($\tau_{\rm ed}$ = 0.3 Myr), dots ($\tau_{\rm ed}$ = 1 Myr), and double dot-dashes ($\tau_{\rm ed} \to \infty$). Similarly, the upper right panel shows the distributions of eccentricities and the lower left panel shows the distributions of orbital inclination angles. The lower right panel shows the distributions of masses, where the solid histogram shows the distribution of observed planets and the solid horizontal line shows starting log-random distribution; note that the log-random IMF for the simulations cuts off at 10 m_J.

Although modest, these angles are significantly larger than the starting inclination angles ($|i| \leq 0.03 \approx 1.7$ degrees). For the shortest eccentricity damping time scale and the log-random IMF (which has the greatest number of small planets), however, the distribution of inclination angle is shifted somewhat toward lower values.

As a general rule, increases of the inclination angle are correlated with increases of eccentricity (consistent with the earlier studies of AL2003; Thommes & Lissauer, 2003). For this ensemble of simulations, we find that the inclination angle and the eccentricity have a linear correlation coefficient in the range $r(N) \approx 0.33 - 0.66$ for simulations that end in either ejection or accretion. Table 4.6 shows these results for the eight classes of simulations conducted in this study; also shown (in parentheses) are the numbers of simulations in the sample used to compute each correlation coefficient. For the large sample size ($N \sim 100 - 300$), these values of $r(N)$ are generally considered significant (Press et al., 1986), but the correlation is not exact. Notice that our simple treatment does not include the possible damping of inclination angle by the circumstellar disk (e.g., Lubow & Ogilvie, 2001). Such damping would move the distributions of i to smaller values, but the correlations between eccentricity excitation and inclination angle excitation would remain.

Table 4.6. Linear Correlation Coefficient between ϵ and i.

τ_{damp}	Survival	Ejection	Accretion	Total
Linear IMF				
0.3 Myr	0.62 (44)	0.53 (99)	0.61 (96)	0.50 (214)
1.0 Myr	0.064 (260)	0.43 (294)	0.57 (103)	0.31 (660)
3.0 Myr	0.061 (190)	0.39 (180)	0.76 (54)	0.27 (425)
Log IMF				
0.1 Myr	0.69 (428)	0.59 (221)	0.55 (333)	0.64 (1034)
0.3 Myr	0.58 (456)	0.53 (258)	0.57 (274)	0.54 (1013)
1.0 Myr	0.30 (566)	0.56 (248)	0.33 (224)	0.45 (1038)
∞	0.28 (398)	0.40 (228)	0.66 (238)	0.46 (867)
Log IMF (2:1)				
1.0 Myr	0.36 (198)	0.56 (80)	0.60 (98)	0.51 (379)

4.2.5 Distribution of Ejection Speeds

A substantial fraction of the planetary systems eject a planet and these planets can, in principle, be observed as free floating bodies. Table 4.1 indicates that approximately one-third of the systems will eject planets for the log-random planetary IMF, and over half of the systems with a linear IMF will eject planets. These planets have roughly Jovian mass (Table 4.2) and thus do not represent a significant mass contribution to the galaxy – in other words, the number of ejected planets is not large enough to be problematic. However, recent observations have found some evidence for very small mass brown dwarfs in stellar clusters; these objects could potentially be freely floating planets (e.g., Zapatero Osorio et al., 2000). If so, these predicted planets must be consistent with the observations.

The planets are ejected with a well-defined distribution of speeds, as shown in Fig. 4.8. For all cases considered here, the distribution displays a well-defined peak near $v_{\rm ej} = 5$ km/s and most of the distribution falls between 0.5 and 20 km/s. For comparison, the planets are ejected from orbits with semi-major axes near 3 – 7 AU, where the orbit speeds are about $11 - 17 \approx 14$ km/s. The kinetic energy carried away by the ejected planets is thus a small fraction F_E of the total. A rough estimate of this fraction is given by

$$F_E \approx \frac{{v_{\rm ej}}^2/2}{|E|} = \frac{a{v_{\rm ej}}^2}{GM_*} \approx (5/14)^2 \approx 0.13\,, \tag{4.4}$$

where $v_{\rm ej}$ is the ejection speed and a is the semi-major axis from which ejection occurs. This finding vindicates the assumption that ejected planets tend to leave on (nearly) zero energy orbits (AL2003; Marzari & Weidenschilling, 2002).

4.8

We can understand the general form of the distribution of ejection speeds with the following heuristic argument: Ejections occur through close encounters between the planets. Let b denote the impact parameter of these interactions, so that the

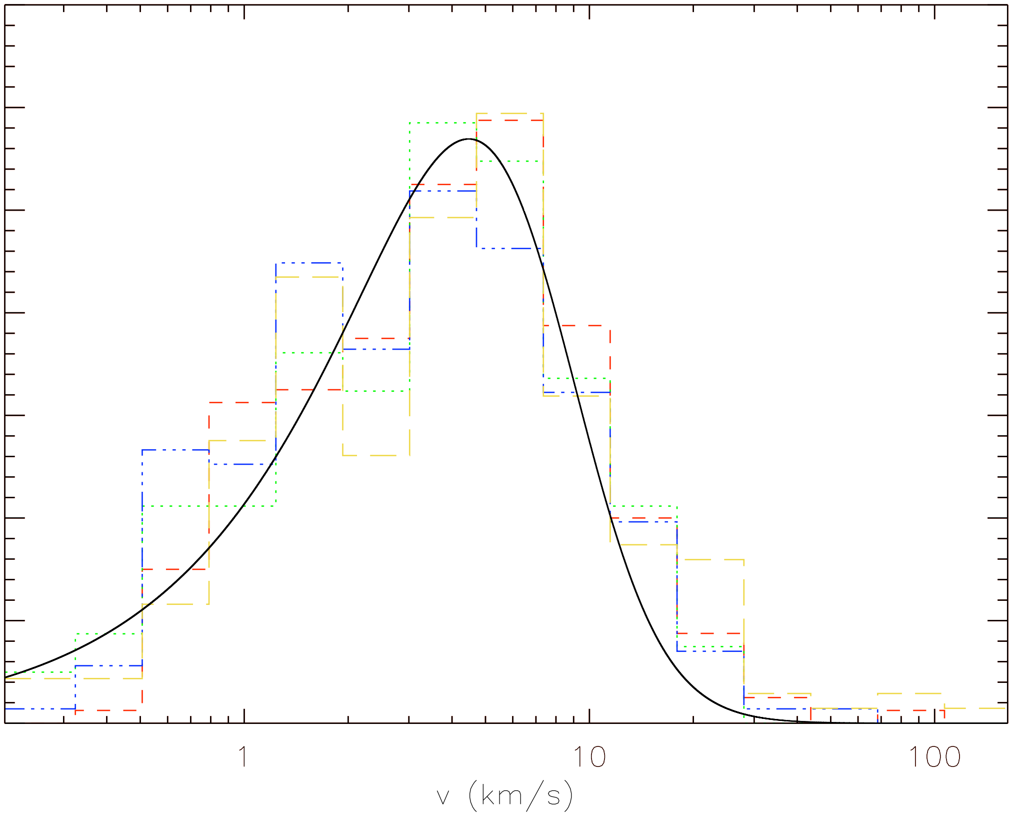

Figure 4.8. Distribution of ejection velocities for planets that are ejected during the epoch of migration. The distribution is shown for the log-random planetary IMF and for four values of the eccentricity damping time scale: $\tau_{\rm ed}$ = 0.1 Myr (yellow long-dashed curve), $\tau_{\rm ed}$ = 0.3 Myr (red short-dashed curve), $\tau_{\rm ed}$ = 1.0 Myr (green dotted curve), and $\tau_{\rm ed} \to \infty$ (blue dot-dashed curve). The four distributions are normalized to the same value, with the vertical scale arbitrary. The smooth solid curve shows the (normalized) analytic approximation to the distribution of ejection speeds (as derived in the text). All speeds are given in km/s.

ejection speed can be written

$$\frac{1}{2}{v_{\rm ej}}^2 = \alpha \frac{G\langle m \rangle}{b} - \frac{GM_*}{2a} \,, \tag{4.5}$$

where a is the semi-major axis of the ejected planet (before the interaction), $\langle m \rangle$ is an average mass of the remaining planet, and α is a dimensionless factor of order unity (which depends on the geometry of the interaction). If we define a velocity scale $v_0^2 \equiv GM_*/a$ and a length scale $r_0 \equiv 2\alpha(\langle m \rangle/M_*)a$, the ejection speed can be written in the form

$$u = \left[\frac{1}{\xi} - 1\right]^{1/2} \,, \tag{4.6}$$

where $u \equiv v_{\rm ej}/v_0$ and $\xi \equiv b/r_0$. If we assume that the impact parameter is distributed according to $dP \propto bdb$ (the target area is circular), the probability distribution for the ejection speed takes the form

$$\frac{dP}{du} = \frac{4u}{(1+u^2)^3} \,. \tag{4.7}$$

As written, this probability distribution is normalized to unity over the full range of dimensionless ejection speeds $0 \le u \le \infty$. In practice, the impact parameter has a minimum value given by the radius of the (ejector) planet, $b_{\rm min} = r_P$, and this value implies a corresponding cutoff in the ejection speed $v_{\rm max} \approx v_0\sqrt{r_0/r_P}$. However, the distribution falls rapidly at high speeds so that the value of this cutoff is relatively unimportant. Equation (4.7) has the same form as the distributions of ejection speeds found in the simulations (as shown in Fig. 4.8). The model distribution has been normalized to agree with the simulations (note that the fraction of systems that experience ejection must be determined numerically). The distributions agree if the velocity scale is taken to be $v_0 \approx 11$ km/s, which implies that ejections (mostly) occur near the beginning of the evolution (the outer planets, which are more often ejected, start near 7 AU where $(GM_*/a) \approx 11$ km/s). Finally, we note that the simple formula derived above assumes a single value for the velocity scale. Since the planets can migrate inwards to different semi-major axes before ejection, the true distribution will have a range of v_0 values; although this range is relatively narrow in the present application, this effect tends to broaden the distribution of ejection speeds relative to equation (4.7).

Under a reasonable set of assumptions, we can estimate the expected population of free floating planets within a typical birth aggregate. The velocity dispersion for a young star forming group/cluster is about 1 km/s (Lada & Lada, 2003; Porras et al., 2003). Given the distribution of ejection speeds (Fig. 4.8), the majority of ejected planets are predicted to be unbound to their birth clusters. As a first approximation, suppose that every solar system produces migrating planets and that one third of them eject planets (Table 4.1). Of the ejected planets, about one tenth remain bound to the group/cluster with ejection speeds $v_{\rm ej} < 1$ km/s. For every 30 stars in the cluster, it will thus contain one freely floating planet that is gravitationally bound. The unbound planets have ejection speeds of $\sim$5 km/s. For an average cluster size of $R \sim 1$ pc, the ejected planets would remain within their birth clusters for $\sim$0.2 Myr. If the young group/cluster remains intact for 10 Myr, then 1/50th of the unbound planets will reside within the group/cluster at any given time, and the cluster will contain one unbound planet for every 150 stars. Given a fiducial group/cluster size of $N_* \approx 300$ stars (Lada & Lada, 2003; Porras et al., 2003), stellar birth aggregates will have $\sim$ 10 freely floating planets at low speeds ($v_{\rm ej} \leq 1$ km/s) and $\sim$ 2 freely floating planets at higher speeds ($v_{\rm ej} \sim 5$ km/s) at any given time ($t \leq 10$ Myr).

4.3 Comparison with Observed Extrasolar Planets

In order for a migration mechanism to be considered fully successful, it must produce distributions of orbital elements that are consistent with those of observed extrasolar planets. Given that the observed distributions are incomplete and contain biases, however, and that additional orbital evolution must take place between the end of our simulations and the $\sim 1-6$ Gyr ages of the observed systems, this type of comparison remains preliminary. In this section, we briefly discuss the limitations of the data set and outline how the distributions of orbital elements can evolve after the end of our simulations. We then show that this migration mechanism meets the necessary (but not sufficient) condition of being able to fill the $a-\epsilon$ plane in a manner that is roughly consistent with presently available data.

4.3.1 Observed Sample of Extrasolar Planets

The observed sample of extrasolar planets used in this chapter is taken from the California and Carnegie Planet Search Website.[1] In order to compare theoretical results with this data set, some of its properties must be taken into account. All planet searches using radial velocity surveys are subject to selection effects. Since the surveys are subject to a minimum (detectable) velocity amplitude, planetary companions that induce reflex velocities that are too small cannot be measured. This effect limits the sensitivity of the surveys to low mass planets. In addition, planets with long periods (large semi-major axes a) cannot be adequately detected because of the limited time baseline of the surveys. This latter effect thus leads to a loss of sensitivity at large a. As a benchmark, Jupiter produces a 12.5 m/s velocity variation on the Sun with a period of 12 years. The detection of a Solar System analog requires approximately $k \approx 3$ m/s precision maintained over a decade window of observing. Since this level of precision (Bernstein et al., 2003) and this time baseline are the best that are currently available, the mass and semi-major axis of Jupiter represent a rough upper limit on detectability. As a general rule, the completeness of the data set must decline with increasing semi-major axis and decreasing planet mass. The detection limit can be written in terms of the reflex velocity $k_{\rm re}$, defined by

$$k_{\rm re} \equiv \frac{m_P \sin i_{obs}}{M_*^{2/3}(1-\epsilon^2)^{1/2}} \left(\frac{2\pi G}{P}\right)^{1/3}, \tag{4.8}$$

---

[1] http://exoplanets.org/science.html

which is valid in the limit $m_P \ll M_*$. We can scale this formula to the limit quoted above, i.e., that the detection of Jupiter itself is near the present day observational threshold. The portion of the $a - \epsilon$ plane that is accessible to observations is (conservatively) delimited by the curve $a(1-\epsilon^2) \leq 5\mu^2$, where a is in AU and $\mu = m_P \sin i_{obs}$ is in Jupiter masses. The radial velocity surveys have 7 year time spans (for the latter, more complete samples) which implies a limit of about $a \leq 3.5$ AU for completeness in semi-major axis. For this value of a, the corresponding mass limit is thus $\mu \geq 0.84$ $(1-\epsilon^2)^{1/2}$. As a result, for the moderate eccentricities observed, $\langle \epsilon \rangle \approx 0.3$, the sample is expected to nearly complete out to $a = 3.5$ AU for $m_P \sin i_{obs} \geq 0.8 m_J$, and nearly complete at $a = 1$ AU for $m_P \sin i_{obs} \geq 0.43 m_J$. At the low end of our planetary IMF, $m_P \sim 0.1 m_J$, the observed sample is expected to be missing planets.

For planets detected with incomplete data sampling, the derived orbital eccentricities are subject to uncertainties. If a planet has extremely low eccentricity, then noise in the radial velocity data stream can mimic the signature of small eccentricities. On the other hand, extrasolar planets with the highest eccentricities, say $\epsilon > 0.8$, may be subject to an additional bias that makes them hard to detect using available strategies, which are sparsely sampled in time (due to limited telescope resources). Planets on high eccentricity orbits spend most of their time out near apstron, where they produce little radial velocity variation. Unless the system is observed when the planet is near periastron, it is difficult to determine the true eccentricity. Even when such a planet is detected, the analysis can underestimate the eccentricity until enough data has been obtained to provide full orbital phase coverage (e.g., see Naef et al., 2001, and the case of HD 80606). However, this bias can be eliminated by sufficient observational coverage and relatively few of the planets already detected should suffer from this effect (D. Fischer, private communication). The eccentricities of multiple planet systems can also vary with time through secular interactions (analogous to the secular eccentricity variations of Jupiter and Saturn). The observed eccentricity distribution of the extrasolar planets is thus a particular sampling of a larger underlying distribution. The observed eccentricity values can be either lower or higher than the mean values sampled over a secular cycle; although this effect can influence the interpretation of a particular eccentricity value, it will not affect the overall distribution of eccentricity of interest here.

4.3.2 Additional Evolution of the Orbital Elements

The orbital elements of the planets will, in general, continue to evolve after the end of the simulations presented in the previous section. In order to compare the theoretical results of this migration scenario with the orbital elements of observed extrasolar planets, this additional evolution should be taken into account. In this section we discuss two physical processes – continued orbital evolution driven by the circumstellar disk (with time scale $\sim$ 1 Myr) and longer term circularization due to interactions of close planets with the star (with time scale $\sim$ 1 Gyr).

The simulations end when a planet is ejected or accreted, a collisions take place, or after a fiducial time span of 1 Myr. In general, however, the disk will not lose its ability to drive migration at exactly the same time that the simulations are stopped. Suppose that the disk continues to drive Type II migration (and eccentricity damping) over a time span Δt. The orbital elements will evolve from their values (a_0, ϵ_0) at the end of the numerical simulations to new values given by

$$a_f = a_0 \, \mathrm{e}^{-\Delta t/\tau_{\rm damp}} \qquad \text{and} \qquad \epsilon_f = \epsilon_0 \, \mathrm{e}^{-\Delta t/\tau_{\rm ed}} \, . \tag{4.9}$$

Since the migration time $\tau_{\rm damp}$ and eccentricity damping time $\tau_{\rm ed}$ are determined for a given simulation, the distribution of values for the additional migration time Δt determines the final distribution of orbital elements.

Unfortunately, the correct choice of the Δt distribution is not known. The numerical experiments begin with the planets already formed, so the disk has already been around for some time before the clock starts, and this lead time will vary from system to system. In fact, within the core accretion scenario of planet formation, theories often have trouble forming giant planets while the disk retains its gas (e.g., Kornet et al., 2002, suggest a formation time of about 3 Myr), which leaves little time for migration. The planets with the largest masses in our numerical simulations lead to the shortest integration times, but these same planets are expected to have the longest formation times. Astronomical observations show that circumstellar disks have lifetimes in the range 3 – 6 Myr (e.g., Haisch et al. 2001), significantly longer than the ~ 1 Myr time spans of the integrations. However, this range of observed disk lifetimes represents the time span over which the disk exhibits observational signatures. The time over which the disk is sufficiently massive to drive (Type II) planet migration will be significantly shorter. In light of these uncertainties, this chapter explores a set of algorithms to account for additional evolution of the orbital elements by the disk, i.e., a set of simple, but well-defined, distributions for the remaining migration time Δt.

The system evolution discussed thus far produces orbital elements that apply to system ages of a few Myr, immediately after planets have finished forming and the disk has lost its ability to drive migration. Longer term evolution can also take place. On time scales $\sim 1 - 6$ Gyr characteristic of the stellar ages in observed extrasolar planetary systems, tidal interactions with the star act to circularize close orbits. In the absence of other processes, the eccentricity of a planetary orbit decays with a time scale $\tau_{\rm circ} = -\epsilon/\dot{\epsilon}$. Here we write this time scale in an approximate form (see Goldreich & Soter, 1966; Hut, 1981; Wu & Goldreich, 2002):

$$\tau_{\rm circ} \approx \frac{2}{21}\frac{Q}{k_2}\left(\frac{a^3}{GM_*}\right)^{1/2}\frac{m_P}{M_*}\left(\frac{a}{R_P}\right)^5 (1-\epsilon^2)^{13/2}[f(\epsilon^2)]^{-1}\,, \tag{4.10}$$

where $Q \approx 10^5 - 10^6$ is the tidal quality factor, $k_2 \approx 1/2$ is the tidal Love number, and $R_P \approx R_J \approx 7 \times 10^9$ cm is the radius of the planet (notice that this radius is smaller than that used for the collision cross section in the simulations because the planets will contract over the longer time spans considered here). This form includes the essential dependence of the circularization time scale on eccentricity, where $f(\epsilon^2)$ is a rather complicated function of ϵ (defined by eqs. [9–12] of Hut, 1981). Evaluation of this time scale for representative values of the parameters indicates that

$$\tau_{\rm circ} \approx \; 1{\rm Gyr} \left[a/(0.05\,{\rm AU})\,(1-\epsilon^2) \right]^{13/2} [f(\epsilon^2)]^{-1} \, . \tag{4.11}$$

As a result, orbits with $a \le 0.05$ AU are expected to be (nearly) circularized, and orbits with somewhat larger a will experience a substantial decrease in eccentricity. Although a number of additional processes can take place (e.g., orbital decay and stellar spinup – see Lin et al., 2000), the leading order effect is loss of eccentricity at constant angular momentum (see also Goldreich & Soter, 1966; Hut, 1981; Wu & Goldreich, 2002). Here we numerically integrate the (nonlinear) evolution equation for eccentricity over the stellar ages t_*, which are assumed to lie in the range $t_* = 1-6$ Gyr. In the following subsection, we apply this correction to the theoretical data set in order to compare with observations, although only the closest orbits are affected.

4.3.3 Comparison of Theory and Observation

One way to evaluate the effectiveness of this migration mechanism is to compare the resulting two-dimensional distribution of orbital elements in the $a - \epsilon$ plane with those of the observed extrasolar planets. This subsection presents such a comparison in systematic fashion. For all cases discussed here, we use the log-random IMF, as it closely mirrors the observed mass distribution of extrasolar planets. The number of theoretical planets is taken to be equal to the number in the observed sample, where the theoretical planets are chosen randomly from the ensemble of simulations. We then produce $a - \epsilon$ diagrams for each value of the eccentricity damping time scale $\tau_{\rm ed}$ = 0.1, 0.3, 1.0 Myr, and $\tau_{\rm ed} \to \infty$. Within this format, the results are presented for a collection of possible corrections for additional evolution of the orbital elements and selection effects, as outlined above.

The first comparison in shown in Fig. 4.9, which shows the $a - \epsilon$ plane for observed and theoretical planets, with no corrections applied for possible additional evolution. The location of the observed extrasolar planets in the $a - \epsilon$ plane are marked by the star symbols, whereas the results of the theoretical simulations are marked by open squares. The four panels show the results of the four eccentricity damping time scales. The theoretical distribution of planets moves to lower values of eccentricity and to lower values of semi-major axis as the eccentricity damping time scale decreases. The lower ϵ values are a direct result of the increased effectiveness of eccentricity damping. The lower values of a occur because the increased eccentricity damping keeps the planets stable for longer times and the disk has more time to move planets inward. This figure suggests that the simulations with no eccentricity damping ($\tau_{\rm ed} \to \infty$; lower right panel) produce too many high eccentricity planets compared to the observational sample, whereas the simulations with $\tau_{\rm ed} = 0.1$ Myr (upper left panel) tend to produce planetary orbits with too little eccentricity. Nonetheless, the zeroeth order result of this comparison is that both the observed planets and the theoretical simulations fill most of the $a - \epsilon$ plane shown here (except for the case $\tau_{\rm ed} \to \infty$, which ejects planets before they move far enough inward). Nonetheless, some differences appear, and we need to explore whether or not the corrections for additional evolution described above act to bring the observational and theoretical samples into better agreement.

4.9

The discussion of Section 4.1 suggests that the observed sample is likely to be incomplete for planet masses below 0.5 m_J, with the level of incompleteness increasing with semi-major axis a. In other words, the sample is incomplete for small values of the reflex velocity $k_{\rm re}$. To determine the importance of this issue on our assessment of this migration mechanism, we present the same set of $a - \epsilon$ diagrams with a $k_{\rm re}$ cut applied; specifically, all planets in the theoretical sample with $k_{\rm re} \leq 3$ m/s have been removed from consideration. The result is shown in Fig. 4.10. No other corrections

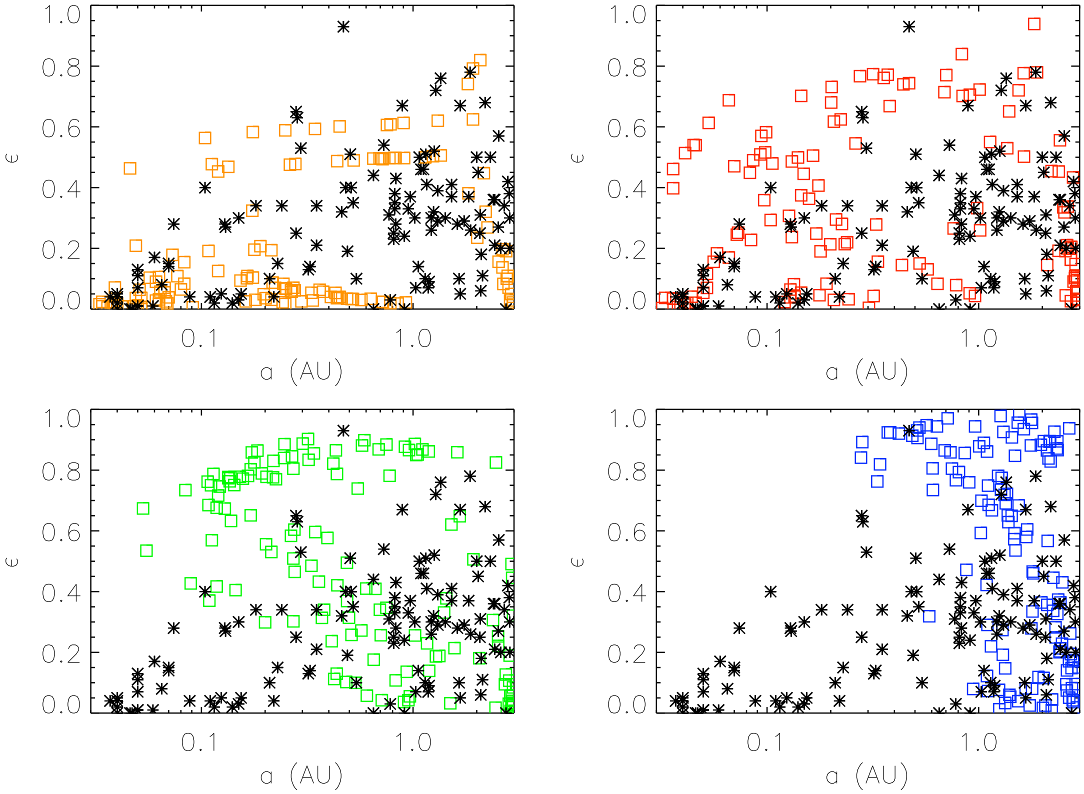

Figure 4.9. The $a-\epsilon$ plane for observed and theoretical planets, where no corrections for additional evolution have been applied to the theoretical sample. This diagram shows the semi-major axes a and eccentricities ϵ for the observed extrasolar planets as stars. The results of the theoretical simulations are shown as open squares. All of the theoretical simulations use the log-random IMF. The four panels correspond to different choices of the eccentricity damping time scale: $\tau_{\rm ed} = 0.1$ Myr (upper left), $\tau_{\rm ed} = 0.3$ Myr (upper right), $\tau_{\rm ed} = 1.0$ Myr (lower left), and $\tau_{\rm ed} \to \infty$ (lower right).

for additional evolution have been applied to the theoretical sample. Comparison of Figs. 4.9 and 4.10 indicates that mass/$k_{\rm re}$ incompleteness has only a modest effect on comparisons of the $a - \epsilon$ plane. This result makes sense because the mass range in question, roughly $m_P \le 0.5 m_J$, represents about one fourth of the starting mass range, but relatively more of the low mass planets are ejected or accreted (see Fig. 4.7 and Table 4.2). As a result, only 10 – 15 percent of the surviving planets fall in this low mass range.

4.10

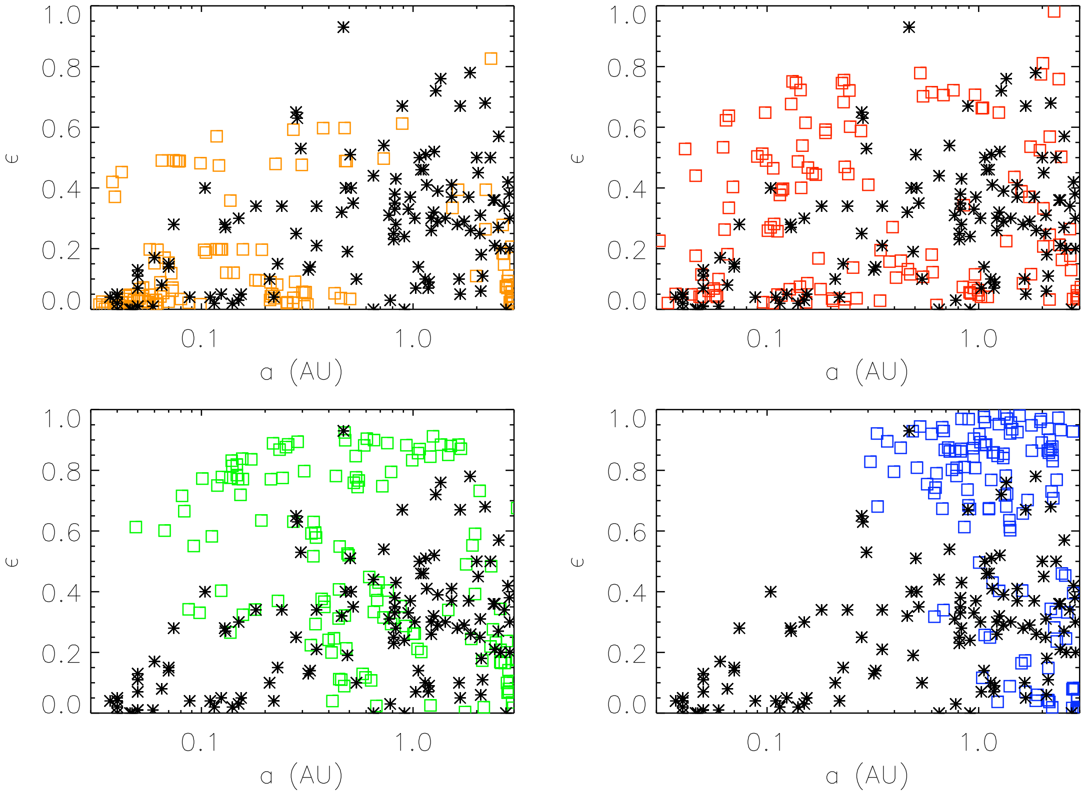

Figure 4.10. The $a - \epsilon$ plane for observed and theoretical planets, where the theoretical sample starts with a log-random IMF and has been subjected to a cut in reflex velocity $k_{\rm re}$ at 3 m/s. No corrections for additional evolution have been applied to the theoretical sample. This diagram shows the semi-major axes a and eccentricities ϵ for the observed extrasolar planets as stars. The results of the theoretical simulations are shown as open squares. The four panels correspond to different choices of the eccentricity damping time scale: $\tau_{\rm ed}$ = 0.1 Myr (upper left), $\tau_{\rm ed}$ = 0.3 Myr (upper right), $\tau_{\rm ed}$ = 1.0 Myr (lower left), and $\tau_{\rm ed} \to \infty$ (lower right).

In order to take into account additional evolution of the orbital elements beyond the end of the simulations due to the surviving circumstellar disk, we apply corrections according to equation (4.9). As discussed above, the distribution of additional migration time Δt is not well determined. As a result, we explore different algorithms for continued evolution. In the first case, we assume that the disk is able to drive migration beyond the end of the numerical simulations for an additional time given by $\Delta t = \delta t - t_{sim}$, where t_{sim} is the time at the end of the simulation, δt is a random time scale in the range 0 – 1 Myr (where negative values of Δt are set to zero, i.e., no additional evolution). This is the same algorithm used in the previous study of this migration scenario in AL2003. The resulting $a - \epsilon$ diagrams are shown in Fig. 4.11 for different choices of eccentricity damping time scale. The continued migration moves the points to lower values of both a and ϵ, and the random time element tends to spread the distributions, although the effect is relatively small (except for the case with no eccentricity damping). Nonetheless, this correction acts to bring the theoretical and observational distributions into closer agreement (although the distribution of Δt applied here is not unique).

4.11

An alternate assumption for additional evolution is that the disk has a remaining lifetime Δt that is random and independent of the previous evolution. Keep in mind that Δt is the time over which the disk has enough mass to change the orbital elements of any remaining planets; the disk may exhibit observational signatures over longer times. Fig. 4.12 shows the resulting $a - \epsilon$ diagrams for random disk lifetimes in the range $\Delta t = 0 - 0.3$ Myr. Fig. 4.13 shows the $a - \epsilon$ diagrams for random disk lifetimes in the somewhat longer range $\Delta t = 0 - 0.5$ Myr. These results are much the same as for the previous algorithm illustrated in Fig. 4.11. Any similar model of continued disk evolution will move the theoretical points to smaller values of (a, ϵ) and will spread the distributions. The magnitude of the effect (the mean value of the Δt distribution) matters more than the particular choice of algorithm (which

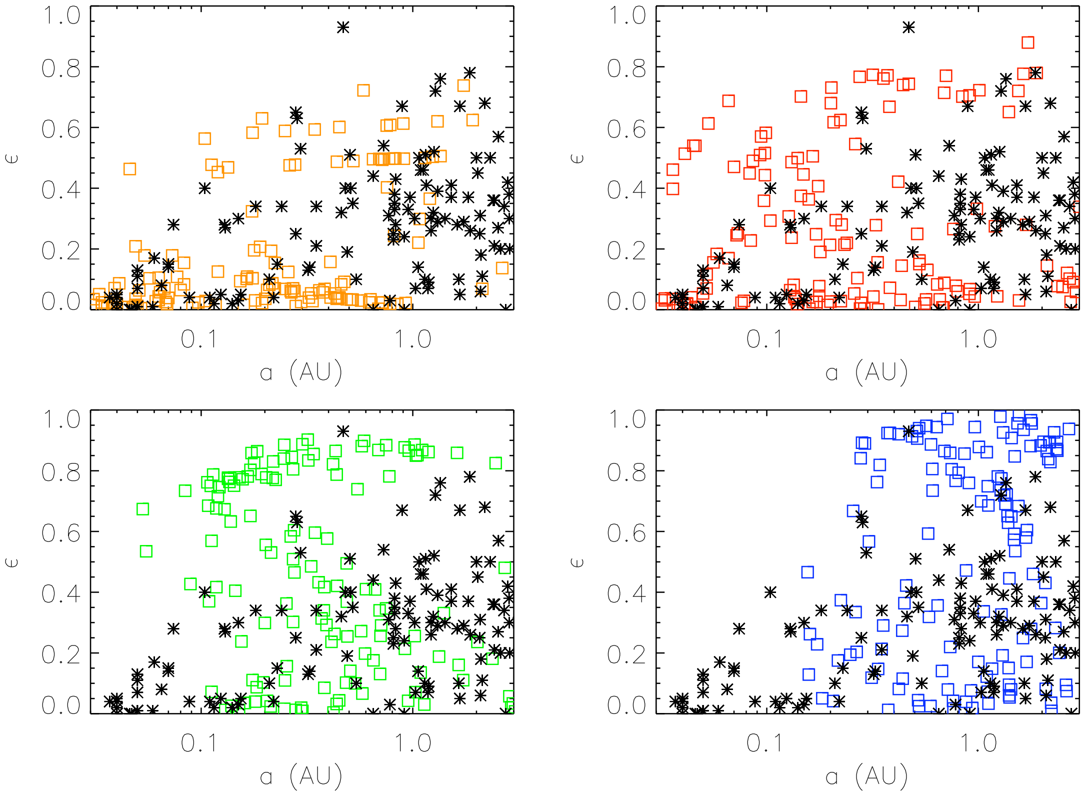

Figure 4.11. The $a - \epsilon$ plane for observed and theoretical planets, where the theoretical sample starts with a log-random IMF and has been corrected for additional orbital evolution (first alogrithm). Here the disk is assumed to exist beyond the end of the numerical simulations for an additional time given by $\Delta t = \delta t - t_{sim}$, where t_{sim} is the time at the end of the simulation, δt is a random time scale in the range $0 - 1$ Myr, and negative values are set to zero. This diagram shows the semi-major axes a and eccentricities ϵ for the observed extrasolar planets as stars. The results of the theoretical simulations are shown as open squares. The four panels correspond to different choices of the eccentricity damping time scale: $\tau_{\rm ed} = 0.1$ Myr (upper left), $\tau_{\rm ed} = 0.3$ Myr (upper right), $\tau_{\rm ed} = 1.0$ Myr (lower left), and $\tau_{\rm ed} \to \infty$ (lower right).

sets the shape of the distribution). Inspection of Figs. 4.11 – 4.13 suggests that a mean value $\langle \Delta t \rangle \approx 0.3 - 0.5$ Myr is needed to provide reasonable agreement with observations. Notice that the model allows for some interplay between this time scale and the eccentricity damping time scale – for larger $\tau_{\rm ed}$, less additional evolutionary time $\langle \Delta t \rangle$ is indicated.

4.12

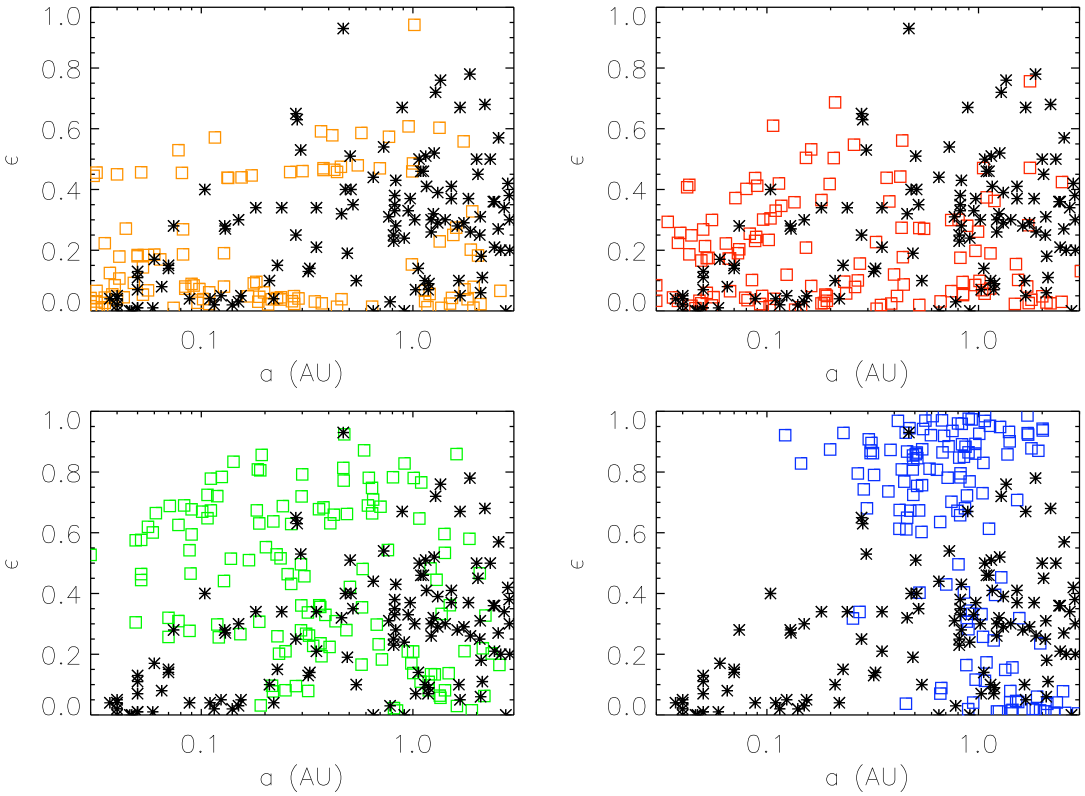

Figure 4.12. The $a - \epsilon$ plane for observed and theoretical planets, where the theoretical sample starts with a log-random IMF and has been corrected for additional orbital evolution (second algorithm). The disk is assumed to exist beyond the end of the numerical simulations for an additional time Δt, which is chosen randomly from the range 0 – 0.3 Myr. This diagram shows the semi-major axes a and eccentricities ϵ for the observed extrasolar planets as stars. The results of the theoretical simulations are shown as open squares. The four panels correspond to different choices of the eccentricity damping time scale: $\tau_{\rm ed} = 0.1$ Myr (upper left), $\tau_{\rm ed} = 0.3$ Myr (upper right), $\tau_{\rm ed} = 1.0$ Myr (lower left), and $\tau_{\rm ed} \to \infty$ (lower right).

4.13

Next we consider corrections to the orbital elements due to the longer term process

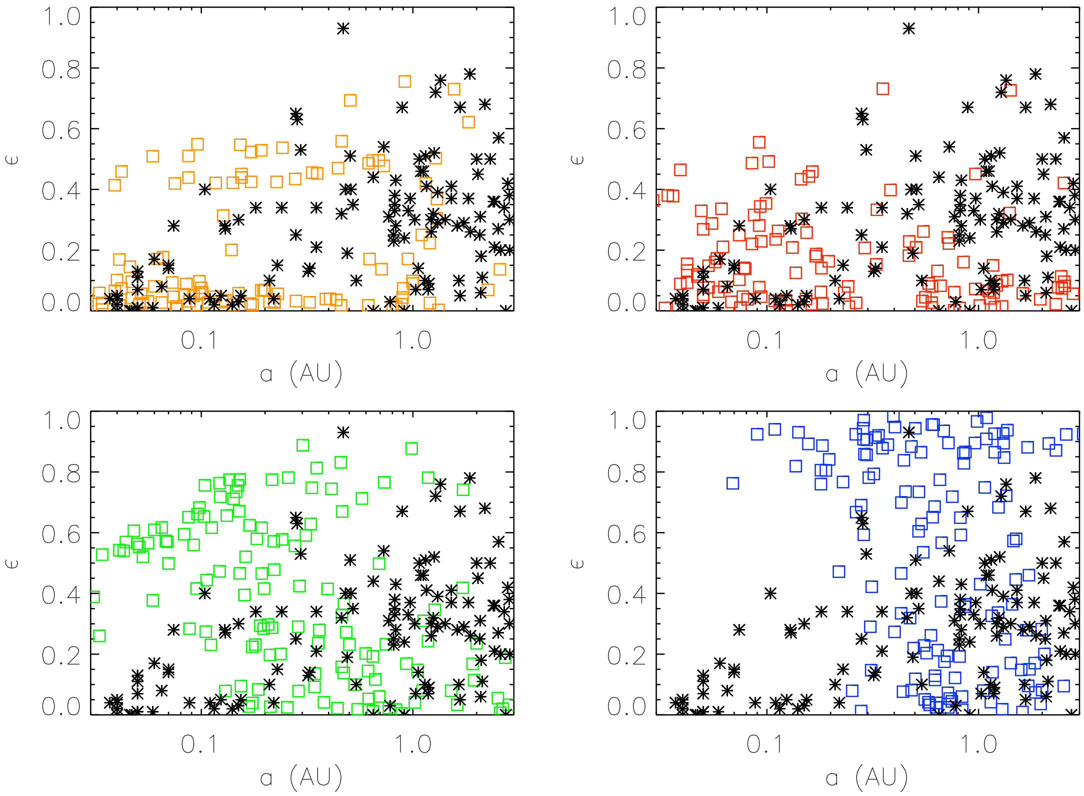

Figure 4.13. The $a - \epsilon$ plane for observed and theoretical planets, where the theoretical sample starts with a log-random IMF and has been corrected for additional orbital evolution (third aloorithm). The disk is assumed to exist beyond the end of the numerical simulations for an additional time Δt, which is chosen randomly from the range $0 - 0.5$ Myr. This diagram shows the semi-major axes a and eccentricities ϵ for the observed extrasolar planets as stars. The results of the theoretical simulations are shown as open squares. The four panels correspond to different choices of the eccentricity damping time scale: $\tau_{\rm ed} = 0.1$ Myr (upper left), $\tau_{\rm ed} = 0.3$ Myr (upper right), $\tau_{\rm ed} = 1.0$ Myr (lower left), and $\tau_{\rm ed} \to \infty$ (lower right).

of tidal circularization by the central star. To account for this effect, we integrate the differential equation $\dot{\epsilon}/\epsilon = -{\tau_{\rm circ}}^{-1}$, with the circularization time scale given by equations (4.10, 4.11). The assumed system lifetimes are assumed to be randomly distributed and lie in the range 1 – 6 Gyr, similar to the stellar ages in the observed sample. The resulting $a - \epsilon$ diagrams are shown in Fig. 4.14. The inclusion of this circularization processes cleans up an important discrepancy between the theoretical and observed orbital elements, namely the observed lack of short period planets (small a) with substantial eccentricities.

4.14

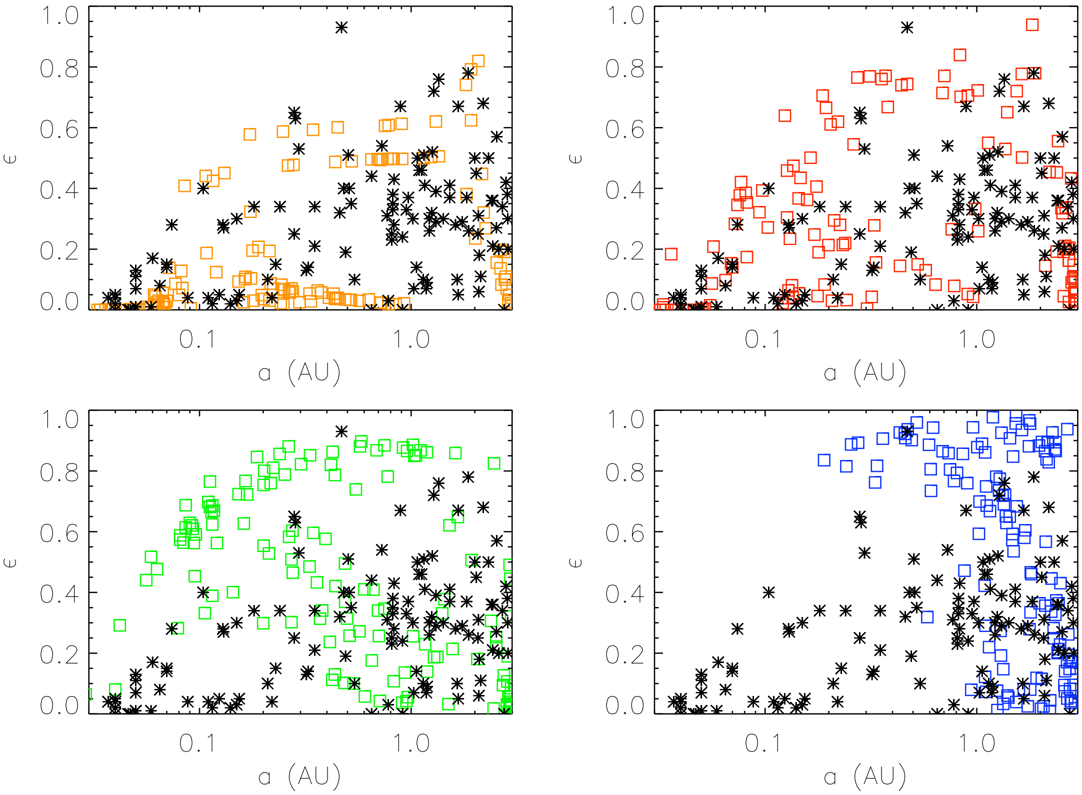

Figure 4.14. The $a - \epsilon$ plane for observed and theoretical planets, where the theoretical sample starts with a log-random IMF and has been corrected for tidal circularization over the stellar lifetime, which is assumed to lie in the range 1 – 6 Gyr. This diagram shows the semi-major axes a and eccentricities ϵ for the observed extrasolar planets as stars; results of the theoretical simulations are shown as open squares. The four panels correspond to different choices of the eccentricity damping time scale: $\tau_{\rm ed} = 0.1$ Myr (upper left), $\tau_{\rm ed} = 0.3$ Myr (upper right), $\tau_{\rm ed} = 1.0$ Myr (lower left), and $\tau_{\rm ed} \rightarrow \infty$ (lower right).

Finally, in Fig. 4.15, we present a set of $a - \epsilon$ diagrams with all of the corrections applied: a reflex velocity cut such that only planets with $k_{\rm re} > 3$ m/s remain, continued migration with remaining disk lifetimes given by the algorithm depicted in Fig. 4.11, and the circularization correction. The resulting theoretical distributions of a and ϵ are in reasonable agreement with those of the observed sample of extrasolar planets. The eccentricity damping time scale $\tau_{\rm ed} = 0.3$ Myr (i.e., $\tau_{\rm ed} = \tau_{\rm damp}$) provides the best fit, although all three cases with $\tau_{\rm ed}$ in the range 0.3 – 3 Myr are in the right ballpark.

4.15

4.4 Conclusion

In this section we summarize our results so far. As the outer planet migrates inward, it eventually becomes close enough to the interior planet to force it inward and to drive eccentricity growth with increasingly violent interactions. Such systems are generally not stable in the long term and adjust themselves to stability by ejecting a planet, accreting a planet onto the central star, or by having the two planets collide. The surviving planet is left on an eccentric orbit of varying semi-major axis, roughly consistent with the orbits of observed extrasolar planets. On longer time scales, tidal interactions with the central star act to circularize the orbits of the closet planets. We have presented a comprehensive, but not exhaustive, exploration of parameter space for this migration scenario. Our main results can be summarized as follows:

[1] This migration scenario results in a wide variety of final systems with a broad distribution of orbital elements. In particular, this migration scenario can fill essentially the entire $a - \epsilon$ plane for semi-major axes a smaller than the initial values. The observed extrasolar planets have orbital elements that fill the $a - \epsilon$ plane in roughly the same way (see Figs. 4.9 – 4.15). When the theoretical ensemble of planets is corrected for additional orbital evolution due to interactions with the circumstellar disk

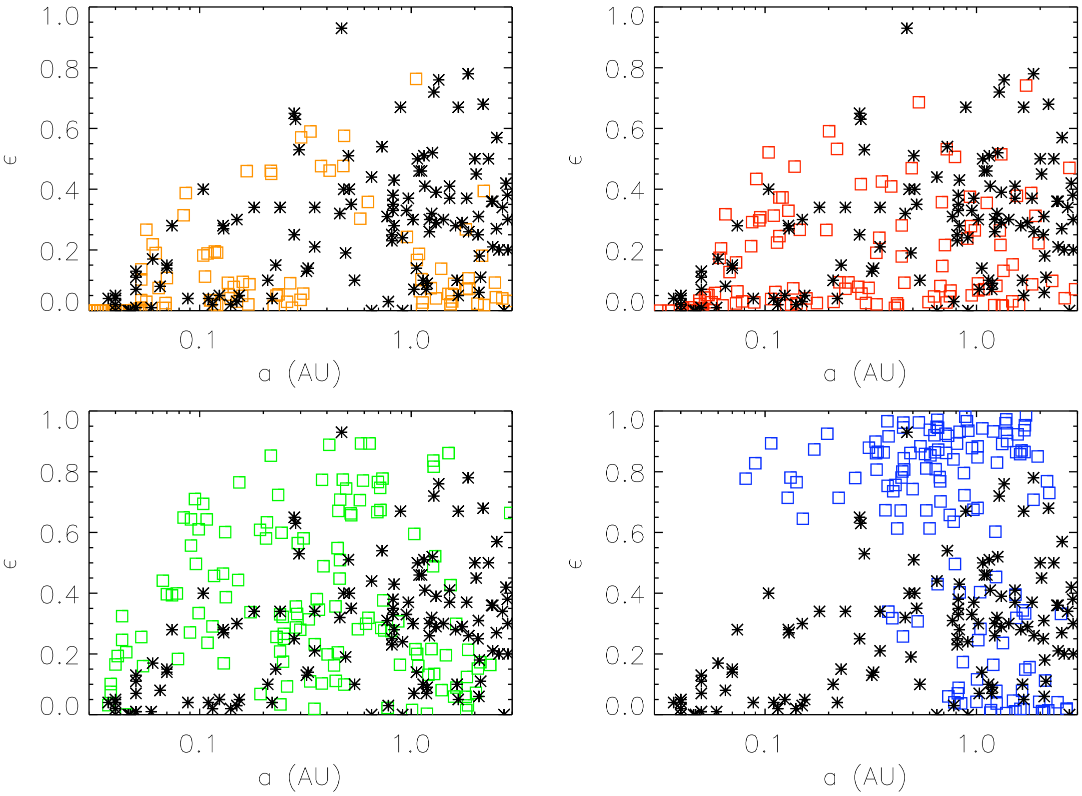

Figure 4.15. The $a-\epsilon$ plane for observed and theoretical planets using corrections for both continued disk evolution and tidal circularization. The theoretical sample starts with a log-random IMF, but a reflex velocity cut $k_{\rm re} > 3$ m/s has been applied to the surviving planets. The disk is assumed to continue driving planet migration beyond the end of the simulations for a random time interval in the range $0-0.3$ Myr. Tidal circularization is assumed to continue for a stellar lifetime, taken to be a random time interval in range $1-6$ Gyr. This diagram shows the semi-major axes a and eccentricities ϵ for the observed extrasolar planets as stars; results of the theoretical simulations are shown as open squares. The four panels correspond to different choices of the eccentricity damping time scale: $\tau_{\rm ed} = 0.1$ Myr (upper left), $\tau_{\rm ed} = 0.3$ Myr (upper right), $\tau_{\rm ed} = 1.0$ Myr (lower left), and $\tau_{\rm ed} \rightarrow \infty$ (lower right).

(on $\lesssim$ Myr time scales) and tidal interactions with the central star (on ~ 1 Gyr time scales), the resulting distributions of theoretical orbital elements are in reasonable agreement with those of the observed sample of extrasolar planets.

[2] Planets of smaller mass tend to be the ones that are ejected or accreted (see Figs. 4.3 and 4.4). The mass distribution of the observed planetary sample is roughly log-random, with a moderate deficit of planets at the low mass end (Fig. 4.7). This shape is consistent with planets being formed with (roughly) a log-random mass distribution and the lower end of the mass function being depleted through planet-planet scattering, as produced by this migration mechanism. Keep in mind, however, that the lower end of the mass distribution also suffers from selection effects (Tabachnik & Tremaine, 2002), which must be sorted out before definitive conclusions can be made (see Section 4.1).

[3] The mutual gravitational interactions of the planets are highly effective at increasing orbital eccentricities. The general trend is for planet-planet scattering to produce orbital eccentricities that are somewhat larger than those observed in the current sample of extrasolar planets. As a result, real solar systems must either provide sufficient eccentricity damping as suggested by numerical simulations of planet-disk interactions (e.g., Kley et al., 2004; Nelson et al., 2000), contain only single planets, or provide a mechanism to keep multiple planets sufficiently separated. The eccentricity damping time scale that provides the best fit to the observations lies in the range $\tau_{\rm ed} = 0.1 - 1$ Myr for a viscous damping time scale of $\tau_{\rm damp} = 0.3$ Myr, i.e., the ratio $\tau_{\rm ed}/\tau_{\rm damp} = 1/3 - 3$. While we find in the next chapter that, analytically, eccentricity excitation and damping are both possible, this study indicates that eccentricity damping is most effective at reproducing the characteristics of the observed extrasolar planets.

Planet-planet interactions are most effective at increasing eccentricities when the two planets are in a mean motion resonance, as can be seen from individual simulations. If additional physics, such as MHD turbulence, prevents the planets from remaining in resonance, this effect will likely be diminished (see Chapter 6.)

[4] The inclination angles of the planetary orbits are excited with a well-defined distribution centered of $\Delta i \approx 5$ degrees (Figs. 4.6 and 4.7). For the end states of this migration mechanism, the inclination angle excitation is correlated with the excitation of orbital eccentricity (Table 6).

[5] This migration scenario leads to a large number of ejected planets; specifically, about one-third to one-half of the simulated systems eject a planet. The distribution of ejection speeds is broad, with a peak near 5 km/s and a long tail toward higher speeds (Fig. 4.8). The functional form of the distribution of ejection speeds can be understood in terms of the simple physical argument given in Section 3.5. More than 90 percent of the exiled planets are predicted to attain ejection speeds greater than 1 km/s, the speed required for planets to (immediately) escape their birth aggregate. As a result, typical stellar birth clusters (with $N_* \approx 300$) are expected to contain only ~ 12 free floating planets at a given time due to this migration mechanism.

This migration scenario produces a full distribution of orbital elements for the surviving planets and is in reasonable agreement with observations. In order for this mechanism to be successful, the systems must have a number of properties, and it is useful to summarize them here: The planets that end up in the currently observed region of the $a - \epsilon$ plane are assumed to have formed in disk annulus $r = 3 - 7$ AU, roughly where Jupiter lives in our solar system. The disk must be able to sustain Type II migration torques over time scales ~ 1 Myr; the disk must maintain more mass (in gas) than its planets over this time scale, which is comparable to the time required for giant planets to form through the core accretion mechanism. Some system-to-system variation in this migration time scale is also indicated. As mentioned above, disk signatures are observed over longer times (several Myr), although the disks do not necessarily maintain enough mass to drive migration over this longer time. The torques must be large enough so that $|a/\dot{a}| \approx 0.3$ Myr, which is equivalent to having a viscosity parameter $\alpha \sim 10^{-3}$. The disk must damp orbital eccentricity of the outer planet with a damping time scale in the range $0.1 - 1$ Myr (so that $|\epsilon\dot{a}/\dot{\epsilon}a| \sim 1$). The planetary IMF must be nearly log-random, more specifically, close to the observed planetary mass function with a moderate excess of lower mass planets (they are the ones accreted or ejected). Finally, in order to not overpopulate the (low a, high ϵ) portion of parameter space, close orbits must be circularized and hence the tidal quality factor must lie in the estimated range $Q = 10^5 - 10^6$. If the system parameters differ significantly from these values/ranges, then this migration mechanism (in the form studied here) will not produce the observed orbital elements of extrasolar planets.

Although this migration mechanism is promising, a number of issues remain unresolved and should be considered in future work. One important issue is the manner in which eccentricity is damped by the circumstellar disk. The parametric treatment presented here indicates that in order for the theory to produce results consistent with the observed distributions of orbital elements, the ratio of the eccentricity damping time scale to the migration (disk accretion) time scale should lie in the range $\tau_{\rm ed}/\tau_{\rm damp} \approx 1/3 - 3$. Numerical simulations of circumstellar disks interacting with planets often provide a damping time scale near the low end of this range (e.g., Nelson et al., 2000; Kley et al., 2004), whereas competing analytic calculations suggest that eccentricity is not damped at all, but rather is excited by the disk (Goldreich & Sari, 2003; Ogilvie & Lubow, 2003). Since a particular disk cannot damp and excite eccentricity at the same time, these two conflicting results define an interesting problem for future study. The resolution of this issue must allow for eccentricity damping time scales in the proper range ($\tau_{\rm ed}/\tau_{\rm damp} \approx 1/3 - 3$) if this migration scenario represents the correct explanation for the observed extrasolar planetary orbits. Therefore, the next chapter of this chapter investigates the eccentricity evolution of giant planets with a range in starting eccentricity.

CHAPTER 5

ECCENTRICITY EVOLUTION OF GIANT PLANET ORBITS

In the standard description of planetary migration, rings of disk material in resonance with a planet in a nearly circular orbit exert torques on the planet, driving it inward and further decreasing its eccentricity ϵ (Goldreich & Tremaine, 1980, hereafter GT80). This scenario, while appropriate for our solar system, never allows the planet to possess large orbital eccentricity, and hence does not explain the large eccentricities of many detected planetary orbits. As a result, one of the current challenges in planetary migration theory is to produce the wide range in orbital eccentricity observed in the extrasolar planet population. The observed range in eccentricity can be explained by disk torques acting in conjunction with interactions with a second planet (Moorhead & Adams, 2005, see Chapter 4; hereafter MA05; see also Rasio & Ford, 1996; Thommes & Lissauer; 2003, Adams & Laughlin, 2003). Here we investigate whether eccentricity excitation can take place when we remove the small eccentricity assumption from the GT80 formalism. We then outline a method for incorporating the results into numerical simulations, such as that performed in Chapter 4, in order to investigate to what extent the a-ϵ distribution changes under this modification.

This chapter combines the formalism of three key analytic papers on planet migration: GT80, Goldreich & Sari (2003; hereafter GS03), and Ogilvie & Lubow (2003; hereafter OL03). Specifically, we obtain our torque formulas from GT80, the form of the eccentricity derivative from GS03, and our treatment of saturated corotation resonances from OL03. We extend this combined treatment primarily by performing a full calculation of the coefficients of the cosine expansion of the planet's perturbation to the overall gravitational potential, $\phi^{\mathsf{P}}_{\ell,m}(\beta)$ (see Chapter 3), assuming neither small eccentricity nor large azimuthal wavenumber (as in past studies). We find that the function $\phi^{\mathsf{P}}_{\ell,m}(\beta)$ has a complicated dependence on eccentricity (see section 2). Each resonant torque depends on $\phi^{\mathsf{P}}_{\ell,m}(\beta)$ (see Chapter 3), and as a result, the eccentricity time derivative is also a complicated function of eccentricity; in particular, $d\epsilon/dt$ attains both positive and negative values depending on the current value of eccentricity. Several properties of the planet's cleared gap, including its width, placement around the planet, and the degree to which it is cleared, alter the shape of $d\epsilon/dt$. In this chapter, we present eccentricity time derivatives for a variety of gap widths and shapes, seeking common behaviors. Additionally, if corotation resonances become saturated, we find $d\epsilon/dt$ to be almost exclusively positive. In this manner, we attain a greater understanding of how the production of either eccentricity excitation or damping depends on current planet and disk properties. The paper concludes with a discussion of this finding in the context of recent analytic studies as well as numerical studies, which generally produce eccentricity damping.

5.1 Methods and Initial Conditions

5.1.1 Disk Properties

For the sake of definiteness, we consider a $1M_{\mathsf{J}}$ planet orbiting a 1 $M_\odot$ star, embedded in a 0.05 $M_\odot$ circumstellar disk with radius 30 AU. We assume that the unperturbed disk surface profile density falls off with distance from the central star as a power law, $\Sigma = \Sigma_0(r/r_0)^{-1/2}$. We choose this power-law index for comparison with the many numerical studies that do the same; additionally, the results are largely insensitive to this choice. We can easily verify that the small chosen disk mass does not disturb the overall Keplerian rotation curve $\Omega(r)$, i.e., the condition

$$\frac{G\Sigma}{\Omega^2 r} \ll 1 \tag{5.1}$$

is satisfied; the largest value $G\Sigma/\Omega^2 r$ attains for any value of r in our given range is 0.04.

We assume that the radial temperature profile also obeys a power law, $T = T_0(r/r_0)^{-3/4}$, where $T_0 = 50$ K at the snow-line, $r_0 = 7$ AU. Finally, we specify the properties of the disk material, the standard viscosity parameter for accretion disks $\alpha = 10^{-3}$ and the ratio of specific heats $\gamma = 1.4$. These parameters determine the extent to which planets are able to clear gaps in the disk and the strength of the torques produced by disk-planet resonances (see GT80; Shu, 1992; Lin & Papaloizou, 1993). A change in the temperature profile or a change in viscosity would result in a different gap width; we investigate several gap widths to account for such possible variations in disk properties.

We assume a flat (cold) disk in our analysis. In addition, our torque formulas require that the disk satisfy the more stringent condition,

$$m\frac{h}{r} = m\frac{(a_s/\Omega)}{r} \ll 1\,, \tag{5.2}$$

for each resonance of order m, where h is the disk scale height and a_s is the sound speed. The largest value h/r attains is 0.07, where $h/r \simeq 0.04(r/1 \text{ AU})^{1/8}$. A 1 M_J planet at 1 AU allows for only 5-10 resonances of each type, and so we can safely use the flat disk torque formulas. Notice, however, that smaller planets produce smaller gaps, which in turn require larger values of m. As a result, this treatment cannot be extrapolated to arbitrarily small planet masses.

We adopt the treatment of disk torques as developed in GT80 and outlined in Chapter 3 of this thesis, including both Lindblad and corotation resonances. We calculate the location and torque of each resonance (and discuss the perturbing function's coefficients $\phi^{\mathsf{P}}_{\ell,m}(\beta)$ in detail). We then present our method for translating a given gap profile into an upper limit on the number of contributing resonances.

5.1.2 Calculating the Expansion Coefficients

Calculating the coefficients of the disturbing potential, $\phi^{\mathsf{P}}_{\ell,m}$, requires the evaluation of an oscillatory two-dimensional integral. One method of sidestepping this problem is to expand $\phi^{\mathsf{P}}_{\ell,m}(r)$ to first order in ϵ (GT80). However, extrasolar planets often display large orbital eccentricity, and one goal of migration theory is to explain these large eccentricities. It is therefore important to consider the validity of the linear approximation of $\phi^{\mathsf{P}}_{\ell,m}$ for the full range of eccentricity ϵ. Figure 5.1 displays the behavior of the numerically determined and approximate expressions for one particular coefficient, $\phi^{\mathsf{P}}_{4,3}(r_{\mathsf{ILR}})$, as a function of eccentricity. Clearly, an approximation to first order in eccentricity is only useful for eccentricities $\epsilon \lesssim 0.3$. In the context of GT80, this approximation was acceptable as researchers were mainly interested in explaining the properties of our own solar system, where planets have nearly circular orbits. However, many extrasolar planets possess large eccentricities, and thus the small ϵ approximation necessarily breaks down.

5.1

An alternative method for avoiding the full calculation of $\phi^{\mathsf{P}}_{\ell,m}$ is to take the large m limit, where the Lindblad and corotation resonances have the same functional dependence on $\phi^{\mathsf{P}}_{\ell,m}(r)$ (see Eqs. 3.6 and 3.4). In this limit, one can evaluate the degree to which Lindblad and corotation resonances cancel or add (GS03). The torque is proportional to m, so large m resonances are more significant. This approximation works well for less massive planets, which clear small gaps and allow large m resonances to contribute to the torque. On the other hand, a 10 M_J planet clears a wide enough gap that only a few resonances exist, and even a 1 M_J planet only allows for only 5 to 10 resonances of each type. Thus, an important part of this study is to

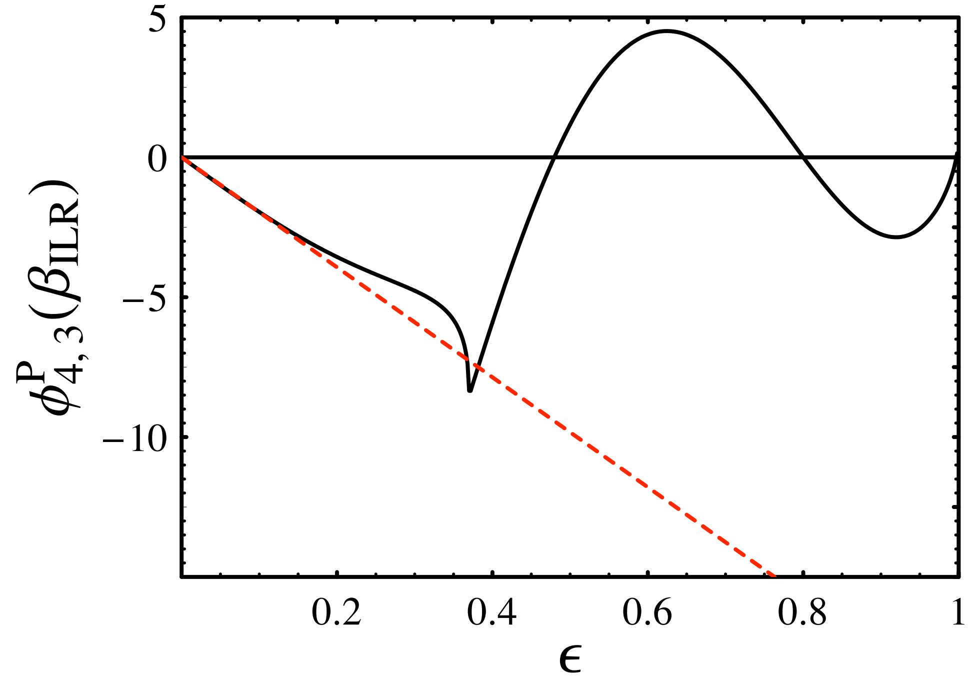

Figure 5.1. The exact solution for $\phi^{\mathsf{P}}_{4,3}(r_{\mathsf{ILR}})$ (solid curve) and an approximation for $\phi^{\mathsf{P}}_{4,3}(r_{\mathsf{ILR}})$ accurate to first order in eccentricity (dashed line) as a function of eccentricity. This plot shows that, for this ℓ, m, the linear approximation is useful only in the region $\epsilon \lesssim 0.3$. As the azimuthal wavenumber m increases, the cusp in the exact solution moves leftward while the oscillations in the right half of $\phi^{\mathsf{P}}_{\ell,m}(r_{\mathsf{ILR}})$ increase in number and decrease in amplitude, thus shrinking the region of accuracy for the linear approximation.

calculate the coefficients $\phi^{\mathsf{P}}_{\ell,m}(r)$ to much higher order accuracy for larger values of eccentricity, ϵ.

To conclude, for the currently observed sample of extrasolar planets, making low ϵ or large m approximations may not produce the correct eccentricity evolution for any given system; on the other hand, calculating the exact solution for $\phi^{\mathsf{P}}_{\ell,m}(r)$ is often not computationally feasible. Therefore, we embark on a semi-analytic investigation of the eccentricity evolution for intermediate values of eccentricity and for a number of representative disk-planet configurations. We look for an overall pattern, both to understand eccentricity evolution and to incorporate into future calculations of planetary migration.

5.1.3 The shape of the function $\phi^{\mathsf{P}}_{\ell,m}(\beta)$ and its radial derivative

Here we note several characteristics of $\phi^{\mathsf{P}}_{\ell,m}(\beta)$ and its derivative as a function of ϵ, as shown in Fig. 5.1. The overall shape consists of three distinct regions: a nearly linear decrease with ϵ for small ϵ, a cusp located at an intermediate value $\epsilon = \epsilon_0$, and a smooth oscillation for larger values of ϵ. As m increases, the location of the cusp moves to the left, and the number of oscillations increases roughly in proportion with m. The cusp at $\epsilon_0 = 1-\beta$ is of particular interest because the derivative $d\phi^{\mathsf{P}}_{\ell,m}(\beta)/d\beta$ becomes unbounded at $\epsilon = \epsilon_0$.

The function $\phi^{\mathsf{P}}_{\ell,m}(\beta)$ is bounded, and we find, as expected (GT80) that the overall amplitude of the resonance falls off as $|\ell - m|$ increases (GT80). However, the derivative $d\phi^{\mathsf{P}}_{\ell,m}(\beta)/dr$ is unbounded at the location of the cusp in $\phi^{\mathsf{P}}_{\ell,m}(\beta)$, ϵ_0. Furthermore, $\epsilon_0 = |1-\beta| = |1-(m-1)|/\ell$ (for inner Lindblad resonances, for example), and so is dense like the rational numbers. In other words,

$$\forall\ \epsilon,\ h \in \mathbb{R}, \{\phi^{\mathsf{P}}_{\ell,m} :\ |\partial_r \phi^{\mathsf{P}}_{\ell,m}(\epsilon)\Big|_{r^{\mathsf{P}}_{\ell,m}}| > h\} \neq \varnothing. \tag{5.3}$$

Using this information alone, it is incorrect to ignore higher values of $|l - m|$. However, any physical disk will exhibit a smooth response to the planet's stimulus.

To mimic this effect, we manually smooth the potential (and therefore the cusp in $\phi^{\mathsf{P}}_{\ell,m}$) over the largest relevant physical scale. The viscous length scale is given by

$$\delta_\nu = \left(\frac{\nu}{m[-d\Omega/dr]} \right)^{1/3} , \tag{5.4}$$

where ν is the characteristic kinematic viscosity (OL03). For $m = 1$ and $r = 1$ AU, $\delta_\nu = 0.004$, and for any m, r of interest, $\delta_\nu \lesssim 0.01$. On the other hand, the size of the disk scale height is $h/r \simeq 0.04$. We will present results using first the viscous length scale as our chosen smoothing length, and then using the disk scale height. This is to demonstrate the effect that increasing the smoothing length has on our results. Smoothing over these physical scales prevents the derivative from attaining arbitrarily large values, and higher order resonances may be safely discarded.

Furthermore, we may apply a low order correction for our treatment of the disk as two dimensional by averaging over the disk scale height (Menou & Goodman, 2004). The disk scale height is about four times as large as the viscous scale length, and therefore we will discard the viscous scale length and smooth all of our functions over the disk scale height.

It is important to note that the amplitude of the resonances decreases much more rapidly for small ϵ than for large ϵ. Thus, it is important to include resonances for which $|\ell - m| > 1$ in order to calculate $d\epsilon/dt$ accurately. However, the shape of $\phi^{\mathsf{P}}_{\ell,m}(\beta)$ does not change rapidly with $|\ell - m|$ (see Fig. 5.2), and higher order resonances tend to add to a similar shape as do lower order resonances. Therefore, we take the approach of using $|\ell - m| \leq 1$ resonances to determine the shape of $d\epsilon/dt$, and then calculating $d\epsilon/dt$ more accurately for key values of ϵ using all contributing ℓ, m.

5.2

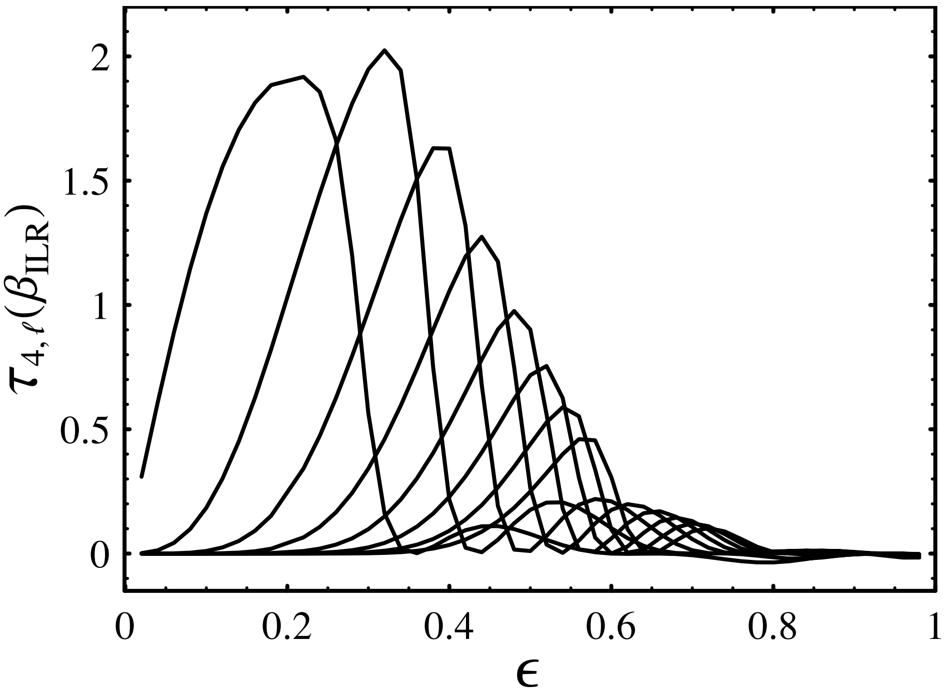

Figure 5.2. The exact solution for the torque exerted by the inner Lindblad resonance $\tau_{\ell,4}(r_{\sf ILR})$ as a function of ϵ for $\ell = 5, 6, 7, 8, 9, 10, 11, 12$. As ℓ increases, the first peak decreases and moves toward higher eccentricity. We find that by including resonances for which $|\ell - m| > 1$, $d\epsilon/dt$ increases in magnitude, but does not significantly alter the shape of $d\epsilon/dt$ as a function of ϵ.

5.2 Results

Using the framework developed in the above section, we can calculate the eccentricity time derivative for a given Jovian planet in a given thin disk. The most important parameters in this calculation are the mass, semi-major axis, and eccentricity of the planet, and the surface density profile in the vicinity of the planet's cleared gap. Our algorithm can be summarized as follows: [1] We define the radial surface density profile of the disk and the orbital properties of the planet. [2] We evaluate the formulae for $\phi^{\sf P}_{\ell,m}$ and its derivative (using the Gauss-Kronrod numerical integration function in *Mathematica*), the torques, and the eccentricity derivative resulting from each resonance, smoothing over the disk scale height to partially account for the disk's finite thickness (Menou & Goodman, 2004). [3] We sum the contributions to the total eccentricity derivative over all resonance types and values of m. For each set of input parameters (disk properties plus orbital parameters of the planet), we obtain $d\epsilon/dt$

as a function of ϵ. Issue may be taken with any individual surface density profile we present in this section. However, we present $d\epsilon/dt$ for a variety of gap architectures, noting shared characteristics.

5.2.1 A Sharp-Edged Gap

We first present the simplest case: a 1 M_J planet orbiting at $a = 1$ AU in a gap with sharply defined edges. The strongest resonances occur for values of $\ell = m$ or $\ell = m \pm 1$, limiting the number of values of ℓ we must consider (GT80). The azimuthal wavenumber m may still take on any value, but, as m increases, the location of the resonance approaches the semi-major axis of the perturbing planet. When the planet clears a clean gap, the edges of the gap place a physical upper limit on the number of values of m that must be considered. The resulting function $d\epsilon/dt$ versus ϵ (shown in Figs. 5.3 and 5.4) is the result of summing the contributions of five to ten resonances of each type (where type refers to, for example, an $\ell = m+1$ inner Lindblad resonance).

5.3

5.4

In Fig. 5.3, $d\epsilon/dt$ is not smoothed over the disk scale height, but is instead smoothed over the viscous length scale $\delta_\nu \simeq 0.01$. Due to the small smoothing length, the features of the $\phi^{\mathsf{P}}_{\ell,m}$ functions are clearly visible in Fig. 5.3; the peaks correspond to the singularities in $d\phi^{\mathsf{P}}_{\ell,m}(\beta)/d\beta$ smoothed over the viscous length scale, and the smooth right half of the plot is produced by the combination of the smoothly oscillating portions of the $\phi^{\mathsf{P}}_{\ell,m}(\beta)$ and $d\phi^{\mathsf{P}}_{\ell,m}(\beta)/d\beta$ functions. In Fig. 5.4, the features of the $\phi^{\mathsf{P}}_{\ell,m}$ functions are smoothed out over the disk scale height, $h/r \simeq 0.04$, and thus not clearly visible in the resulting function $d\epsilon/dt$. However, the peaks and troughs in $d\epsilon/dt$ for $\epsilon < 0.5$ generally correspond to the singularities in $d\phi^{\mathsf{P}}_{\ell,m}(\beta)/d\beta$, and peaks and troughs in $d\epsilon/dt$ for $\epsilon > 0.5$ correspond to the smoothly oscillating portions of the $\phi^{\mathsf{P}}_{\ell,m}(\beta)$ and $d\phi^{\mathsf{P}}_{\ell,m}(\beta)/d\beta$ functions. The most important result obtained from this

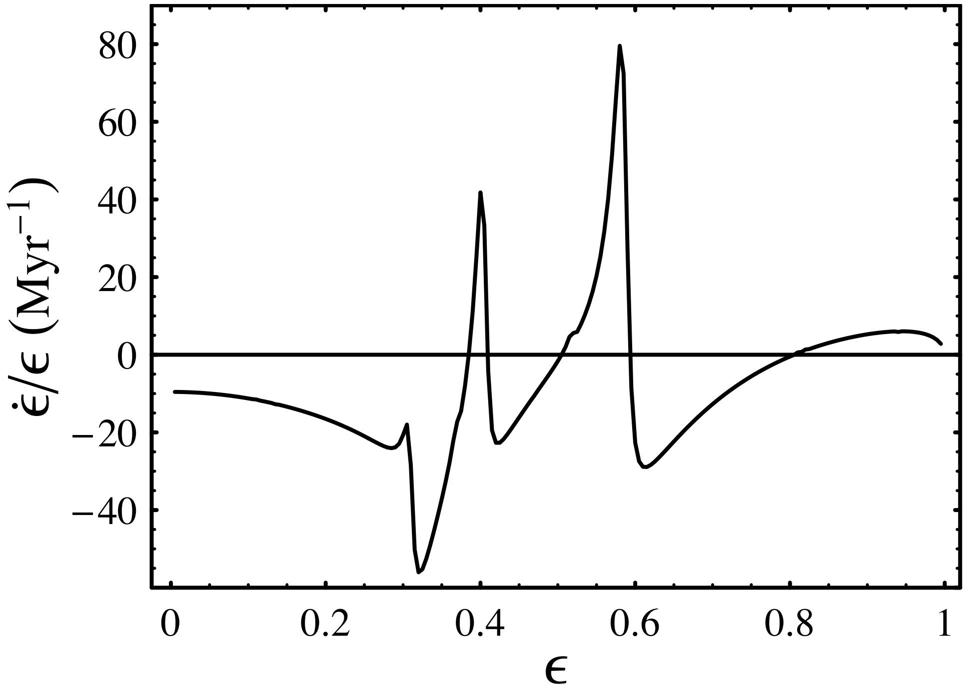

Figure 5.3. The function $d\epsilon/dt$ versus ϵ for a 1 M_J planet in a 1 AU orbit. Here we have smoothed over the viscous scale length to demonstrate the shape of $d\epsilon/dt$ for a small smoothing length. The features of this function clearly result from the $\phi^{\mathsf{P}}_{\ell,m}$ functions; each sharp peak and trough occurs at the location of a cusp in some $\phi^{\mathsf{P}}_{\ell,m}$ function, which is the same location at which the radial derivative of $\phi^{\mathsf{P}}_{\ell,m}$ becomes unbounded (e.g., see Fig. 5.1).

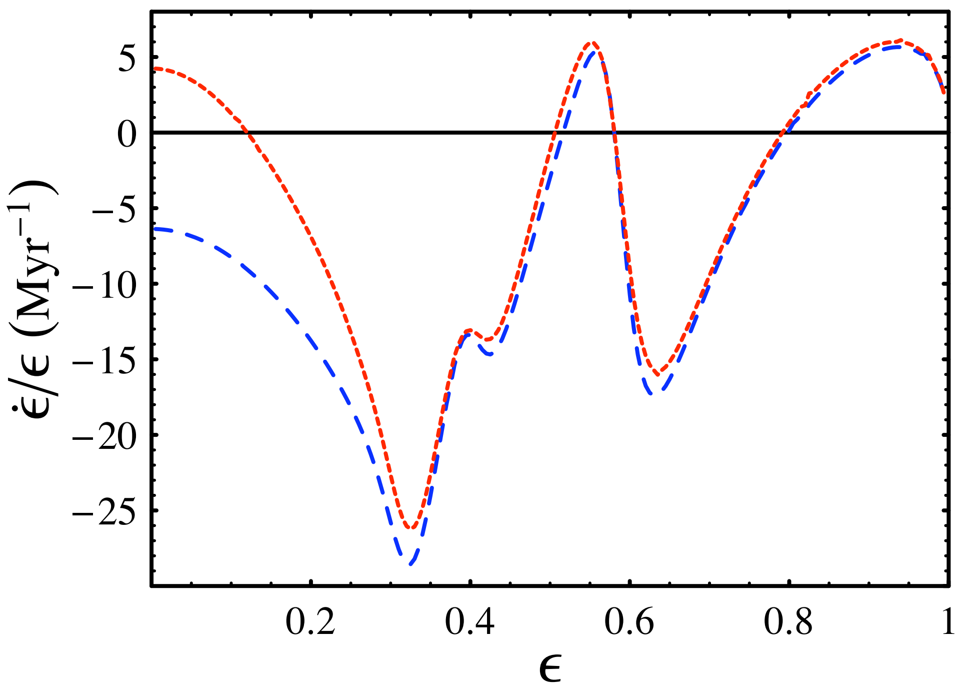

Figure 5.4. The function $d\epsilon/dt$ versus ϵ for a 1 M_J planet in a 1 AU orbit. Here we have smoothed over the disk scale height to account for the finite thickness of the disk. The overall shape of this function is common for all surface density profiles that have gaps with sharp edges centered on the orbiting planet. The features of this function result from the $\phi^{\mathsf{P}}_{\ell,m}$ functions; peaks and troughs for $\epsilon < 0.5$ occur at the locations of smoothed cusps in the $\phi^{\mathsf{P}}_{\ell,m}$ functions, and result from the oscillations in low order $\phi^{\mathsf{P}}_{\ell,m}$ functions for $\epsilon > 0.5$. The dotted curve is for a narrower gap.

plot is that planet-disk interactions do not result in uniform eccentricity damping or excitation. The behavior of $d\epsilon/dt$ is complicated, leading to varying levels of damping or excitation depending on the current value of ϵ.

There exist sizable bodies of both analytic and numerical work on the subject of planet-induced gaps in circumstellar disks. In the context of this study, these works translate into a wide array of possible inputs for the surface density in the vicinity of the planet. A planet on an eccentric orbit is likely to have a wider gap than a planet in a circular orbit, as is assumed in many of these studies, and so we also perform a calculation of $d\epsilon/dt$ for an artificially widened gap. The shape of the surface density profile has two important effects on the resulting eccentricity evolution equation $d\epsilon/dt$: [1] Since each torque depends on either the surface density or its radial derivative, altering the shape of the surface density profile will (linearly) change the relative heights of the features in the function $d\epsilon/dt$. At the same time, if the width of the gap is unchanged, the overall pattern will also be largely unchanged. [2] If we instead alter the gap width, the shape of the function $d\epsilon/dt$ changes as resonances are included or excluded. To understand the general implications of gap width for eccentricity evolution, we present gap architectures with varying gap widths.

The result of slightly narrowing the cleared gap – a change in the sign of $d\epsilon/dt$ – is also displayed in Fig. 5.4. However, we are most interested in calculating $d\epsilon/dt$ for intermediate values of eccentricity (and this is the region where our assumptions are most accurate), so this change is not significant within the context of our calculations.

5.2.2 The Effect of Residue in the Gap

When some material remains within the gap, the radius at which disk material no longer exerts torques on the planet is unclear. To investigate eccentricity evolution in such a gap, we choose a gap shape resembling that produced by the numerical calculations of Bate et al. (2003), where residual material remains within the gap (see Fig. 5.5). We then raise the limit on the number of contributing resonances (by raising the allowed values of m) until $d\epsilon/dt$ converges to a single value.

5.5

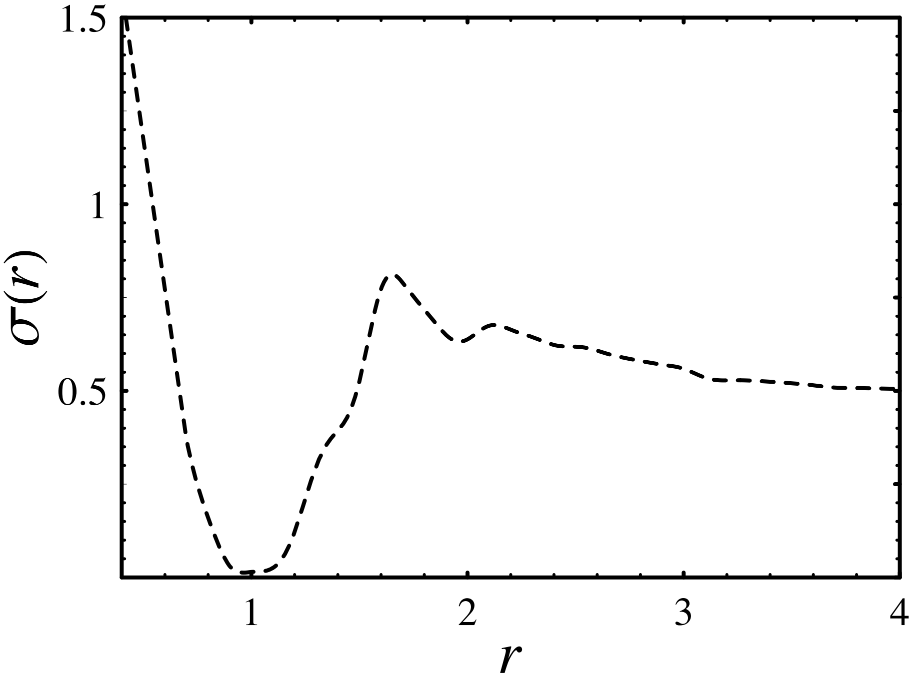

Figure 5.5. Surface density profile for a gap as calculated in Bate et al. (2003). This profile is used to evaluate $d\epsilon/dt$ versus ϵ in Fig. 5.6.

5.6

As mentioned, the radius at which disk material no longer exerts torques on the planet is unclear. Therefore, we present $d\epsilon/dt$ with and without torques resulting from coorbital disk material. Figure 5.6 displays $(d\epsilon/dt)/\epsilon$ as a function of ϵ where only non-coorbital resonances are allowed to contribute. As it is somewhat unclear how to include coorbital material, we present results both with, and withouth, coorbital resonances. Here, we find that $(d\epsilon/dt)/\epsilon$ does not converge as ϵ approaches zero, but instead approaches $+\infty$. When we include the effects of coorbital resonances (Fig. 5.7), $d\epsilon/dt$ switches sign for small ϵ, resulting in eccentricity damping rather than excitation. Notice, however, that in both cases, eccentricity damping results for all values of eccentricity in the range $0.1 < \epsilon < 0.8$.

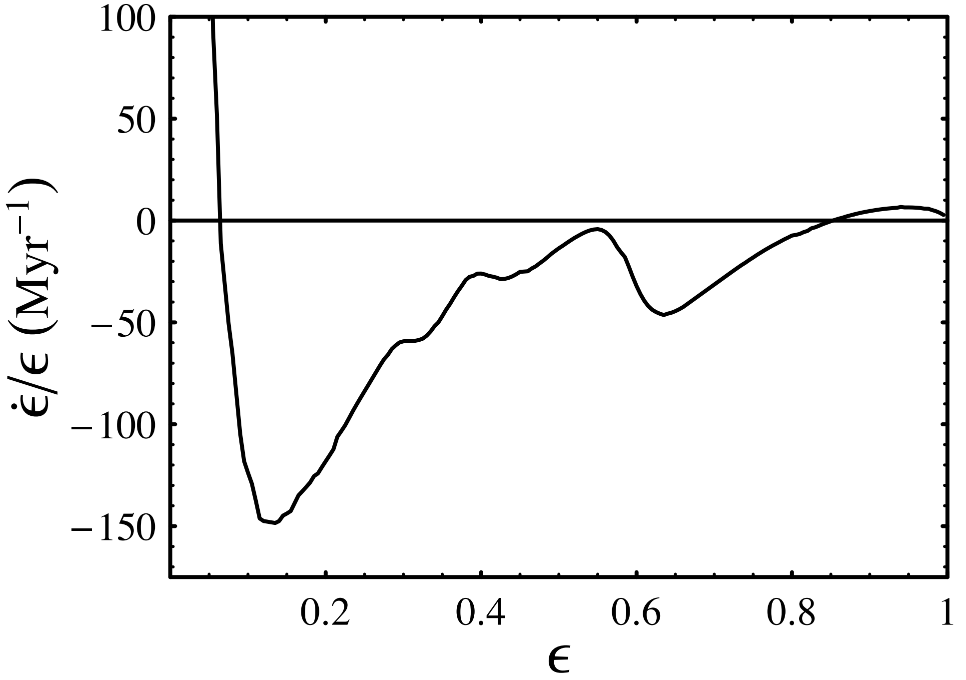

Figure 5.6. The function $d\epsilon/dt$ versus ϵ for a 1 M_J planet in a 1 AU orbit for the gap shape of Fig. 5.5 (from Bate et al., 2003). Here we have included non-coorbital corotation and Lindblad resonances only.

5.7

5.2.3 Other configurations

As mentioned previously, the overall shape of the function $d\epsilon/dt$ versus ϵ is fairly uniform for all surface density profiles that contain a sharp-edged gap of a given width centered on the planet. However, there are a number of scenarios in which a planet may lie off-center in the gap: accretion may clear the inner disk, photoevaporation or a close encounter with another star may strip the outer disk, or multiple planets may produce overlapping gaps in the disk. Of these three possibilities, the situation in which two planets have overlapping gaps is of the greatest interest because two planets orbiting in a close resonance are certain to produce a gap in which neither planet lies at the center. In contrast, it requires more fine-tuning for other processes to deplete the disk from one of its edges exactly to the semi-major axis of the planet.

To study the effect of a two-planet gap, we place two 1 M_J planets in orbits at

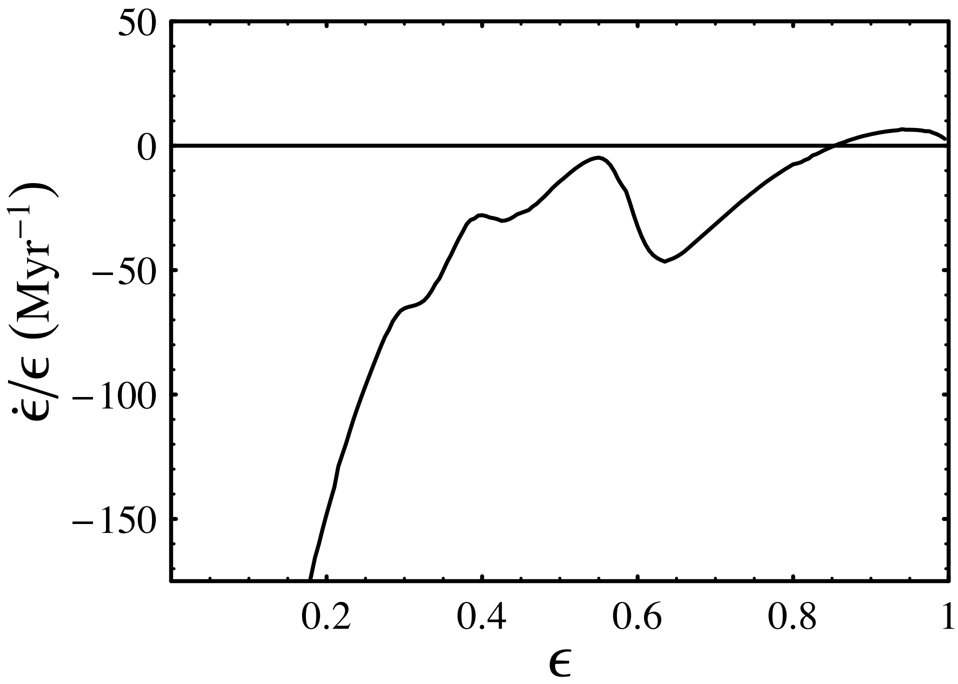

Figure 5.7. The function $d\epsilon/dt$ versus ϵ for a 1 M_J planet in a 1 AU orbit for the gap shape of Fig. 5.5 (from Bate et al., 2003). Here we have included coorbital corotation and Lindblad resonances as well as non-coorbital resonances.

a_1 =1 AU and a_2 =1.59 AU, and thus in a 2-1 mean motion resonance. The resulting gap in disk material is displayed in Fig. 5.8, and the eccentricity evolution it produces is displayed in Fig. 5.9. We find that the gap asymmetry does not affect the planets equally; while the inner planet experiences a drastic change in both the shape and magnitude of its $d\epsilon/dt$ function, the outer planet's eccentricity evolves in much the same way a lone planet's eccentricity evolves. We find, upon closer inspection, that this result is due to the fact that the contribution to $d\epsilon/dt$ from the $m = 2$, $\ell = 1$ corotation and Lindblad resonances are significantly greater than any other resonance contributions for a single planet, and that these resonances are located on the outer side of the gap. For the inner planet in a 2-1 resonance, there is no material at this location, but for the outer planet, the location of the 2-1 resonance lies within the disk material. We can deduce from this that, for any planet orbiting in a disk, a particularly strong resonance exists between the planet and a ring of disk material inside the planet's orbit. It is then important to combine this effect with that of the mean motion resonance (Murray & Dermott, 2001; Thommes & Lissauer, 2003; Lee & Peale, 2002) between the two planets when performing semi-analytic studies of solar system evolution such as that in MA05.

5.8

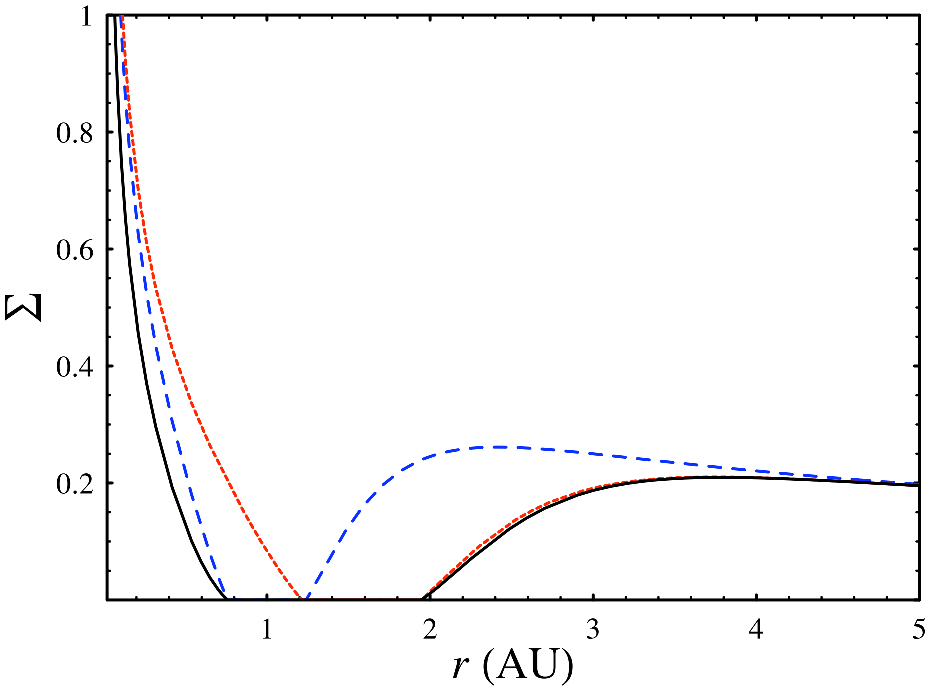

Figure 5.8. Radial surface density profile for a disk in the presence of 1 M_J planets at (dashed) 1 AU, (dotted) 1.59 AU, and at both 1 AU and 1.59 AU (solid). This configuration places the planets in a 2-1 mean motion resonance. The gaps produced by the two planets in the final case overlap to produce a single wide gap, in which each planet is offset from the gap center.

5.9

If these results are to be used in future numerical calculations such as extensions to MA05 it is important to understand how the eccentricity evolution depends on orbital parameters. By completing a large range of calculations, we have determined the following: [1] As the semi-major axis a decreases, the surface density in the vicinity of the planet increases, and the planet sits in a deeper, narrower trough. The function $d\epsilon/dt$ versus ϵ obtains an increased number of peaks and troughs, smoothed over the disk scale height, in the small ϵ region as we include more resonances, and an

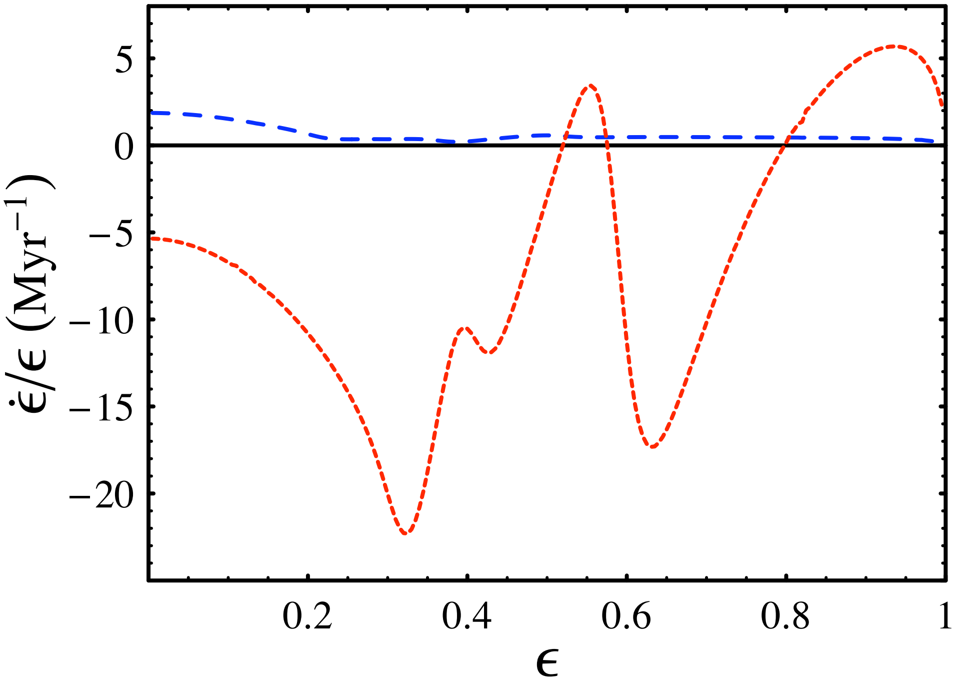

Figure 5.9. The resulting plot of $d\epsilon/dt$ as a function of ϵ produced by the double gap shown in Fig. 5.8. The dotted line traces the eccentricity evolution of the outer planet, and the dashed line traces that of the inner planet. The function $d\epsilon/dt$is changed substantially for the inner planet due to the lack of material at locations corresponding to the strongly contributing $m = 2, \ell = 1$ Lindblad and corotation resonances.

increased magnitude of $d\epsilon/dt$ everywhere due to the larger surface density at small radii. As a increases rather than decreases, these effects are reversed. [2] As the planet mass decreases, the planet clears a narrower and narrower gap. Once again, the function $d\epsilon/dt$ versus ϵ obtains an increased number of peaks and troughs, again smoothed over the disk scale height, and experiences an decreased overall magnitude due to the dependence $d\epsilon/dt \propto M_P$. (This dependence arises from Eqs. 3 and 11; In Eq. 3, the formula $d\epsilon/dt$ explicitly contains the term $1/M_P$, and we see from Eq. 11 that $(\phi^{\mathsf{P}}_{\ell,m})^2$ contributes M_P^2.)

5.2.4 Saturation of Corotation Resonances

The torque of the planet on resonances in the disk deposits or removes angular momentum from the resonance locations in the disk. Lindblad resonances lose this change in angular momentum through a wave flux, but corotation resonances do not. As a result, they can become saturated and thereby exert a reduced torque on the planet. In this section, we assume that coorbital corotation resonances will be completely saturated, and thus provide no contribution to the overall eccentricity evolution (Balmforth & Korycansky, 2001). We account for the effects of corotation saturation using the prescription of OL03.

The degree of saturation for a particular $(\ell,\, m)$ non-coorbital corotation resonance can be expressed in terms of a single parameter p (OL03), which is given by

$$p \equiv \left(\frac{-d\ln r}{d\ln\Omega}\right)\frac{\phi^{\mathsf{P}}_{\ell,m}(\beta)}{\kappa^2}\left(\frac{[-d\Omega/dr]}{\nu/m}\right), \tag{5.5}$$

where the viscosity ν is related to the parameter α by the standard Shakura-Sunyaev formulation, $\nu = \alpha\Omega h^2$. Therefore, assuming the disk is Keplerian, and that the disk scale height $h = a_s/\Omega$, the expression for p becomes

$$p = \frac{2}{3}\phi^{\mathsf{P}}_{\ell,m}(\beta)\left[\frac{3m_H}{\alpha\gamma k_B T_0}\sqrt{\frac{r}{GM_*}}(r/r_0)^{3/4}\right]^{2/3}. \tag{5.6}$$

Using the quantities specified previously, we obtain $p \approx 0.284\ \phi^{\mathsf{P}}_{\ell,m}(\beta)$. Our sample calculation of $\phi^{\mathsf{P}}_{4,3}(r_{\mathsf{ILR}})$ has an amplitude of about 5 ($\phi^{\mathsf{P}}_{4,3}(r_{\mathsf{C}})$ has a similar amplitude), and so the saturation parameter p attains values of order unity for some values of ϵ. Thus, it is important to investigate the effect that saturation may have on our results.

The torque exerted in the corotation region is reduced by a factor $f(p)$, where $f(p) \approx 0.4019p^{-3/2}$ for $p \gg 1$, and $f(p) \approx 1 - 2.044p^2$ for $p \ll 1$ (OL03). We interpolate between these two limits in a manner similar to that in GS03 to obtain

$$f(p) = (1 + 0.3529p^3)^{5/6}/(1 + 1.022p^2)^2 \, . \tag{5.7}$$

The result of including saturation effects is shown in Figs. 5.10 and 5.11. Thus, the calculated saturation level of corotation resonances results in eccentricity excitation over the full range of eccentricity. If coorbital resonances are allowed to contribute, a small interval of eccentricity damping exists for $\epsilon \lesssim 0.05$. On a side note, we learn that the substantial eccentricity damping in the low ϵ limit in Fig. 5.11 is due to coorbital Lindblad resonances and not coorbital corotation resonances.

5.10

5.11

Taken at face value, our results imply that all single planets starting with $\epsilon > 0.1$ will be ejected from their systems or accreted on time scales shorter than 0.15 Myr. Furthermore, uniform eccentricity excitation would lead to no multiple planet systems (MA05), in contrast with the observed population of extrasolar planets which contains about 10-20% multiple systems. As a result, it is unlikely that corotation resonances are saturated to the degree described above. The determination of the degree of saturation is thus an important issue for the future.

5.2.5 Eccentricity Damping at $\epsilon = 0.3$

As mentioned earlier in this work, our goal is to compute the eccentricity time derivative for a variety of orbital parameters and gap shapes, looking for a common pattern. We find that for each set of inputs, the eccentricity time derivative for a single planet

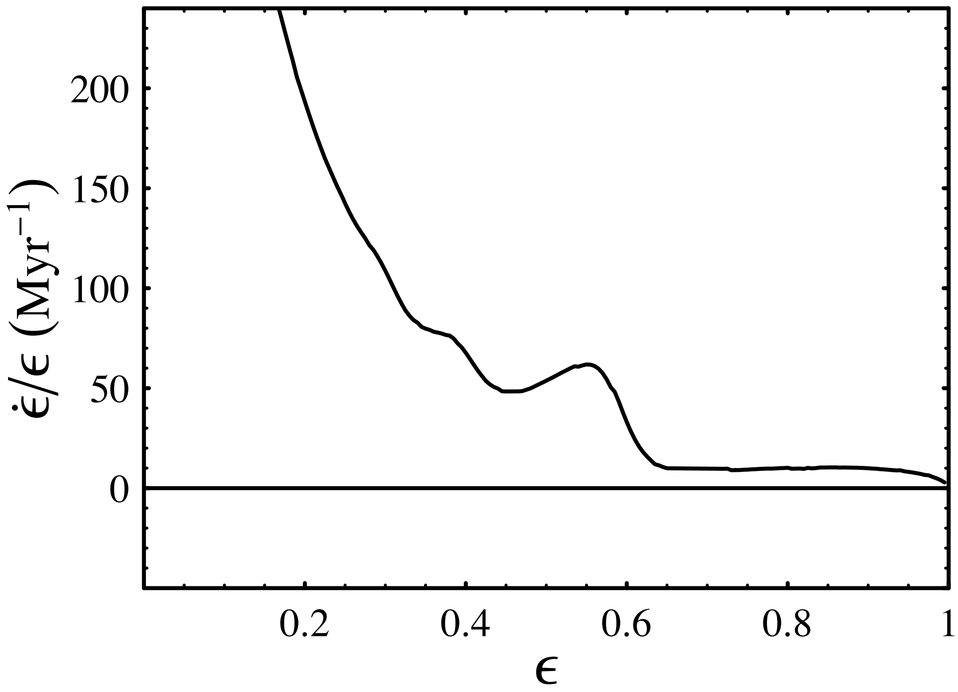

Figure 5.10. The function $d\epsilon/dt$ versus ϵ for a 1 M_J planet in a 1 AU orbit for the gap shape of Fig. 5.5 (from Bate et al. 2003), including the effects of saturation of corotation resonances. Here we have included only non-coorbital corotation and Lindblad resonances. A marked difference exists between this graph and previous graphs. This is due to the reduction of non-coorbital corotation resonant torques via corotation saturation.

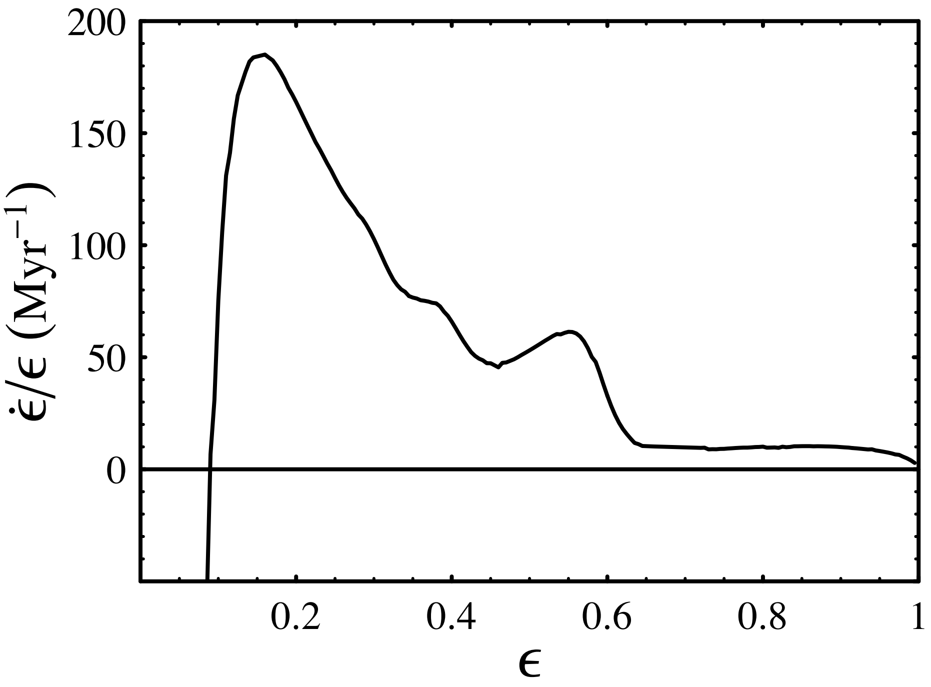

Figure 5.11. The function $d\epsilon/dt$ versus ϵ for a 1 M_J planet in a 1 AU orbit for the gap shape of Fig. 5.5 (from Bate et al. 2003), including the effects of saturation of corotation resonances. Here we have included coorbital corotation and Lindblad resonances as well as non-coorbital resonances, although we then assume that coorbital corotation resonances are fully saturated.

without saturation of corotation resonances is negative for some range in eccentricity between 0.1 and 0.5, and is always negative for $\epsilon = 0.3$. On the other hand, the eccentricity derivative for the same set of parameters, including $\epsilon = 0.3$, is always large and positive when corotation resonances become saturated.

At this point in our study, we narrow our focus to $\epsilon = 0.3$ only. We now include resonances in our calculation for which $|\ell - m| > 1$ and recalculate $d\epsilon/dt$ for our different gap shapes. The result is displayed in Table 5.1. The corresponding gaps in surface density are displayed in Fig. 5.12. We see that $d\epsilon/dt$ maintains its sign while adopting a greater magnitude in all cases, as expected.

5.12

5.1

It is clear that, using our approach and assumptions, we obtain, for intermediate eccentricity, either eccentricity damping or extremely rapid eccentricity excitation.

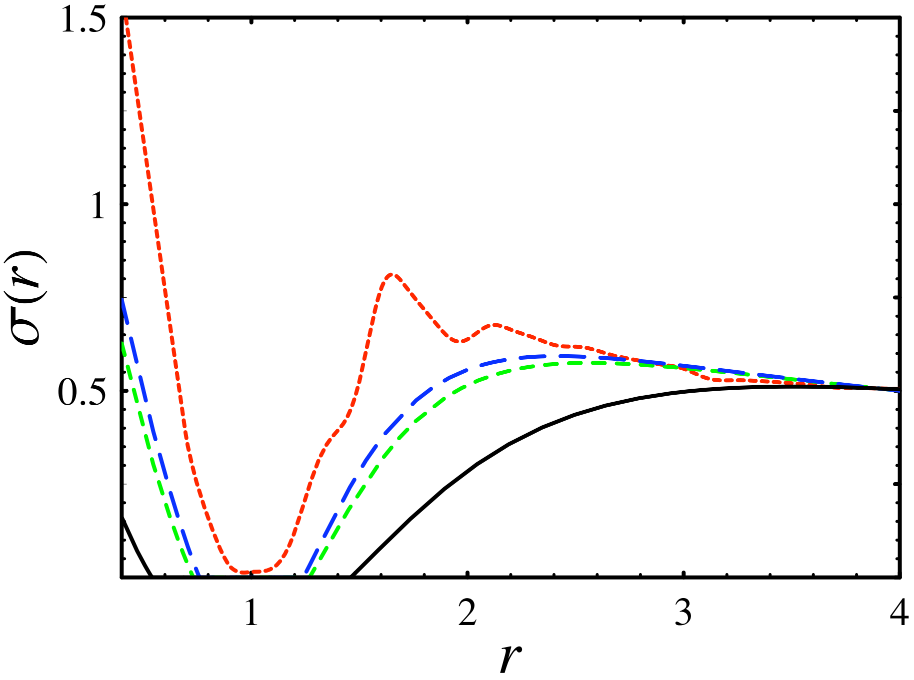

Figure 5.12. Surface density as a function of radius for different gap shapes corresponding to values of eccentricity evolution timescales presented in Table 5.1.

Eccentricity damping at $\epsilon = 0.3$ will prevent planets from attaining the full range of eccentricity values that the observed sample of extrasolar planets possesses. On the other hand, if corotation saturation occurs according to the formula of Ogilvie and Lubow (2003), planets would attain very large eccentricities in a few thousand years, and thus would likely be ejected from their host systems within the Myr lifetime of the disk. Either some additional component (such as vorticity of the gap edges) must be included in calculations of eccentricity evolution, or some additional physical phenomenon, such as interactions between planets in multiple planet systems, must take place.

5.3 Conclusions

We have re-examined the manner in which circumstellar disks exert torques on giant planets and thereby change their orbital eccentricity, and shown that both the small ϵ and large m approximations for calculating eccentricity evolution are invalid for

Table 5.1. $d\epsilon/dt$ at $\epsilon = 0.3$, in units of Myr^{-1}.

Gap Architecture	Coorbital Material Included?	Corotation Saturation Included?	$\lvert\ell - m\rvert \leq 1$ only	all ℓ, m
wide and sharp-edged	–	no	-0.16	-0.05
narrow and sharp-edged	–	no	-0.17	-0.048
narrowest and sharp-edged	–	no	-0.13	-0.073
Bate et al. gap	no	no	-0.052	-0.025
Bate et al. gap	yes	no	-0.050	-0.019
narrow and sharp-edged	–	yes	0.063	0.029
narrowest and sharp-edged	–	yes	0.077	0.031
Bate et al. gap	no	yes	0.032	0.017
Bate et al. gap	yes	yes	0.032	0.017

studying the current population of observed extrasolar planets. We have removed both of these approximations from the formalism and completed a full calculation of $\phi^{\mathsf{P}}_{\ell,m}(\beta)$ (see Fig. 5.1). The resulting function $d\epsilon/dt$ attains both positive and negative values (see Figs. 5.3 and 5.4), reflecting its nature as a composition of $\phi^{\mathsf{P}}_{\ell,m}(\beta)$ functions. Thus, Type II migration produces neither uniform eccentricity excitation nor uniform eccentricity damping, but can produce either excitation or damping depending on the combination of disk and planet properties. We have found that $d\epsilon/dt$ is influenced by gap properties, in particular gap width. As the gap width changes, the number of included torques changes and we see corresponding addition or subtraction of spikes in the $d\epsilon/dt$ function. The placement of the planet within the gap is also important. A planet in a 2-1 resonance with a second planet and thus far offset from the gap center, for instance, may experience substantially different eccentricity evolution than a planet roughly at the center of the gap.

A gap with sharp edges places an upper limit on the number of contributing resonances. The exact width of such a gap strongly affects the eccentricity time derivative in the low eccentricity limit. For instance, a small change in the gap width produces eccentricity excitation rather than damping for small eccentricity (Fig. 5.4). Therefore, it is important to understand the shape of the planet's cleared gap to predict the eccentricity evolution in the small eccentricity regime using our approach. If the gap contains residual contributing material (Figs. 5.6 and 5.7) or if the gap is generated by two, rather than one, planets (Fig. 5.9), the shape of $d\epsilon/dt$ versus ϵ changes drastically.

This work has several limitations. First, we have assumed throughout that the disk is infinitesimally thin. The accuracy of our method relies on the inclusion of relatively few disk torques. As m increases, the flat-disk approximation for disk torques is less accurate. This effect is of concern in our analyses when $\epsilon \lesssim 0.1$. Second, our calculations converge extremely slowly for large eccentricity. Furthermore, while D'Angelo et al (2006) showed that the primary effect of moderate planet eccentricity was to widen the gap in the disk, the effects of a very eccentric planet ($\epsilon > 0.5$) on disk geometry are uncertain. With these limitations in mind, we present again our $d\epsilon/dt$ plots with data shown only for $0.1 < \epsilon < 0.5$ (Fig. 5.13). This plot demonstrates that, as long as corotation resonances are unsaturated, eccentricity damping necessarily occurs for $0.2 < \epsilon < 0.5$. Therefore, disk-planet interactions alone cannot produce the full observed range in extrasolar planet eccentricities, assuming corotation resonances are unsaturated. However, disk-planet interactions combined with planet-planet scattering, as in Chapter 4, or turbulence, as in Chapter 6, remain possible solutions to the observed eccentricity distribution.

5.13

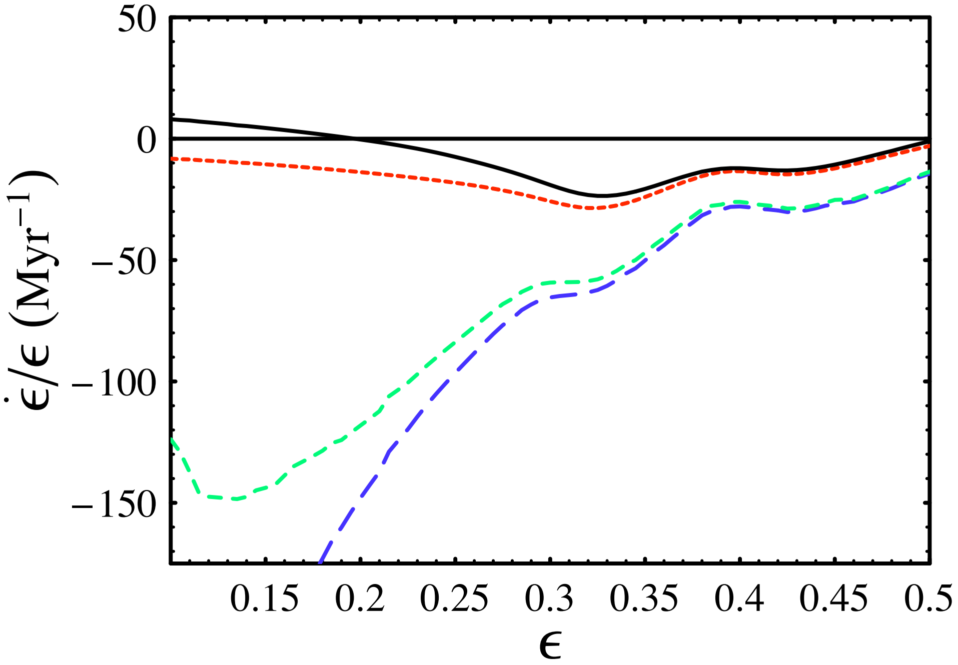

Figure 5.13. The function $d\epsilon/dt$ versus ϵ for a 1 M_J planet in a 1 AU orbit for various disk configurations. Note that the range in eccentricity (horizontal axis) is restricted to the regime where the approximations of this chapter are most applicable. The solid curve corresponds to a gap in the disk with sharp edges defined by $T_0 = 70$ K at $r_0 = 7$ AU, and the dotted curve corresponds to a gap in the disk with sharp edges defined by $T_0 = 50$ K at $r_0 = 7$ AU. The dashed curve corresponds to the gap shape of Fig. 5.5 (from Bate et al. 2003) with no coorbital resonances contributing, and the long-dashed curve to the same disk shape with coorbital resonances contributing. In all four curves, corotation resonances are completely unsaturated.

If, on the other hand, we find that if corotation resonances are saturated, we obtain almost exclusive eccentricity excitation (Figs. 5.10 and 5.11). However, the resulting excitation is so severe that a planet could only remain in orbit about its host star for less than a tenth of a million years (we obtain this timescale when we include all values of ℓ, m in our $d\epsilon/dt$ calculation). Assuming that disks last for of order one million years, this scenario fails to explain how planets survive disk-planet interactions.

There are several possible refinements and extensions of this work. In our treatment of the disk as strictly Keplerian, we neglect the effects of vortices near the gap edges. A careful treatment of vorticity may alter the strength of the corotation resonances and lead different values of the eccentricity derivative. Furthermore, it may be informative to extend the range in eccentricity for which this approach is valid, as the observed range in eccentricity for the extrasolar planets ranges from 0 to 0.9. As mentioned, we have assumed an infinitesimally thin disk throughout this project. Accounting for the disk's finite thickness is necessary for understanding the behavior of $d\epsilon/dt$ for $\epsilon \lesssim 0.1$. Second, as mentioned previously, the function $d\epsilon/dt$ may behave differently than we have calculated here for high eccentricities ($\epsilon \gtrsim 0.5$). Our calculation will therefore benefit from an improved understanding of disk properties when a massive planet is present in a highly eccentric orbit. Third, additional disk effects, such as turbulence, may reduce the degree of corotation resonance saturation proposed by Ogilvie and Lubow to a level consistent with eccentricity growth on a timescale of a few million years, allowing planetary orbits to survive Type II migration. Finally, these results can be utilized in numerical studies of planet migration, such as MA05, where the effects of the disk can be combined with other solar system phenomena, such as secular resonances between planets.

As this set of calculations illustrates, different disk properties, gap properties, and planet properties can lead to different types of behavior concerning the eccentricity evolution of giant planet orbits. In the vast ensemble of star and planet forming environments in our Galaxy (and others), we expect a wide variety of disk surface density profiles, gap widths, gap edge shapes, and other characteristics that determine eccentricity damping and excitation. In addition, for any given set of disk/planet properties, the eccentricity damping and/or excitation rates are complicated functions of eccentricity. As a result, although we have found a common denominator of eccentricity damping at $\epsilon = 0.3$ for a variety of gap shapes and widths, the question of how circumstellar disks affect the eccentricity evolution of their planets should generally be considered only in a statistical sense.

CHAPTER 6

SOLAR SYSTEM EVOLUTION IN THE PRESENCE OF MHD TURBULENCE

The combination of planet-planet scattering and simplified disk effects (constant damping rates of semi-major axis and eccentricity) has been shown to successfully reproduce the observed a-ϵ distribution of the extrasolar planets (Adams & Laughlin, 2003; Moorhead & Adams, 2005). The disk drives both planets inward while interactions between the planets compete with the disk's eccentricity damping; the result is both small a and a large range in ϵ. We found that many of our two-planet simulations spent a significant fraction of time in a low-order mean motion resonance.

As a next step, we want to explore the result of combining three phenomena potentially important to the process of solar system formation: planet-planet scattering, planetary migration, and disk turbulence. Laughlin, Steinacker, and Adams (2004) showed that disk turbulence induces a random walk in an embedded planet's semi-major axis that can potentially overwhelm Type I migration. Giant planets, on the other hand, clear an annulus in the circumstellar disk and therefore are less subject to turbulence; however, turbulence in the disk may be sufficient to prevent pairs of planets from maintaining a mean motion resonance. This modification of solar system dynamics may result in significantly different distributions of orbital parameters.

We present here simulations of a two-planet solar system under the influence of mutual gravitational interactions, Type II migration, and varying levels of MHD turbulence. We plan to extend this project to include large numbers of simulations with randomly chosen initial configurations to complete a parametric study similar to that performed in Moorhead & Adams (2005). These simulations are currently underway.

6.1 Methods and Initial Conditions

This section outlines our basic migration model which combines [1] the dynamical interactions of two planets, [2] inward forcing driven by tidal interactions with a background nebular disk (see also Kley 2000; Murray et al. 2002; Papaloizou 2003; Kley et al. 2004), and [3] MHD turbulence, which induces a random walk in orbital elements. Our goal here is to build on previous studies by producing a statistical generalization of the generic migration problem with two planets and an exterior disk – a situation that we expect is common during the planet formation process.

The numerical experiments are set up for two planets with the following orbital properties: Two planets are assumed to form within a circumstellar disk with initial orbits that are widely spaced. The central star is assumed to be of solar-type with mass $M_* = 1.0\ M_\odot$. For the sake of definiteness, the inner planet is always started with orbital period $P_{in} = 1900$ days, which corresponds to a semi-major axis $a_{in} \approx 3$ AU. This radial location lies just outside the snowline for most models of circumstellar disks and thus provides a fiducial starting point where the innermost giant planets are likely to form. For most of the simulations, the second (outer) planet is placed on an orbit with the larger period $P_{out} = \pi 2^{1/4} P_{in} \approx (3.736\ldots)P_{in}$; with this starting state, the planets are not initially in, or near, resonance but will have the opportunity to pass through a number of low-order mean motion resonances, including the 3:1 resonance, as the outer planet migrates inward. In the absence of disk turbulence, the two planets are often caught in mean motion resonances for some portion of their evolution (Moorhead and Adams, 2005; for a more detailed description, see Lee and Peale, 2002). The initial eccentricities of both planets are drawn from a uniform random distribution in the range $0 < \epsilon < 0.05$. The planets are also started with a small, but nonzero inclination angle in the range $i \leq 0.03$ (in radians). Planetary systems started in the exactly the same orbital plane tend to stay co-planar, whereas small departures such as these allow the planets to explore the full three dimensions of space.

The observed planetary mass function is nearly log-random, and the chosen planetary mass function tends to be preserved throughout solar system evolution (Moorhead and Adams, 2005); we choose $-1 \leq \log_{10}[M_P/M_J] \leq 1$, where M_J is the mass of Jupiter, as a good approximation of the observed exoplanet mass distribution.

The numerical integrations are carried out using a second-order mixed-variable symplectic (MVS) algorithm incorporating simple symplectic correctors (see Wisdom et al., 1996), *Mercury* (Chambers, 1991). This algorithm, while much more rapid than Bulirsch-Stoer, cannot handle close encounters (see the Appendix for a discussion of Bulirsch-Stoer and symplectic integration). While *Mercury*'s hybrid Bulirsch-Stoer/symplectic integrator can handle close encounters by switching to Bulirsch-Stoer when the planets move within a few Hill radii of each other, it is much less accurate, proving unstable when the planets move within 1 AU of the central star. As we found in Chapter 4 that collisions comprise a small percentage of the possible outcomes, we have therefore chosen to use the MVS integration scheme rather than the hybrid integrator. The equations of motion are those of the usual three body problem (two planets and the star) with the additional forcing terms to implement the effects of Type II migration and MHD turbulence in the disk on the planets. In each case, the simulations are carried out for 1 Myr.

The outer planet in the system is tidally influenced by a background circumstellar disk. Since the planets are (roughly) of Jovian mass, they clear gaps in the disk and the migration is Type II. Instead of modeling the interaction between the outer planet and disk in detail, we adopt a parametric treatment of semi-major axis and eccentricity damping:

$$\begin{aligned} a &= a_0\, e^{-t/\tau_a} && (6.1) \\ e &= e_0\, e^{-t/\tau_e}\,. && (6.2) \end{aligned}$$

We choose damping timescales $\tau_a = \tau_e = 0.3$ Myr. We assume here that the disk inside the orbit of the outer planet is sufficiently cleared out so that the inner planet does not usually experience a Type II torque. Over most of its evolution, the inner planet has a sufficiently small eccentricity so that it lies well inside the (assumed) gap edge and receives neglible torque from the disk (which lies outside the outer planet). When the inner planet attains a high eccentricity, however, it can approach a radius comparable to that of the outer planet and experience some torque. This (relatively minor) effect is included by giving the inner planet a torque that is reduced from that of the outer planet by a factor $(r_1/r_2)^6$.

In this set of simulations, we set the accretion and eccentricity damping time scales to be $\tau_a = \tau_e = 0.3$ Myr. This is roughly consistent with recent estimates and is roughly the correct order of magnitude to produce the observed distribution of semi-major axis and eccentricity in the absence of MHD turbulence (see Chapter 4). We would like to point out that our treatment of Type II migration relies on a host of studies of laminar disks; however, the study of overall migration trends in turbulent disks are inconclusive (Nelson, 2005) and so we adopt the simplest model of combining the two effects.

MHD turbulence is approximated using the prescription of LSA04; that is, we introduce a spectrum of nonlinear density perturbations which are capable of producing a random walk in the orbital elements of any embedded planets. The gravitational potential of such a perturbation is given by

$$\Phi = \frac{A\xi e^{-(r-r_c)^2/\sigma^2}}{r^{1/2}} \cos{(m\theta - \phi - \Omega_c\tilde{t})} \sin{(\pi \frac{\tilde{t}}{\Delta t})}\,. \tag{6.3}$$

The center of the perturbation has radial location r_c and initial angular location

ϕ, both of which are chosen from a random uniform distribution. The azimuthal wave number m, chosen from the log-random distribution $1 \leq m \leq 32$, determines the extent of the mode. The parameter $\sigma = \pi r_c/4m$ sets the shape of the mode as roughly 4:1. Notice that the mode travels with the Keplerian flow due to the appearance of the pattern speed Ω_c in the time dependent term. The duration of the perturbation is obtained from the sound crossing time of the mode along the angular direction; $\Delta t = 2\pi r_c/(m a_s)$, where a_s is the sound speed. When one perturbation ceases, we assume the immediate formation of another, so that the total number of nodes at any time is constant.

The overall amplitude of the modes, A, best approximates MHD turbulence with a value of approximately 2×10^{-2} AU$^{5/2}$ yr^{-2}, while the migration of terrestrial mass planets is observed to visibly change when $A > 2 \times 10^{-4}$ AU$^{5/2}$ yr^{-2} (LSA04.) We therefore investigate how Type II migration is affected at these same levels. The individual amplitude, ξ, is chosen from a gaussian random distribution with unit width.

6.2 Results

In the following section we present the solar systems that result from our simulations. The key difference between this experiment and previous studies (such as MA05) is the inclusion of turbulent fluctuations, which we investigate by gradually increasing the overall magnitude of the turbulence.

First we revisit the non-turbulent scenario, explored previously in Adams & Laughlin (2003) and Moorhead & Adams (2005). In this case, the outer planet quickly migrates inward under the influence of Type II migration. Along its route inward, the outer planet has the potential to become trapped in a mean motion resonance with the inner planet, and, in fact, this often occurs. We present one example in Figs. 6.1 and 6.2, where the inward migration of first the outer planet ($M_{out} = 0.12 M_J$), then both planets ($M_{in} = 0.33 M_J$) together, is plainly visible.

6.1

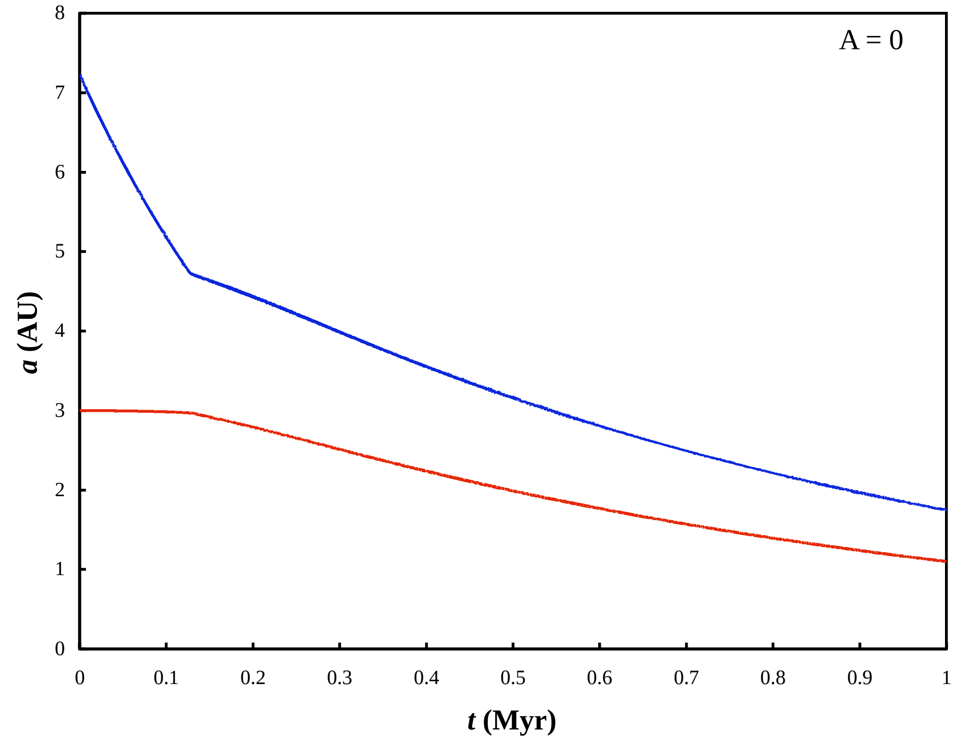

Figure 6.1. Planetary semi-major axes of a system of two interacting planets migrating under the influence of torques from a circumstellar disk in the absence of MHD turbulence. The outer planet starts outside 7 AU and is represented by the blue line. The inner planet starts at 3 AU and is represented by the red line.

6.2

Fig. 6.3 demonstrates that the two planets spend nearly the entire span of the simulation very close to a 2:1 period ratio, which is a strong indication that the two planets may be in resonance. However, this period ratio represents a necessary but not sufficient condition for the planets to be in resonance. In addition, the resonance angles must librate rather than circulate; these angles, for a 2:1 mean

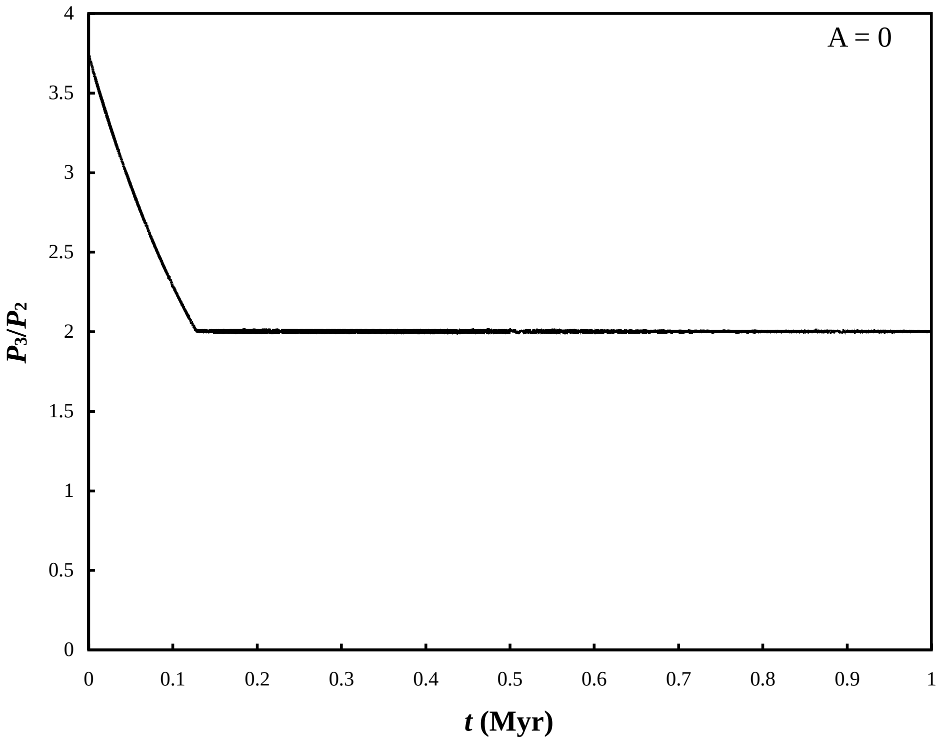

Figure 6.2. Ratio of the periods of two interacting planets migrating under the influence of torques from a circumstellar disk in the absence of MHD turbulence. The outer planet migrates inward quickly until the planets attain a period ratio of 2:1. The planets subsequently migrate inwards together, maintaining this period ratio.

motion resonance, are given by

$$\phi_1 = 2\lambda_2 - \lambda_1 - \varpi_1, \qquad \phi_2 = 2\lambda_2 - \lambda_1 - \varpi_2, \tag{6.4}$$

where the λ_j are the mean longitudes and the ϖ_j are the longitudes of pericenter (Murray and Dermott 2001). With this in mind, we present the 2:1 resonance angles in Fig. 6.3. Our representative case is indeed in a 2:1 mean motion resonance, as each angle librates about a constant value. These values are spaced approximately 100 degrees apart.

6.3

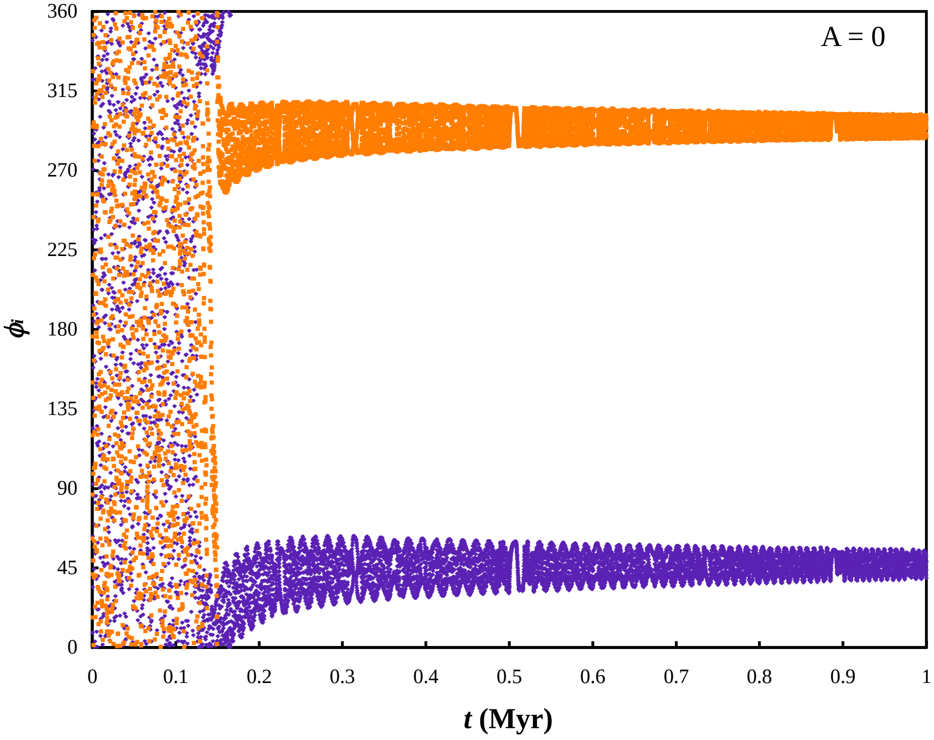

Figure 6.3. 2:1 resonance angles of two interacting planets migrating under the influence of torques from a circumstellar disk in the absence of MHD turbulence. $\phi_1 = 2\lambda_2 - \lambda_1 - \varpi_1$ and is represented by the purple diamonds. $\phi_2 = 2\lambda_2 - \lambda_1 - \varpi_2$ and is represented by the orange squares.

Our simulations always begin with small orbital eccentricities, in keeping with our current understanding of planet formation. However, once the planets enter a mean-motion resonance, planet-planet interactions tend to increase the orbital eccentricity of each (see Fig. 6.4). In our example, each planet's eccentricity smoothly increases, then saturates. It is worth noting that the less massive outer planet ($M_{out} = 0.12M_J$) attains a higher eccentricity than that of the more massive inner planet ($M_{in} = 0.33M_J$). In fact, the value of the eccentricity at eccentricity excitation saturation is inversely proportional to mass: $e_{out,sat}/e_{in,sat} = (M_{out}/M_{in})^{-1}$.

6.4

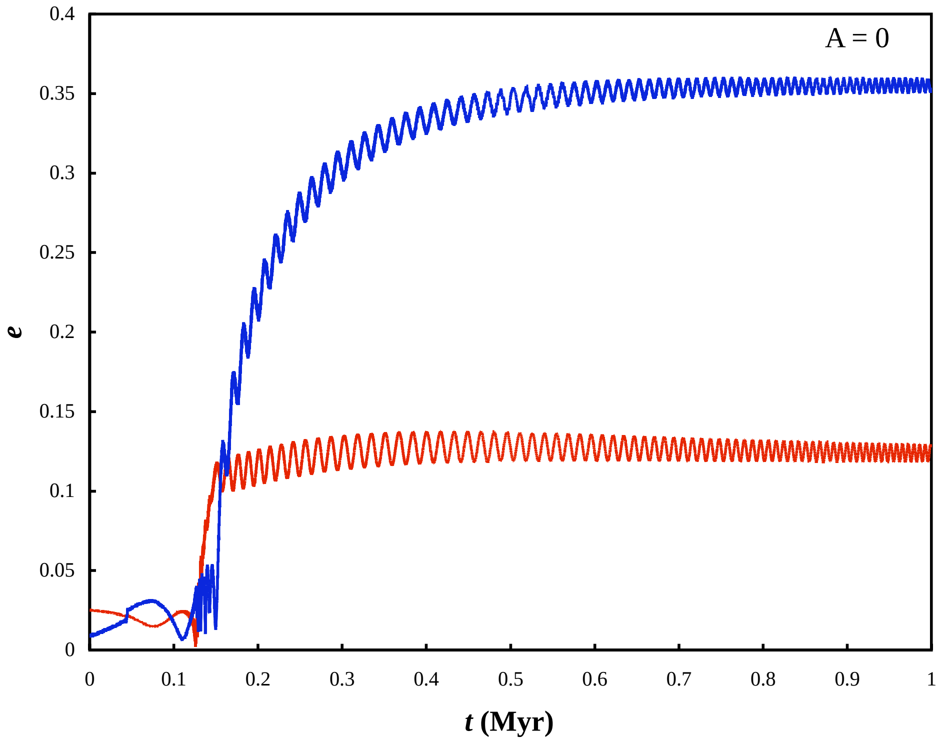

Figure 6.4. Planetary eccentricities of a system of two interacting planets migrating under the influence of torques from a circumstellar disk in the absence of MHD turbulence. The outer planet attains a higher value of eccentricity and is represented by the blue line. The inner planet is represented by the red line.

To summarize, in the absence of turbulence, our simulation of these two planets sees them quickly entering a 2:1 mean motion resonance and maintaining this resonance as the two planets migrate inward together. Neither the period ratio nor the resonance angles change appreciably over the course of the simulation.

Next we repeat the simulation, adding a small amount of MHD turbulence. Here we have employed the spectrum of LSA04, discussed above, with an overall amplitude of $2 \times 10^{-4}\mathrm{AU}^{5/2}\mathrm{yr}^{-2}$. This is equivalent to the value of 10^{-5} in the units of LSA04, or the value above which Type I migration changes its character.

Although Type I migration may change significantly above the threshold of $2 \times 10^{-4}\mathrm{AU}^{5/2}\mathrm{yr}^{-2}$, Type II migration does not. This is likely because [1] giant planets, being much more massive, are less susceptible to the tugging of turbulent fluctuations, and [2] these planets clear large gaps in the vicinity of their orbits, so turbulence must act from a distance. Thus, Type II migration proceeds (see Fig. 6.5) roughly as usual; the outer planet migrates quickly inward, the two planets enter a 3:1 mean motion resonance, and then both planets migrate inwards together. We see a small amount of noise in the outer planet's path due to the turbulence, but it is not enough to alter the system's evolution. The time evolution of eccentricity and the resonance angles are also unchanged.

6.5

While turbulence of the order of magnitude $2 \times 10^{-4}\mathrm{AU}^{5/2}\mathrm{yr}^{-2}$ is significant for Type I migration, MHD turbulence is expected to be two orders of magnitude larger (LSA04). We run our simulation once again, this time with $2 \times 10^{-2}\mathrm{AU}^{5/2}\mathrm{yr}^{-2}$; note that this level of turbulence best approximates the turbulence spectrum from LSA04's full MHD simulations. Much stronger turbulent fluctuations result, and the evolution of the system is drastically changed. A random walk component is visible in the planet's semi-major axis from the beginning of the simulation (Fig. 6.6). A random walk is also apparent in the planets' eccentricities (Fig. 6.7). We find that when the outer planet is scattered to large radii, the random walk temporarily ceases; this is because our treatment of the turbulent zone is restricted to between 0.05 and 15 AU.

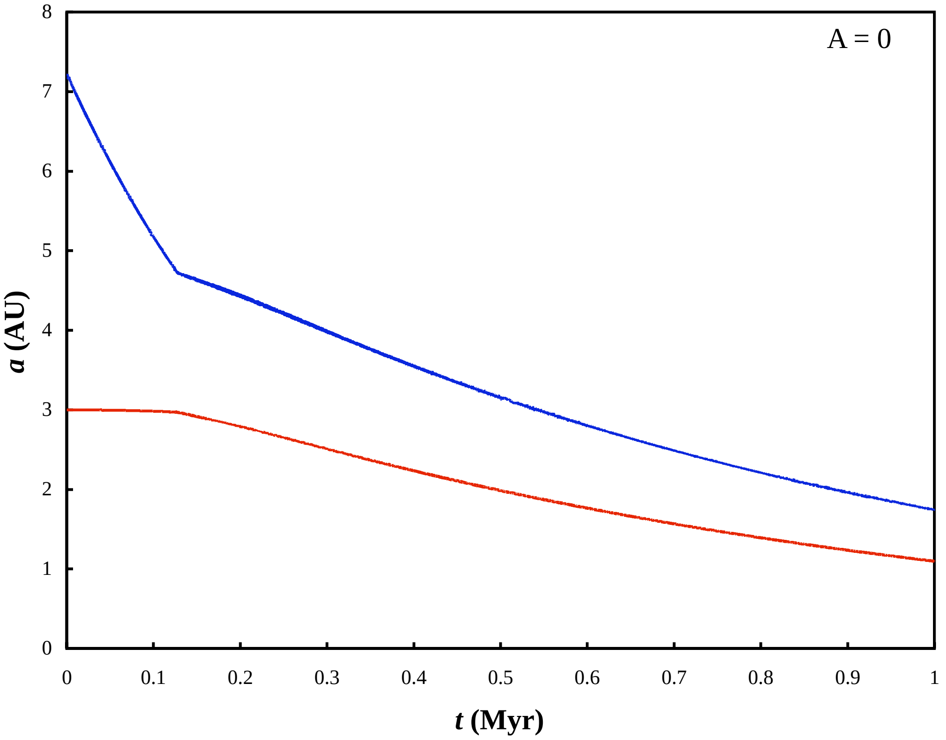

Figure 6.5. Planetary semi-major axes of a system of two interacting planets migrating under the influence of torques from a circumstellar disk in the presence of minimal MHD turbulence. Here the overall amplitude of the spectrum of turbulent fluctuations is given by $A = 2 \times 10^{-4}\text{AU}^{5/2}\text{yr}^{-2}$. The outer planet starts outside 7 AU and is represented by the blue line. The inner planet starts at 3 AU and is represented by the red line.

6.6

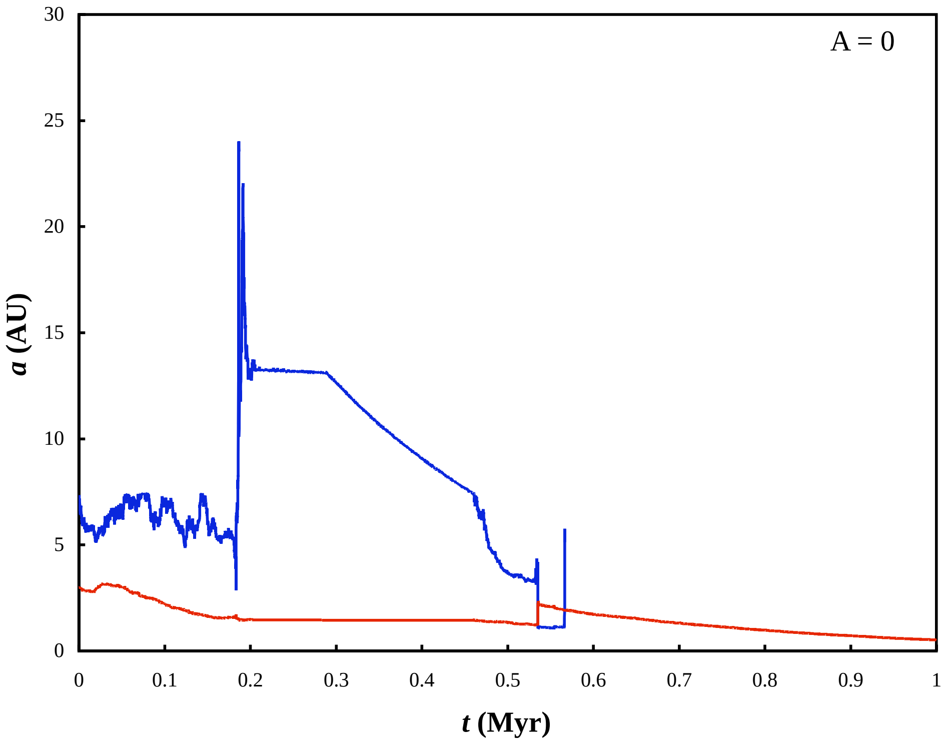

Figure 6.6. Planetary semi-major axes of a system of two interacting planets migrating under the influence of torques from a circumstellar disk in the presence of MHD turbulence. Here the overall amplitude of the spectrum of turbulent fluctuations is given by $A = 2 \times 10^{-2} \mathrm{AU}^{5/2} \mathrm{yr}^{-2}$. The outer planet starts outside 7 AU and is represented by the blue line. The inner planet starts at 3 AU and is represented by the red line.

6.7

The plot of semi-major axis versus time (Fig. 6.6) does not appear to show the planets anywhere near a mean motion resonance; Fig. 6.8 confirms it. The two planets, as a direct result of the inclusion of MHD turbulence, do not approach a mean motion resonance at any point, confirming one of our hypotheses. Additionally, turbulence leads to a different end state for the system, ejecting the outer planet after 0.57 Myr.

6.8

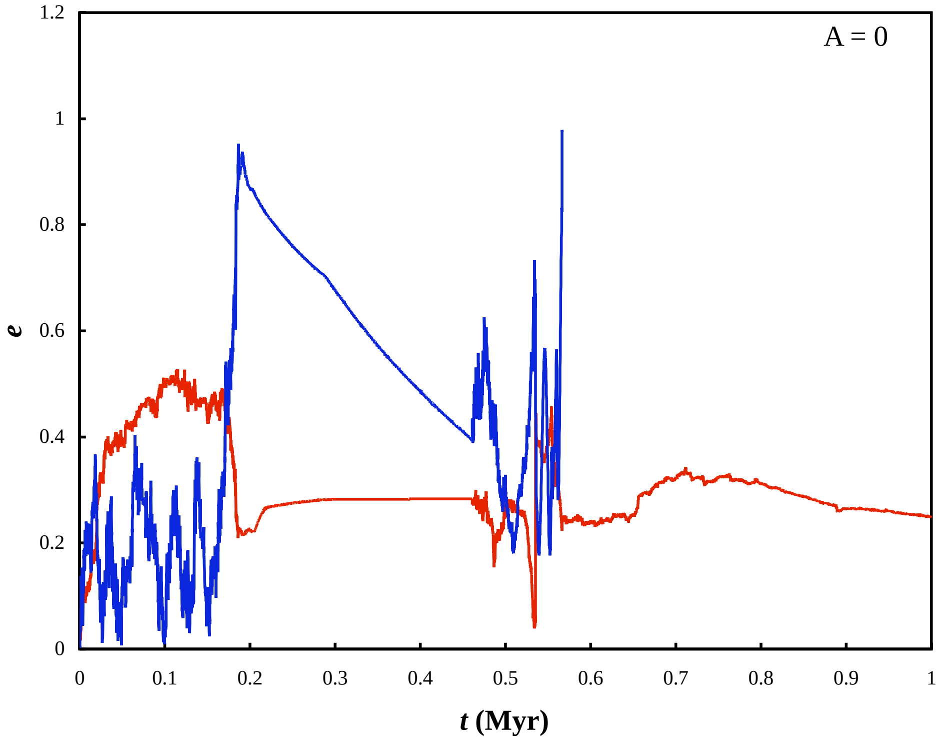

Figure 6.7. Planetary eccentricities of a system of two interacting planets migrating under the influence of torques from a circumstellar disk in the presence of MHD turbulence. Here the overall amplitude of the spectrum of turbulent fluctuations is given by $A = 2 \times 10^{-2}\mathrm{AU}^{5/2}\mathrm{yr}^{-2}$. The outer planet starts outside 7 AU and is represented by the blue line. The inner planet is represented by the red line.

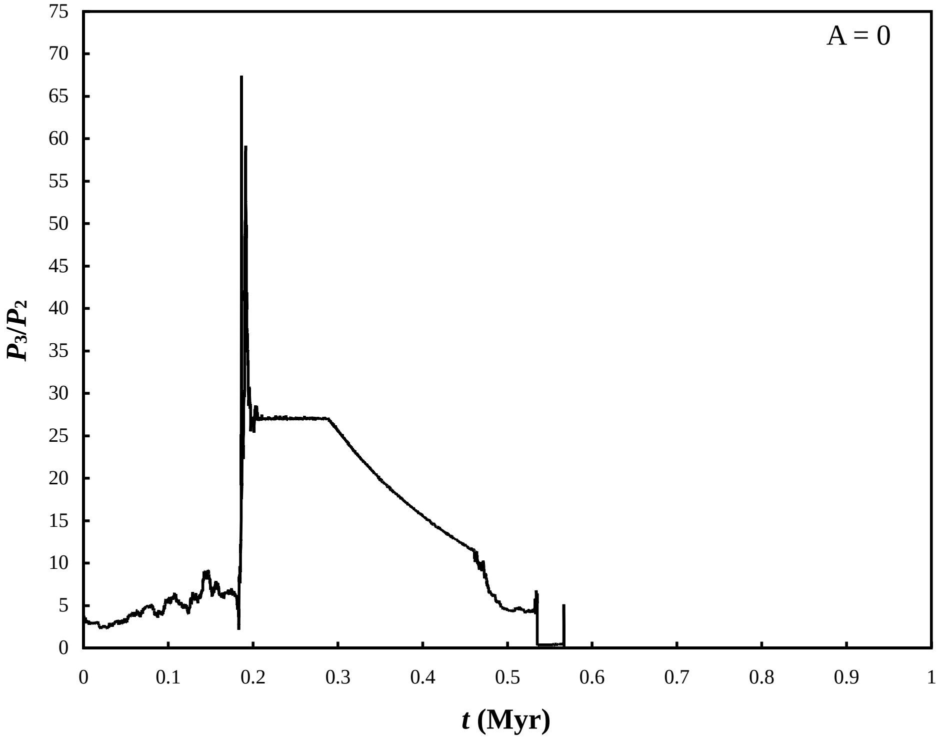

Figure 6.8. Ratio of the periods of two interacting planets migrating under the influence of torques from a circumstellar disk in the presence of MHD turbulence. The outer planet starts outside 7 AU and is represented by the blue line. The inner planet is represented by the red line. Note that the planets never enter a mean motion resonance.

In conclusion, we find that the introduction of turbulence at a level in agreement with MHD simulations changes the orbital evolution of giant planets. A random walk in orbital elements is observed, and the system is prevented from entering a mean motion resonance. Finally, the end state of the system is altered, with the ejection of one of the planets occurring halfway through the simulation.

6.3 Conclusions and Future Work

In this short section, we have explored the effects of disk turbulence on the planet migration scenario developed in this thesis. We have found that the introduction of turbulence into simulations of two planet solar systems undergoing Type II migration has the capacity to alter the evolution and outcome of these systems. We find that, in at least one case, the influence of turbulence prevents the planets from entering mean motion resonances, produces fluctuations in orbital elements such as eccentricity, and halves the lifetime of the outer planet.

These changes are likely to occur in every realization of planet-planet interactions, Type II migration, and MHD turbulence, although it should be noted that the system investigated here had planets of relatively low mass; planets have been observed to be much more massive than 0.1 M_J, and such planets would be less affected by turbulence. The next step to take is to complete a parametric study of three body systems under the influence of Type II migration and MHD turbulence similar to that of Moorhead & Adams (2005). Such a study would allow us to address the following questions: [1] What degree of turbulence is typically necessary to prevent capture into mean motion resonances? [2] How do varying levels of turbulence affect the number of surviving planets and the final distribution of orbital elements? [3] What combination of turbulence, Type II migration, and planet-planet scattering best recreates the observed a-e distribution?

MHD turbulence is a promising mechanism for rescuing planetary cores from runaway Type I migration. It is therefore important to evaluate whether turbulence is compatible with the observed distribution of giant planet orbital elements. If it is incompatible, then Type I migration must be halted by some other means, or MHD turbulence must fade before giant planets form.

CHAPTER 7

CONCLUSIONS

The rapid discovery of, to date, more than 200 extrasolar planets has revolutionized planetary astronomy. The attempt to explain these planets has produced a much improved core accretion model, and revived another planet formation model: the gravitational instability model. However, in their simplest form, both models fail to explain the orbital elements of the observed planets; the core accretion model works best at intermediate radii (for instance, Jupiter's current orbit) and requires solids for the initial phase of planet formation, which are rare within the condensation radius. The gravitational instability method works best where the disk is heavy and cold, and thus is prone to producing very massive planets (many Jupiter masses) tens to hundreds of AU from their host star. Since many of the observed planets have semi-major axes that are a small fraction of an AU in size, additional physics is required to explain their formation.

The migration mechanism developed by Goldreich and Tremaine (1980) provides a possible solution for this problem. If a circumstellar disk is present around a protoplanetary core, interactions between the disk and the planet act to drive the planet inward and damp its eccentricity. This process is so effective, in fact, that it is difficult to prevent the accretion of all cores onto the central star, but it is certainly capable of moving planets inward. If the planet has the opportunity to grow to gas giant size ($M_P > 0.1 M_J$) it begins to open a gap in the disk; this halts Type I migration and Type II migration, which proceeds on the viscous time scale of the disk, begins.

Thus, an understanding of Type II migration is necessary to describe the observed extrasolar planets, nearly all of which are of gap-opening mass.

Any viable migration scenario must be able to explain the observed distributions of orbital elements. We have shown in Chapter 4 that Type II migration (modeled using parametric disk torques) acting in combination with planet-planet scattering can produce these observed distributions (see Fig. 4.15). Furthermore, we find that our modeled systems have a variety of outcomes: accretion of one planet, ejection of one planet, or the persistence of both planets beyond the disk lifetime of a million years are all possible. Outcome was observed to be somewhat dependent on planet mass (see Fig. 4.3 and 4.4); the smaller of the two planets is generally the planet to be ejected or accreted onto the central star, and persistence of both planets throughout the simulation tends to occur when both planets were less than $1 M_J$. Each outcome occurs in approximately equal numbers, with the number of double planet solar systems in the set of complete simulations ranging from 30 to 50% of the total. This is a higher rate of two planet systems than is observed; we might then favorably consider any additional physics that reduces the number of two planet systems. We also note that these systems tend to spend a significant portion of their lifetime in mean motion resonance; planet in both 2:1 and 3:1 mean motion resonances have been observed, with systems in the 2:1 mean motion resonance proving to be slightly more stable.

We have shown in Chapter 6 that the introduction of turbulence into simulations of two planet solar systems undergoing Type II migration has the potential to alter the outcome of these systems. Turbulence can prevent planets from entering mean motion resonances and can lead to a different outcome, such as the ejection of one planet (see Fig. 6.6). We note that a higher level of turbulence is required to appreciably alter Type II migration; while an overall amplitude of the turbulence spectrum of 2×10^{-4} may be sufficient to change the character of Type I migration (LSA04), the same level of turbulence does not alter the orbital evolution of giant planets (see Fig. 6.5). However, the level of turbulence encountered in MHD simulations is sufficient to alter the evolution of these massive planets (see Fig. 6.6). We anticipate that turbulence may affect the orbital parameters of planetary systems in general and increase the number of planets scattered out of their solar systems; to quantify this effect, a parametric study of the combination of planet-planet interactions, Type II migration, and MHD turbulence in the manner of Moorhead & Adams (2005) is necessary.

Our simulations treat semi-major axis and eccentricity damping due to disk torques in a highly simplified manner; we explicitly damp both orbital elements on given time scales, usually a fraction of a million years. While this treatment of semi-major axis is in good agreement with simulations of Type II migration, the time evolution of eccentricity is highly debated. This debate is outlined in Chapter 5, and a more complete calculation of the time derivative of eccentricity for non-negligible starting eccentricity is performed. We encounter neither uniform damping nor uniform excitation of orbital eccentricity, but rather a function $d\epsilon/dt$ that varies in both sign and magnitude depending on eccentricity and other solar system properties. Most significantly, we find that for every combination of disk and planet properties investigated, corotation torques produce negative values of $d\epsilon/dt$ for some range in ϵ within the interval [0.1, 0.5] (Fig. 5.13). If corotation torques are saturated, this region of eccentricity damping disappears, and excitation occurs on a short timescale of less than 0.08 Myr. Thus, our study does not produce eccentricity excitation on a timescale of a few Myr – we obtain either eccentricity excitation on a short time scale, or eccentricity damping on a longer time scale. As eccentricity excitation on a time scale of 0.08 Myr would result in the ejection of nearly every forming planet from its host system, we conclude that, for now, it is more reasonable to assume eccentricity damping in parametric studies.

This thesis work has led to a number of subsequent projects. As mentioned, we are in the midst of producing data for a parametric study of planet-planet interactions, Type II migration, and MHD turbulence similar to that of Moorhead & Adams (2005). In an effort to better understand the behavior of eccentricity, we are looking into using the hydrodynamics code FARGO (Masset, 2000) to simulate disk-planet interactions for a variety of starting orbital elements; comparison of these results with the results of Chapter 5 will enhance our understanding of corotation resonance saturation.

APPENDIX A

NUMERICAL INTEGRATION OF N-BODY SYSTEMS

Much of this thesis is devoted to understanding the evolution of solar systems over very long timescales; i.e., millions of years. In order to achieve this, we must use integration schemes that have high accuracy and speed. We have implemented two such algorithms in our research thus far; the Bulirsch-Stoer integration scheme and a symplectic integrator, *Mercury*.

A.1 Bulirsch-Stoer Integration

Suppose an N-body is governed by the equation $d\mathbf{x}/dt = f(t, \mathbf{x})$. We can divide a given timestep, H, into N equal, smaller timesteps, $H = Nh$, and apply a *modified midpoint* method (Bodenheimer, Laughlin, & Rozyczka, 2007, hereafter BLR07):

$$\begin{aligned} \mathbf{x}_0 &= \mathbf{x}(t) && \text{(A.1)} \\ \mathbf{x}_1 &= \mathbf{x}_0 + hf(t, \mathbf{x}_0) && \text{(A.2)} \\ \mathbf{x}_n &= \mathbf{x}_{n-2} + 2hf(t + [n-2]h, \mathbf{x}_{n-1}) \text{ for } n = 2, ..., N && \text{(A.3)} \\ \mathbf{x}(t + H) &= \frac{1}{2}[\mathbf{x}_N + \mathbf{x}_{N-1} + hf(t + H, \mathbf{x}_N)] && \text{(A.4)} \end{aligned}$$

We can repeat this process for the same overall time step with increasing values of N; each successive calculation's error can be expressed as a power series in h^2; thus, the $\mathbf{x}(t + H)$'s can be combined to produce a final result that has high accuracy in comparison to computation time. Richardson extrapolation describes the process in which this polynomial combination is calculated for $N = 2, ..., 2k$ and the resulting polynomial is extrapolated for $k \rightarrow \infty$. Once these coefficients are determined, the resulting expression is evaluated at $h = 0$ to determine $\mathbf{x}(t + H)$.

Bulirsch-Stoer integration (Stoer & Bulirsch, 1980), which uses Richardson extrapolation, is well suited to calculating dynamics for systems in which energy and angular momentum are conserved; often, the level to which these invariants must be conserved is predetermined, and Bulirsch-Stoer integration is performed with an initial timestep that preserves this level of accuracy, usually chosen to be something like 10^{-11} for solar system simulations.

In addition to being speedy and accurate, the Bulirsch-Stoer method has the additional benefit of being able to handle close encounters, making it superior to several other methods (including symplectic integration) in this respect. As a result, Bulirsch-Stoer is often the method of choice for N-body integrations where $N < 10$ and close encounters may occur. For these reasons, we chose to perform Bulirsch-Stoer integration in our initial studies of 3-body systems under the influence of Type II migration (Moorhead & Adams, 2005).

A.2 Symplectic Integration

While the motion resulting from the gravitational interaction of two bodies can be written down in an analytic form (and is usually the focus of at least a chapter in any mechanics course), the 3-body problem is non-integrable (Murray & Dermott, 2001). However, if there is a large imbalance in mass, such as one encounters with a star and two planets, the gravitational effect of the third, small body can be treated as a perturbation to the gravitational forces exerted by the most massive body in the system. Symplectic integration takes advantage of this by dividing the motion of the planet into Keplerian and non-Keplerian components.

To be more specific, symplectic integration divides the Hamiltonian into Keplerian and non-Keplerian components. This can be done most easily using Jacobian coordinates (Wisdom & Holman, 1991), in which the origin is located at the center of mass of the system. Integration is then carried out in two steps. First, the motion due to the Keplerian portion of the Hamiltonian can be carried out rapidly using Gauss' f and g functions (BLR07):

$$\begin{aligned} \mathbf{r}(t) &= f(t,t_0)\mathbf{r}(t_0) + g(t,t_0)\mathbf{v}(t_0) && \text{(A.5)} \\ \mathbf{v}(t) &= \dot{f}(t,t_0)\mathbf{r}(t_0) + \dot{g}(t,t_0)\mathbf{v}(t_0) && \text{(A.6)} \end{aligned}$$

where

$$\begin{aligned} f(t,t_0) &= \frac{a}{r_0}[\cos(E-E_0)-1]+1 && \text{(A.7)} \\ g(t,t_0) &= (t-t_0)+\frac{1}{n}[\sin(E-E_0)-(E-E_0)] && \text{(A.8)} \end{aligned}$$

where r_0 is the radial location at time t_0 and E is the eccentric anomaly at time t.

Next, second-order corrections resulting from contributions to the non-Keplerian portion of the Hamiltonian are applied in the form of velocity "kicks." Additional forces, such as disk torques, can very naturally be added at this stage as well:

$$\Delta\mathbf{v}_i' = \Delta t\left(\frac{d\mathbf{v}_i'}{dt}\right)_{\text{interaction}} = \Delta t\,\frac{1}{m_i'}\left(\frac{\partial H_{\text{interaction}}}{\partial \mathbf{r}_i'}\right). \quad \text{(A.9)}$$

Symplectic integration is extremely rapid – up to ten times more rapid than Bulirsch-Stoer (BLR07) – and is well-suited to studying the long-term behavior of multiple planet systems where the planets do not experience close encounters. However, as mentioned, symplectic integration relies on the assumption that the system is near Keplerian; that is, that the gravitational effects of additional bodies can be treated as perturbations to the star's gravitational potential. When two planets have a close encounter, the assumption obviously breaks down. In general, symplectic integration is no longer a viable approach when two bodies approach within 3 Hill radii of each other, where the Hill radius of a body with semi-major axis a_i and mass M_i is given by

$$R_H = a_i\left(\frac{M_i}{M_{tot}}\right)^{1/3}. \quad \text{(A.10)}$$

Our simulations of N-body systems in the presence of Type II migration and MHD disk turbulence proved, at first, to be much slower than our simulations without turbulence. Therefore, for our more recent work (see Chapter 6), we are using a symplectic integrator: to be specific, the *Mercury* symplectic integrator developed by John Chambers (1999).

BIBLIOGRAPHY

[1] Adams, F. C., & Laughlin, G. 2003. Migration and dynamical relaxation in crowded systems of giant planets. Icarus 163, 290.

[2] Balbus, S.A., Hawley, J.F. 1991. A powerful local shear instability in weakly magnetized disks. I - Linear analysis. II - Nonlinear evolution. Astrophys. J. 376, 214 – 222.

[3] Balmforth, N.J., Korycansky, D.G. 2001. Non-linear dynamics of the corotation torque. Mon. Not. R. Astron. Soc. 326, 833 – 851.

[4] Bate, M. R., Lubow, S. H., Ogilvie, G. I., Miller, K. A. 2003. Three-dimensional calculations of high- and low-mass planets embedded in protoplanetary discs. Mon. Not. R. Astron. Soc. 341, 213 – 229.

[5] Beaugé, C., Ferraz-Mello, S., Michtchenko, T. A. 2003. Extrasolar Planets in Mean-Motion Resonance: Apses Alignment and Asymmetric Stationary Solutions. Astrophys. J. 593, 1124 – 1133.

[6] Bernstein, R., Shectman, S. A., Gunnels, S. M., Mochnacki, S., Athey, A. E. 2003. MIKE: A Double Echelle Spectrograph for the Magellan Telescopes at Las Campanas Observatory. SPIE 4841, 1694 – 1704.

[7] Binney, J., Tremaine, S. 1987. Galactic Dynamics. (Princeton University Press).

[8] Bodenheimer, P., Laughlin, G.P., Rozyczka, M. 2007. Numerical Methods in Astrophysics: An Introduction. (Boca Raton: Taylor & Francis).

[9] Boss, A.P. 2001. Gas Giant Protoplanet Formation: Disk Instability Models with Thermodynamics and Radiative Transfer. Astrophys. J. 563, 367 – 373.

[10] Bryden, J., Rózyczka, M., Lin, D.N.C., Bodenheimer, P. 2000. Astrophys. J. 540, 1091 – 1101.

[11] Chambers, J.E. 1999. A Hybrid Symplectic Integrator that Permits Close Encounters between Massive Bodies. Mon. Not. R. Astron. Soc. 304, 793 – 799.

[12] Charbonneau, D, Brown, T.M., Latham, D.W., Mayor, M 2000. Detection of Planetary Transits Across a Sun-like Star. Astrophys. J. 529, L45 – L48.

[13] D'Angelo, G., Lubow, S.H., Bate, M.R. 2006. Evolution of Giant Planets in Eccentric Disks. Astrophys. J. 652, 1698 – 1714.

[14] D'Antona, F., Mazzitelli, I. 1994. New pre-main-sequence tracks for M less than or equal to 2.5 solar mass as tests of opacities and convection model. Astrophys. J. 90, 467 – 500.

[15] Ferraz-Mello, S., Beaugé, C., Michtchenko, T. A. 2003. Evolution of Migrating Planet Pairs in Resonance. Celest. Mech. Dynam. Astron. 87, 99 – 112.

[16] Fischer, D. A., Marcy, G. W., Butler, R. P., Vogt, S. S., Frink, S., Apps, K. 2001. Planetary Companions to HD 12661, HD 92788, and HD 38529 and Variations in Keplerian Residuals of Extrasolar Planets. Astrophys. J. 551, 1107 – 1118.

[17] Ford, E. B., Havlickova, M., Rasio, F. A. 2001. Dynamical instabilities in extrasolar planetary systems containing two planets. Icarus 150, 303 – 313.

[18] Ford, E.B., Quinn, S.N., Veras, D. 2008. Characterizing the Orbital Eccentricities of Transiting Extrasolar Planets with Photometric Observations. Astrophys. J., accepted.

[19] Goldreich, P., Sari, R. 2003. Eccentricity evolution for planets in gaseous disks. Astrophys. J. 585, 1024 – 1037.

[20] Goldreich, P., Soter, S. 1963. Q in the solar system. Icarus 5, 375 – 389.

[21] Goldreich, P., Tremaine, S. 1980. Disk-satellite interactions. Astrophys. J. 241, 425 – 441.

[22] Haisch, K. E., Lada, E. A., Lada, C. J. 2001. Disk frequencies and lifetimes in young clusters. Astrophys. J. 553, L153 – 156.

[23] Hatzes, A. P., and 12 colleagues, Evidence for a long period planet orbiting Epsilon Eridani. Astrophys. J. 529, L145 – 148.

[24] Henry, Gregory W., Marcy, Geoffrey W., Butler, R. Paul, Vogt, Steven S. 2000. A Transiting "51 Peg-like" Planet. Astrophys. J. 529, L41 – 44.

[25] Holman, M. J.; Murray, N. W. 2005. "The Use of Transit Timing to Detect Terrestrial-Mass Extrasolar Planets." *Science*, **307**, 1288-1291.

[26] Hut, P. 1981. Tidal evolution in close binary systems. Astron. Astrophys. 99, 126 – 140.

[27] Ikoma, M., Nakazawa, K., Emori, H. 2000. Formation of Giant Planets: Dependences on Core Accretion Rate and Grain Opacity. Astrophys. J. 537, 1013 – 1025.

[28] Katz, J. I. 1997. Single close encounters do not make eccentric planetary orbits. Astrophys. J. 484, 862 – 865.

[29] Klahr, H.; Bodenheimer, P. 2006. Formation of Giant Planets by Concurrent Accretion of Solids and Gas inside an Anticyclonic Vortex. Astrophys. J. 639, 432 – 440.

[30] Kley, W. 1999. Mass flow and accretion through gaps in accretion discs. Mon. Not. R. Astron. Soc. 303, 696 – 710.

[31] Kley, W. 2000. On the migration of a system of protoplanets. Mon. Not. R. Astron. Soc. 313, L47 – L51.

[32] Kley, W., D'Angelo, G., Henning, T. 2001. Three-dimensional simulations of a planet embedded in a protoplanetary disk. Astrophys. J. 547, 457 – 464.

[33] Kley, W., Peitz, J., Bryden, G. 2004. Evolution of planetary systems in resonance. Astron. Astrophys. 414, 735 – 747.

[34] Kornet, K., Bodenheimer, P., Rózyczka, M. 2002. Models of the formation of the planets in the 47 UMa system. Astron. Astrophys. 396, 977 – 986.

[35] Lada, C. J., Lada, E. A. 2004. Embedded clusters in molecular clouds. Ann. Rev. Astron. Astrophys. 41, 57 – 115.

[36] Laughlin, G., Chambers, J. E., Fischer, D. 2002. A dynamical analysis of the 47 Ursae Majoris planetary system. Astrophys. J. 579, 455 – 467.

[37] Laughlin, G., Steinacker, A., Adams, F. 2004. Type I Planetary Migration with MHD Turbulence. Astrophys. J. 608, 489 – 496.

[38] Lee, M. H. 2004. Diversity and origin of 2:1 orbital resonances in extrasolar planetary systems. Astrophys. J. 611, 517 – 527.

[39] Lee, M. H., and Peale, S. J. 2002. Dynamics and origin of the 2:1 orbital resonances of the GJ 876 planets. Astrophys. J. 567, 596 – 609.

[40] Lin, D.N.C., Bodenheimer, P., Richardson, D. C. 1996. Orbital migration of the planetary companion of 51 Pegasi to its present location. Nature 380, 606 – 607.

[41] Lin, D.N.C., Ida, S. 1997. On the origin of massive eccentric planets. Astrophys. J. 477, 781 – 791.

[42] Lin, D. N. C., Papaloizou, J. C. B. 1993. On the tidal interaction between protostellar disks and companions. In: Levy, E.H., Lunine, J.I. (Eds.). Protostars and Planets, vol. III. Univ. Arizona Press, Tucson, pp. 749 – 836.

[43] Lin, D.N.C., Papaloizou, J.C.B., Terquem, C., Bryden, G., Ida, S. 2000. Orbital evolution and planet-star interaction. in Protostars and Planets IV, eds. V. Mannings, A. P. Boss, and S. S. Russell. (Tucson: Univ. Arizona Press), pp. 1111 – 1134.

[44] Lissauer, J.J. 1993. Planet formation. Ann. Rev. Astron. Astrophys. 31, 129 – 174.

[45] Lubow, S. H., Ogilvie, G. I. 2001. Secular interactions between inclined planets and a gaseous disk. Astrophys. J. 560, 997 – 1009.

[46] Marcy, G. W., Butler, R. P. 1996. A planetary companion to 70 Virginis. Astrophys. J. 464, L147 – 150.

[47] Marcy, G. W., Butler, R. P. 1998. Detection of extrasolar giant planets. Ann. Rev. Astron. Astrophys. 36, 57 – 97.

[48] Marcy, G. W., Butler, R. P. 2000. Planets orbiting other suns. Publ. Astron. Soc. Pacific 112, 137 – 140.

[49] Marcy, G. W., Butler, R. P. 2000. Planets orbiting other suns. Publ. Astron. Soc. Pacific 112, 137 – 140.

[50] Marzari, F., Weidenschilling, S. J. 2002. Eccentric extrasolar planets: The jumping Jupiter model. Icarus 156, 570 – 579.

[51] Masset, F. 2000. FARGO: A fast eulerian transport algorithm for differentially rotating disks. Astron. Astrophys. Supp. 141, 165 – 173.

[52] Masset, F. S., Papaloizou, J.C.B. 2003. Runaway migration and the formation of hot Jupiters. Astrophys. J. 588, 494 – 508.

[53] Masset, F. S., Snellgrove, M. 2001. Reversing type II migration: resonance trapping of a lighter giant protoplanet. Mon. Not. R. Astron. Soc. 320, L55 –59.

[54] Mayor, M., Queloz, D. 1995. A Jupiter-mass companion to a solar-type star. Nature 378, 355 – 359.

[55] Menou, K., Goodman, J. 2004. Low-mass planet migration in T Tauri α-disks. Astrophys. J. 606, 520 – 531.

[56] Moorhead, A.V., Adams, F.C. 2005. Giant planet migration through the action of disk torques and planet-planet scattering. Icarus 178, 517 – 539.

[57] Moorhead, A.V., Adams, F.C. 2008. Eccentricity evolution of giant planet orbits due to circumstellar disk torques. Icarus 193, 475 – 484.

[58] Murray, C. D., Dermott, S. F. 2001. Solar System Dynamics. (Cambridge: Cambridge Univ. Press).

[59] Murray, N., Hansen, B., Holman, M., Tremaine, S. 1998. Migrating Planets. Science 279, 69 – 71.

[60] Murray, N., Paskowitz, M., Holman, M. 2002. Eccentricity evolution of migrating planets. Astrophys. J. 565, 608 – 620.

[61] Naef, D., and 11 colleagues 2001. HD80606b, A planet on an extremely elongated orbit. Astron. Astrophys. 375, L27 – 30.

[62] Nelson, R. P. 2005. On the orbital evolution of low mass protoplanets in turbulent, magnetised disks. Astron. Astrophys. 443, 1067 – 1085.

[63] Nelson, R. P., Papaloizou, J.C.B., Masset, F., Kley, W. 2000. The migration and growth of protoplanets in protostellar discs. Mon. Not. R. Astron. Soc. 318, 18 – 36.

[64] Ogilvie, G. I., Lubow, S. H. 2003. Saturation of the corotation resonance in a gaseous disk. Astrophys. J. 587, 398 – 406.

[65] Papaloizou, J.C.B. 2003. Disc-Planet Interactions: Migration and resonances in extrasolar planetary systems. Celest. Mech. Dynam. Astron. 87, 53 – 83.

[66] Papaloizou, J.C.B., Nelson, R. P., Masset, E. 2001. Orbital eccentricity growth through disc-companion tidal interaction. Mon. Not. R. Astron. Soc. 366, 263 – 275.

[67] Papaloizou, J.C.B., Terquem, C. 2001. Dynamical relaxation and massive extrasolar planets. Mon. Not. R. Astron. Soc. 325, 221 – 230.

[68] Perryman, M.A.C. 2000. Extra-solar planets. Inst. Phys. Rep. Progress Phys. 63, 1209 – 1272.

[69] Porras, A., Christopher, M., Allen, L., Di Francesco, J., Megeath, S. D., Myers, P. C. 2003. A catalog of young stellar groups and clusters within 1 kpc of the Sun. Astron. J. 126, 1916 – 1924.

[70] Press, W. B., Flannery, B. P., Teukolsky, S. A., Vettering, W. T., 1986. Numerical Recipes: The art of scientific computing. (Cambridge: Cambridge Univ. Press).

[71] Press, W. B., Teukolsky, S. A. 1977. On the formation of close binaries by two-body tidal capture. Astrophys. J. 213, 183 – 192.

[72] Rasio, F. A., Ford, E. B. 1996. Dynamical instabilities and the formation of extrasolar planetary systems. Science 274, 954 – 956.

[73] Saumon, D.; Guillot, T. 2004. Shock Compression of Deuterium and the Interiors of Jupiter and Saturn. Astrophys. J. 609, 1170 – 1180.

[74] Schäfer, C., Speith, R., Hipp, M., Kley, W. 2004. Simulations of planet-disc interactions using Smoothed Particle Hydrodynamics. Astron. Astrophys. 418, 325 – 335.

[75] Shu, F. H. 1992. Gas Dynamics. (Mill Valley: Univ. Science Books).

[76] Snellgrove, M. D., Papaloizou, J.C.B., Nelson, R. P. 2001. On disc driven inward migration of resonantly coupled planets with application to the system around GJ876. Astron. Astrophys. 374, 1092 – 1099.

[77] Stoer, J., Bulirsch, R. 1980. Introduction to Numerical Analysis. (New York: Springer-Verlag).

[78] Struve, O. 1952. Proposal for a project of high-precision stellar radial velocity work. The Observatory 72, 199 – 200.

[79] Tabachnik, S., & Tremaine, S. 2002. Maximum-likelihood method for estimating the mass and period distributions of extrasolar planets. Mon. Not. R. Astron. Soc. 335, 151 – 158.

[80] Thommes, E. W., Lissauer, J. J. 2003. Resonant inclination excitation of migrating giant planets. Astrophys. J. 597, 566 – 580.

[81] Toomre, Q. 1964. On the gravitational stability of a disk of stars. Astrophys. J. 139, 1217 – 1238.

[82] Trilling, D. E., Benz, W., Guillot, T., Lunine, J. I., Hubbard, W. B., Burrows, A. 1998. Orbital evolution and migration of giant planets: Modeling extrasolar planets. Astrophys. J. 500, 902 – 914.

[83] Ward, W. R. 1997. Protoplanet migration by nebula tides. Icarus 126, 261 – 281.

[84] Ward, W. R., Hahn, J. M. 2000. Disk-Planet Interactions and the Formation of Planetary Systems. in Protostars and Planets IV, eds. V. Mannings, A. P. Boss, and S. S. Russell. (Tucson: Univ. Arizona Press), pp. 1135 – 1155.

[85] Weidenschilling, S. J., Marzari, F. 1996. Gravitational scattering as a possible origin for giant planets at small stellar distances. Nature 384, 619 – 620.

[86] Weinberg, S. 1972. Gravitation and cosmology. (New York: Wiley).

[87] Wisdom, J., Holman, M. 1991. Symplectic maps for the n-body problem. Astron. J. 102, 1528 – 1538.

[88] Wisdom, J., Holman, M., Touma, J. 1996. Symplectic Correctors. Fields Institute Communications 10, 217.

[89] Wu, Y., Goldreich, P. 2002. Tidal evolution of the planetary system HD 83443. Astrophys. J. 564, 1024 – 1027.

[90] Zapatero Osorio, M. R., Bjar, V.J.S., Martn, E. L., Rebolo, R., Barrado y Navascus, D., Bailer-Jones, C.A.L., Mundt, R. 2000. Discovery of young isolated planetary mass objects in the Sigma Orionis star cluster. Science 290, 103 – 107.